JOURNAL OF APPLIED PHYSICS

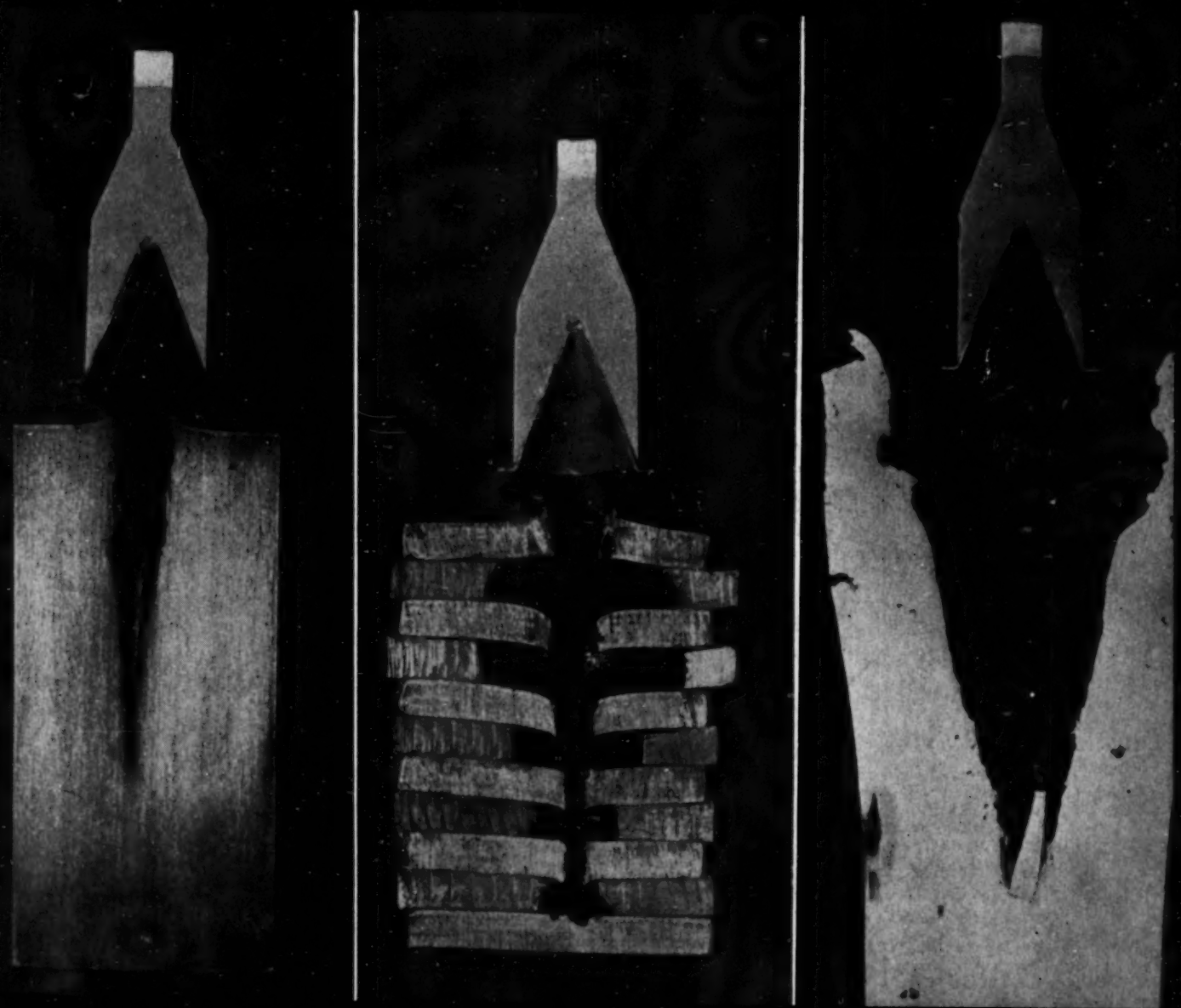

JOURNAL OF APPLIED PHYSICS

Vol. 19, No. 6 JUNE, 1948

In This Issue

Page

Qualitative Experimental Verification of the Change of Burning Rate of Rocket Powders with Radiation Path Length S. S. PENNER 511

Universal Curves for Dielectric-Filled Wave Guides and Microwave Dielectric Measurement Methods for Liquids W. H. SURBER, JR. 514

Erratum: On the One-Dimensional Theory of Steady Compressible Fluid Flow in Ducts with Friction and Heat Addition BRUCE L. HICKS, DONALD J. MONTGOMERY, AND ROBERT H. WASSERMAN 523

Method of Determining the Angle of Arrival A. W. STRAITON, W. E. GORDON, AND A. H. LAGRONE 524

Choice of Operating Mode for Standing Wave Type Linear Accelerators for Electrons ELLIOTT J. LAWTON 534

Theory of Plastic Flow *versus* Theory of Plastic Deformation W. PRAGER 540

Theory of Extreme Values and Its Implications in the Study of the Dielectric Strength of Paper Capacitors BENJAMIN EPSTEIN AND HAMILTON BROOKS 544

Magnetization in Perpendicularly Superposed Direct and Alternating Fields F. J. BECK AND J. M. KELLY 551

Explosives with Lined Cavities GARRETT BIRKHOFF, DUNCAN P. MAC DOUGALL, EMERSON M. PUGH, AND SIR GEOFFREY TAYLOR 563

Spectral Emissivity and Electron Emission Constants of Thoria Cathodes T. E. HANLEY 583

Letters to the Editor:

Analogy between Isopachic Stress Lines and Equipotential Lines ROBERT EMMETT MUELLER 590

Note on the Phase Difference between Two Waves Reflected from the Ionosphere J. M. KELSO 590

In Every Issue

Calendar of Meetings 543

New Booklets 591

Here and There 592

Index to Advertisers xxxviii

BOARD OF EDITORS

ELMER HUTCHISSON, *Editor*

Associate Editors

R. BOWLING BARNES
OTTO BEECK
W. F. BUSSE
W. JAMES LYONS
PHILIP MORRISON
PAUL E. SABINE
FREDERICK SEITZ
J. R. TOWNSEND
JOHN VON NEUMANN

Publication of the American Institute of Physics

ADMINISTRATIVE STAFF

HENRY A. BARTON, *Director*

CLEVELAND NORCROSS, *Assistant Director*

RUTH F. BRYANS, *Publication Manager*

THEODORE VORBURGER, *Business Manager*

JOHN T. TATE, *Adviser on Publications*

GOVERNING BOARD

GEORGE R. HARRISON, *Chairman*

WALLACE WATERFALL, *Secretary*

GEORGE B. PEGRAM, *Treasurer*

LUIS W. ALVAREZ
ROBERT B. BRODE
E. U. CONDON
A. J. DEMPSTER
W. F. FAIR, JR.
HARVEY FLETCHER
R. C. GIBBS
W. V. HOUSTON
PAUL E. KLOPSTEG
F. W. LOOMIS
PHILIP M. MORSE
A. H. PFUND
JOHN T. TATE
M. W. WHITE
A. G. WORTHING

The JOURNAL OF APPLIED PHYSICS, published monthly at Prince and Lemon Sts., Lancaster, Pa., is devoted to physics in its role as the science basic to other natural sciences and to the arts and industries. Previous to 1937 this publication was known as PHYSICS. The JOURNAL OF APPLIED PHYSICS publishes editorials, news of physicists, and reviews, as well as technical papers of applied physics.

Manuscripts should be submitted to Elmer Hutchisson, Editor, Case Institute of Technology, Cleveland 6, Ohio.

Subscriptions and orders for back numbers should be addressed to Prince and Lemon Streets, Lancaster, Pa. or to the American Institute of Physics, 57 East 55 Street, New York 22, N. Y.

Subscription Price

	U.S. AND CANADA	ELSEWHERE
To members and associate members of the American Institute of Physics	$6.00	$7.00
To all others	8.00	9.00

Back Number Prices

Complete set: Vol. 1, July, 1931–Vol. 18, 1947—$132.00
Yearly back number rate: $10.00
Single copies: $1.00 each.

Changes of address should be sent to the Business Manager, American Institute of Physics; **corrected proofs** should be sent to the Publication Manager, American Institute of Physics.

Advertising rates supplied on request. Orders, advertising copy, and cuts should be sent to the American Institute of Physics.

Entered as second class matter January 22, 1937, at the Post Office at Lancaster, Pennsylvania, under the Act of March 3, 1879. Accepted for mailing at the special rate of postage provided for in the Act of February 28, 1925, authorized May 2, 1932.

Copyright 1948, by the American Institute of Physics.

Journal
of
Applied Physics

Volume 19, Number 6 June, 1948

Qualitative Experimental Verification of the Change of Burning Rate of Rocket Powders with Radiation Path Length*

S. S. Penner**
Allegany Ballistics Laboratory, Cumberland, Maryland
(Received November 21, 1947)

Experimental studies on step-machined powder grains indicate a small increase in the average burning rate of solid fuel rocket propellants with an increase in the radiation path length. This result is in agreement with theoretical predictions.

INTRODUCTION

THE rate of burning of solid fuel rocket propellants can be determined from the nature of the variation of the chamber pressure with time during the burning of the charge. The geometric configuration of the powder grain must be known.[1] It is found experimentally that the pressure developed during the burning of the powders is nearly constant for a constant value of K, where K is defined as the ratio of the surface area of the burning powder to the cross-sectional area at the nozzle throat. The dependence of pressure on K suggests the use of a step-machined powder grain for a study of the effect of radiation path length on the rate of burning.

A representative step-machined powder charge is shown in the following Fig. 1. As the charge burns, the powder surface recedes with a nearly uniform rate in a direction normal to itself. If the width of the steps, d, is much greater than the half-web thicknesses $\frac{1}{2}W_1$, $\frac{1}{2}W_2$, etc., then the powder surface area decreases in steps as the half-web thicknesses $\frac{1}{2}W_1$, $\frac{1}{2}W_2$, etc. are consumed in succession. A stepwise decrease in powder surface during burning is accompanied by a stepwise decrease in K and, therefore, also by a corresponding change in chamber pressure. The chamber pressure as a function of time is shown in Fig. 2 for a step-machined, perforated, cylindrical powder grain.

In Fig. 2 t_0 corresponds to the time when the entire powder surface is first ignited; t_{b_1} is the time at which the half-web thickness $\frac{1}{2}W_1$ has been consumed; t_{b_2} is the corresponding

* This is the last of three articles abstracted from OSRD report No. 5251 which was written in 1945 at the Allegany Ballistics Laboratory. The work was carried out under OSRD Contract OEMsr-273 with the George Washington University, Washington, D. C. The original paper was reissued as Part IV of OSRD report No. 5817.

A summary of the original paper is given in the Bibliography of Scientific and Industrial Reports, Office of Technical Service, Department of Commerce, Vol. 3, No. 4, Oct. 1946. The PB number is 34764.

The radiation program at the Allegany Ballistics Laboratory was initiated by the Director of Research, Dr. R. E. Gibson. Dr. W. H. Avery, to whom the author is indebted for advice throughout the course of the work, directed the radiation studies.

The author wishes to acknowledge the aid of the Editorial Staff of the Jet Propulsion Laboratory, California Institute of Technology, in preparing this paper for publication.

** Present address: Jet Propulsion Laboratory, California Institute of Technology, Pasadena, California.

[1] W. H. Avery, R. E. Hunt, and M. N. Donin, OSRD report No. 5827, Jan. 1946; W. H. Avery, R. E. Hunt, and L. D. Sachs, OSRD report No. 5824, March 1946.

time when the half-web thickness $\frac{1}{2}W_2$ has burnt completely, etc.

The step-machined powder grains are contained in a cylindrical motor chamber of inside diameter D_c during burning. The radiation path length normal to the half-web thickness $\frac{1}{2}W_j$ is

$$L_j=(D_c-W_j-w)/2, \tag{1}$$

where w represents the inside diameter of the perforation. The firing of step-machined powder grains therefore offers the opportunity of studying the dependence of the burning rate on pressure under conditions where the radiation path length is varied in steps.

THEORY

The average rate of burning of the j'th web (W_j) is defined according to the relation

$$\bar{r}_j=\tfrac{1}{2}W_j/t_{bj}. \tag{2}$$

The corresponding average pressure is

$$\bar{p}_j=(1/t_{bj})\int_0^{t_{bj}} p\,dt. \tag{3}$$

The average burning rate over the j'th *step of the pressure-time curve* is designated as $\bar{r}_j'$ and the corresponding average pressure is $\bar{p}_j'$. Equations (4) and (5) may be used to define these quantities:

$$\bar{r}_j'=(\tfrac{1}{2}W_j-\tfrac{1}{2}W_{j-1})/(t_{bj}-t_{bj-1}) \tag{4}$$

and

$$\bar{p}_j'=[1/(t_{bj}-t_{bj-1})]\int_{t_{bj-1}}^{t_{bj}} p\,dt. \tag{5}$$

The definitions of $\bar{r}_j'$ and $\bar{p}_j'$ according to Eqs. (4) and (5) involve the assumption that the rate of burning is independent of the radiation path length. The assumption that the burning rate is the same for all of the steps of the charge is contrary to the radiation theory since the average outside radiation path length for $\frac{1}{2}W_{j-1}$ is greater than for $\frac{1}{2}W_j$. Therefore, the burning rate, $\bar{r}_j'$, while corresponding to the correct time interval, is calculated for a web $(\frac{1}{2}W_j-\frac{1}{2}W_{j-1})$ which is actually too small. It follows that the calculated values of $\bar{r}_j'$ are too small.*** A qualitative verification of the radiation hypothesis may thus be obtained if it can be demonstrated experimentally that $\bar{r}_j'$ is less than $\bar{r}_j$ at the same average pressure.

Since the difference between $\bar{r}_j$ and $\bar{r}_j'$ is very small,[2] it is preferable to base the experimental check of the theory on a comparison of entire groups of data rather than on a comparison of individual points. For this reason plots of $\bar{r}_j$ *vs.* $\bar{p}_j$ should be presented on the same graph with the observed values for $\bar{r}_j'$ and $\bar{p}_j'$.

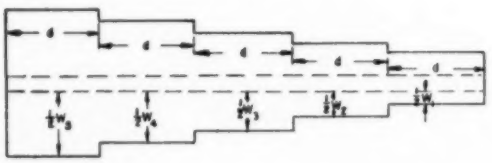

FIG. 1. Step-machined, perforated, cylindrical powder grain. The powder surface recedes in a direction normal to itself during burning.

EXPERIMENTAL RESULTS AND DISCUSSION

Details for the experimental procedure used to determine the pressure in a rocket chamber as a function of the time are given elsewhere.[1] For the present study it proved to be necessary to use carefully machined powder grains with smooth surfaces in order to decrease the experimental errors normally encountered in this type of work. However, in spite of the precautions which were exercised, the random scatter of experimental points was found to exceed the magnitude of the effect under investigation in some cases. Nevertheless, the results are sufficiently reproducible to afford at least qualitative verification for the radiation theory.

The experimental results obtained for two

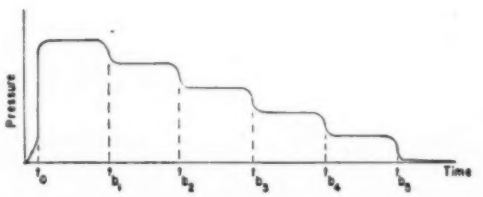

FIG. 2. Chamber pressure as a function of time for a step-machined, perforated, cylindrical powder grain.

*** This argument does not hold for $\frac{1}{2}W_1$. Thus $\bar{r}_1$ and $\bar{r}_1'$ are identical.

[2] See preceding paper: S. S. Penner, J. App. Phys. **19**, 392 (1948).

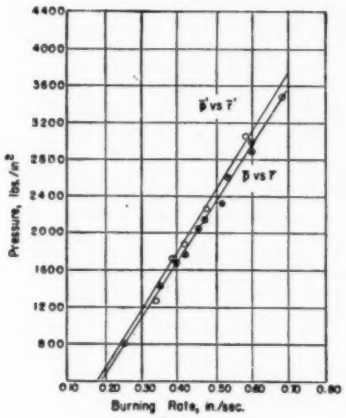

FIG. 3. Burning rate as a function of pressure for an undarkened rocket powder at 25°C.

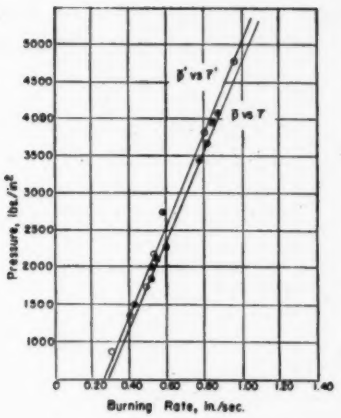

FIG. 4. Burning rate as a function of pressure for a darkened rocket powder at 25°C.

representative double base rocket powders**** are shown in Figs. 3 and 4. The data shown in these figures were calculated from the experimental pressure *vs.* time curves obtained in two or more independent tests on powder grains containing from two to five steps.

**** The composition of the powders was similar to the JPT formulation (see reference 2). The darkened powder contained 0.02 percent of finely divided carbon.

Reference to Figs. 3 and 4 shows that the values of $\bar{r}$ are generally greater than the values of $\bar{r}'$ at the same pressure. The predictions of the radiation theory for the effect of radiation path length on the rate of burning of solid fuel propellants are thus borne out qualitatively. In view of the limited experimental accuracy no further conclusions appear to be justified.

Universal Curves for Dielectric-Filled Wave Guides and Microwave Dielectric Measurement Methods for Liquids*†

W. H. SURBER, JR.
Department of Electrical Engineering, Princeton University, Princeton, New Jersey
(Received December 11, 1947)

The characteristics of wave guides containing a non-ideal dielectric medium are expressed in terms of a dissipation factor, D, the effect of which is analogous to that of the loss tangent of the medium, $\tan\delta$, for coaxial or two-conductor transmission lines. A set of universal curves may then be constructed for the variation of the wave-guide parameters as functions of the dielectric loss factor in terms of D. These curves are independent of the dielectric constant, ϵ', and of the frequency and mode of operation.

An experimental method is described for the measurement of the dielectric constants of medium and high loss liquids using a variable length of liquid dielectric column contained in a section of wave guide or coaxial line and terminated by a perfectly reflecting plane. Either a unidirectional coupler or slotted line may be used to observe the variation of the magnitude of the reflection coefficient with the dielectric sample length. An exact analytical expression is given for the determination of the constants of the medium using the dielectric constant, ϵ', and the dissipation factor, D, as the primary independent parameters instead of ϵ' and $\tan\delta$. A graphical method of solution is also given.

I. INTRODUCTION

IN the microwave frequency region, measurements to determine the dielectric properties of matter are normally made upon a sample of the material which is completely enclosed within a section of coaxial transmission line, hollow wave guide, or some form of resonant cavity. The behavior of the system must be analyzed and the dielectric constants calculated in terms of the propagation characteristics of the electromagnetic energy through the dielectric medium.

The same general principles were originally applied in 1895 at lower frequencies by Drude, who used an open two-wire line immersed in the medium.[1] A general solution of the transmission line problem for a section of dielectric-filled line terminated by a reflecting plane has been given by S. Roberts and A. von Hippel,[2] and a modification of their method for the case of low loss dielectrics was developed by T. W. Dakin and C. N. Works.[3]

The complex dielectric constant of the medium may be defined as

$$\epsilon=\epsilon_0(\epsilon'-j\epsilon''), \tag{1}$$

where ϵ_0 is the dielectric constant of free space in m.K.S. units. The electrical characteristics for the *TEM* mode along a section of two-conductor transmission line may then be separated into two groups. One of these groups is affected primarily by the relative dielectric constant, ϵ', with only a small correction term due to the loss factor, ϵ'', while the second set of characteristics is determined by the dielectric loss and may be expressed solely in terms of the loss tangent of the medium, $\tan\delta=\epsilon''/\epsilon'$.

* This paper is based upon work done for an Office of Naval Research project and is a condensation of portions of technical reports I and II, ONR Contract N6ori-105, Task Order IV: *I. Methods of Measurement of Dielectric Constant and Loss Factor for Liquids at Microwave Frequencies* (March, 1947); *II. Universal Curves for Wave Guides containing a Lossy Dielectric Medium and Applications to Dielectric Measurements* (August, 1947).

† This method was used by a group of workers under Professor C. P. Smyth of the Chemistry Department, Princeton University, to investigate the dielectric constants of certain groups of pure organic liquids in the 1.25-cm and 3.0-cm regions. Their experimental results, together with an interpretation of their data in terms of the molecular structure of the compounds, appear in the following reports: H. L. Laquer, *The Complex Dielectric Constant of Some Liquid Organic Halides at Three Centimeter Wavelength*, Dissertation presented to the Faculty of Princeton University, October 1947; W. M. Heston, Jr., E. J. Hennelly, and C. P. Smyth, *The Measurement of the Dielectric Constant and Absorption in Liquids at 1.27 cm. Wavelength*, Report for ONR Contract N6ori-105, Task Order IV. This material is to be published in part in the Journal of the American Chemical Society.

[1] Paul Drude, Ann. d. Physik und Chemie **55**, 663 (1895); *ibid.* **61**, 466 (1897); Zeits. f. physik. Chemie **23**, 267 (1897).

[2] S. Roberts and A. von Hippel, J. App. Phys. **17**, 610 (1946).

[3] T. W. Dakin and C. N. Works, J. App. Phys. **18**, 789 (1947).

For the *TE* or *TM* modes in a hollow wave guide, the effect of the dielectric medium is modified because of the existence of a finite cut-off frequency for the system. The electrical properties which are caused by the dielectric power loss may still be expressed, however, as functions of a single dielectric factor by the use of a new parameter, D, which may be called the "dissipation factor" of the system, defined as

$$D=\epsilon''/[\epsilon'-(\lambda/\lambda_c)^2]=\tan\delta/[1-(1/\epsilon')(\lambda/\lambda_c)^2], \tag{2}$$

where λ is the wave-length in free space of the excitation frequency and λ_c is the free space wave-length for the cut-off frequency of the air-filled guide. This dissipation factor, D, depends on the geometrical shape of the wave-guide cross section and the mode of operation only to the extent that they determine the cut-off wave-length, λ_c. For coaxial transmission lines λ_c is infinite and D reduces to the $\tan\delta$ of the medium.

The use of ϵ' and D as the two independent dielectric parameters, instead of ϵ' and $\tan\delta$ or ϵ'', results in a considerable logical simplification of the analysis of the wave-guide circuit operation. By using D as the dielectric loss parameter, a set of universal curves may be constructed for the variation with dielectric loss of the electrical characteristics of the system. These curves are independent of the relative dielectric constant, ϵ', and of the frequency and mode of operation. The range of validity and percent error for approximations in the wave-guide equations for low loss materials may also be discussed with more generality in terms of D than of the $\tan\delta$ of the medium.

For low loss media for which $D<0.1$ (or $\tan\delta<0.1$, as is more usually stated), the effects of ϵ' and D on the propagation constants are approximately independent, and the dielectric constants of the medium may then be expressed in a relatively direct manner in terms of the experimentally observed quantities. For higher loss media this is considerably more difficult algebraically because of the interaction of both ϵ' and D in determining the electrical behavior of the system. The measurement of the characteristics of these medium and high loss materials is important for the investigation of the molecular structure of matter, although these materials are not normally used in electrical circuits.

II. UNIVERSAL CURVES

For a hollow wave guide of uniform cross section having high conductivity metallic walls and containing a non-ideal dielectric medium, the equation for the electrical characteristics may be developed entirely in terms of ϵ', D, and λ_c. The general analysis of the propagation of electromagnetic energy along a system of conducting surfaces is well known and is developed in several recent texts.[4,5] Most of the equations for the wave-guide characteristics given below are found scattered throughout the literature in an equivalent form,[5-7] although they frequently appear in an approximate form valid only for low loss media.

The propagation constant for the air-filled guide, γ_g, may be expressed as

$$\gamma_g=\alpha_c+j(2\pi/\lambda_g), \tag{3}$$

$$\lambda_g=\lambda/(1-(\lambda/\lambda_c)^2)^{\frac{1}{2}}, \tag{4}$$

where λ_g is the wave-length in the guide, λ the wave-length in free space, and α_c the attenuation due to conductor loss in the walls of the wave guide. The propagation constant for the dielectric-filled guide, γ_d, is then

$$\gamma_d=(\alpha_c'+\alpha_d)+j(2\pi/\lambda_d), \tag{5}$$

$$\lambda_d=[\lambda/(\epsilon'-(\lambda/\lambda_c)^2)^{\frac{1}{2}}][1-\tan^2(\tfrac{1}{2}\tan^{-1}D)]^{\frac{1}{2}}, \tag{6}$$

$$\alpha_d=\pi\epsilon''(\lambda_d/\lambda^2)=\pi D[\lambda_d/(\lambda_d)_0^2], \tag{7}$$

$$\begin{aligned}\alpha_d\lambda_d&=2\pi D/[1+(1+D^2)^{\frac{1}{2}}]\\&=2\pi\tan(\tfrac{1}{2}\tan^{-1}D),\end{aligned} \tag{8}$$

where λ_d is the wave-length in the dielectric-filled guide, $(\lambda_d)_0$ is the guide wave-length for a lossless dielectric medium having the same ϵ', α_d the attenuation caused by dielectric power loss in nepers per meter, and α_c' the attenuation caused by wall loss in the presence of the di-

[4] J. A. Stratton, *Electromagnetic Theory* (McGraw-Hill Book Company, Inc., New York, 1941).

[5] Ramo and Whinnery, *Fields and Waves in Modern Radio* (John Wiley and Sons, Inc., 1944).

[6] Sperry Gyroscope Company, *Microwave Transmission Design Data* (1944).

[7] W. B. Westphal, Report IX, Laboratory for Insulation Research, Massachusetts Institute of Technology, Contract OEMsr-191, N.D.R.C. (1945).

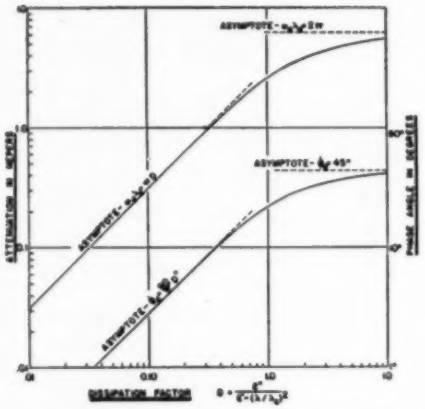

FIG. 1. Variation of the dielectric attenuation per wave-length, $\alpha_d\lambda_d$, and the phase angle of the characteristic impedance, ϕ_d, with the dissipation factor, D.

electric. The relative permeability of the dielectric medium is assumed to be unity and the magnetic loss factor zero. These equations apply for either the *TE* or *TM* modes.

For the *TE* modes of operation, which are the type normally used in measurement circuits, the characteristic per unit impedance of the dielectric-filled guide relative to the empty guide is given by the equation:

$$Z_d = |Z_d| e^{j\phi_d} = R_d + jX_d = \gamma_0/\gamma_d, \tag{9}$$

$$|Z_d| = \left(\frac{1-(\lambda/\lambda_c)^2}{\epsilon'-(\lambda/\lambda_c)^2}\right)^{\frac{1}{2}} \cdot \frac{1}{(1+D^2)^{\frac{1}{4}}}, \tag{10}$$

$$\phi_d = \tfrac{1}{2}\tan^{-1}D. \tag{11}$$

A useful alternative form for $|Z_d|$ in terms of λ_d is

$$|Z_d| = (\lambda_d/\lambda_0)\cos(\tfrac{1}{2}\tan^{-1}D). \tag{12}$$

Many possible variations of these formulae may be obtained by the manipulation of algebraic and trigonometric identities. The trigonometric forms are frequently the most useful for exact computational purposes. For low and medium loss media, the first two terms of a simple series expansion are usually quite adequate. A number of equivalent forms for these equations are tabulated in the ONR report II cited, and a generalized form for magnetic as well as dielectric media is also given there.

From these equations it is evident that the dielectric attenuation per wave-length, $(\alpha_d\lambda_d)$ in nepers, and the phase angle of the characteristic impedance, ϕ_d, are functions solely of the dissipation factor, D, and are independent otherwise of ϵ', λ, λ_c, or the mode of operation. Universal curves of these functions are shown in Fig. 1.

The per unit variation of λ_d, $|Z_d|$, R_d, and X_d as functions of the dielectric loss are plotted similarly as universal curves in terms of D in Fig. 2. The wave-length in the dielectric and the characteristic impedance are referred to their values for an ideal dielectric medium having the same ϵ' but zero loss factor, i.e.,

$$(\lambda_d)_0 = \lambda/(\epsilon'-(\lambda/\lambda_c)^2)^{\frac{1}{2}}, \tag{13}$$

$$(Z_d)_0 = \left(\frac{1-(\lambda/\lambda_c)^2}{\epsilon'-(\lambda/\lambda_c)^2}\right)^{\frac{1}{2}}. \tag{14}$$

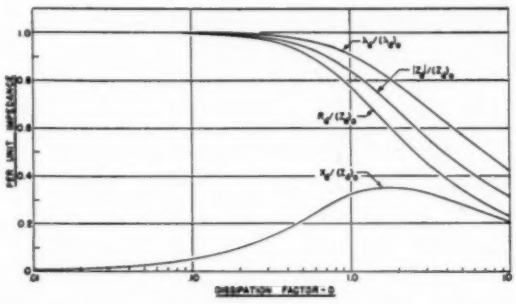

FIG. 2. Per unit variation of the wave-length in the guide, λ_d, and of the characteristic impedance, $|Z_d|$, R_d, and X_d, with the dissipation factor, D.

The experimentally observed quantities can usually be interpreted more or less directly in terms of the wave-length in the dielectric, λ_d, and the attenuation per wave-length, $\alpha_d\lambda_d$. The wall loss attenuation, α_c', is negligible relative to α_d for medium and high loss materials, but must be corrected for in the case of very low loss media. The dielectric constants of the medium may then be computed from the equations

$$D = \tan[2\tan^{-1}(\alpha_d\lambda_d/2\pi)], \tag{15}$$

$$\epsilon' = (\lambda/\lambda_c)^2 + (\lambda/\lambda_d)^2\cdot[1-\tan^2(\tfrac{1}{2}\tan^{-1}D)], \tag{16}$$

$$\epsilon'' = (1/\pi)(\lambda/\lambda_d)^2\cdot(\alpha_d\lambda_d). \tag{17}$$

III. MICROWAVE DIELECTRIC MEASUREMENT METHODS FOR MEDIUM AND HIGH LOSS LIQUIDS

A. Measurement Techniques

The dielectric constant and loss tangent of a liquid medium in the microwave region may be

determined by measuring the propagation constant through a sample of the liquid contained in a section of wave guide or coaxial line. This may be done either by moving a probe directly through the liquid medium or by varying the length of the dielectric column, using a movable reflecting plunger as a termination, and observing the variation in the reflection coefficient at the face of the sample with either a unidirectional coupler or a slotted line placed ahead of the liquid cell. The latter method was chosen because of the greater simplicity required for the experimental equipment.

For medium and high loss media the mathematical difficulty in the computation of the dielectric constants is considerably greater than in the low loss case since approximations to separate the effects of ϵ' and D are no longer valid. The relative loss in the wave-guide components is much smaller, however, thus reducing one possible source of error due to any uncertainty in the measurement of the apparatus losses.

The wave-length in the dielectric-filled guide, λ_d, can be determined for low loss media by using an external slotted line to observe the phase of

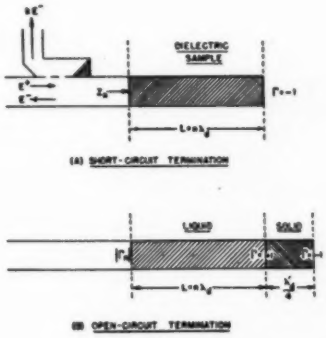

FIG. 3. Schematic wave-guide circuit.

the reflection coefficient at the face of the sample. This can no longer be done conveniently for higher loss materials, however, since the characteristic phase angle, ϕ_d, may be appreciable and the rate of phase variation at the face of the sample quite low for a large $(\alpha_d\lambda_d)$. Instead, λ_d may be measured by observing the variation in the magnitude of the reflection coefficient as the length of the dielectric column is varied. This is most easily done with a unidirectional coupler. The attenuation, $\alpha_d\lambda_d$, and thus the dielectric loss factor may then be obtained from the ratios of the amplitudes of the reflection coefficient at the successive $\lambda_d/2$ or odd $\lambda_d/4$ dielectric lengths, depending on the type of terminating plunger.

For a dielectric sample of length L, enclosed within a section of wave guide and terminated by a perfectly reflecting short-circuit plane, as shown in Fig. 3, the magnitude of the reflection coefficient, Γ, at the face of the dielectric will be given by the equation,

$$|\Gamma| = \left|\frac{E^-}{E^+}\right| = \left|\frac{Z_d \tanh\gamma_d L - 1}{Z_d \tanh\gamma_d L + 1}\right|, \qquad (18)$$

where E^+ is the incident voltage wave and E^- the reflected voltage wave in the empty guide. For an ideal open-circuit termination, the function "$\tanh\gamma_d L$" in Eq. (18) is replaced by "$\coth\gamma_d L$."

The output of a square law detector coupled to the reflected wave by a unidirectional coupler is proportional to $|\Gamma|^2$ for a constant incident power. For lengths of the dielectric sample which are integral multiples of $\lambda_d/2$ for the short-circuit termination, or which are odd integral multiples of $\lambda_d/4$ for an open-circuit termination, the set of values of $|\Gamma|^2$ may be written in the form:

$$|\Gamma|^2 = \frac{T + 2Fe^{-2n\alpha_d\lambda_d} + e^{-4n\alpha_d\lambda_d}}{1 + 2Fe^{-2n\alpha_d\lambda_d} + Te^{-4n\alpha_d\lambda_d}}, \qquad (19)$$

where

$$T = |\Gamma_\infty|^2 = |(Z_d - 1)/(Z_d + 1)|^2,$$

$$F = (1 - |Z_d|^2)/(|1 + Z_d|^2).$$

$L = n \cdot \lambda_d$ = length of the sample, so that:

$n = 1/2, 1, 3/2, \cdots$ for short-circuit termination;
$n = 1/4, 3/4, 5/4, \cdots$ for open-circuit termination.

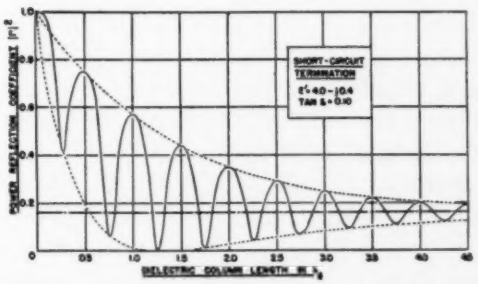

FIG. 4. Variation of reflected power with dielectric column length for a short-circuit termination, $\tan\delta = 0.10$ for the medium.

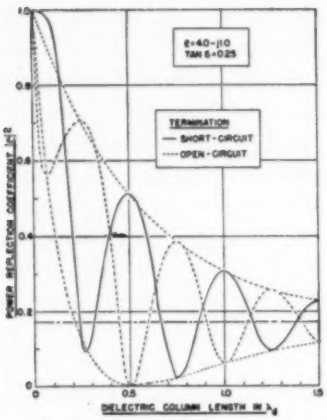

FIG. 5. Variation of reflected power with dielectric column length for a perfectly reflecting termination and a medium having a $\tan\delta = 0.25$.

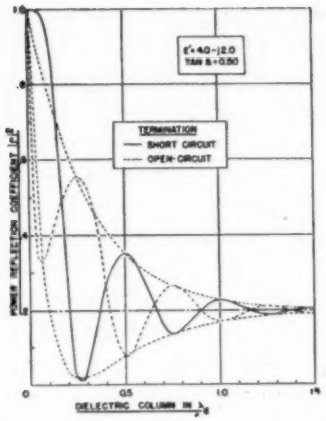

FIG. 6. Variation of reflected power with dielectric column length for a perfectly reflecting termination and a medium having a $\tan\delta = 0.50$.

To simplify the notation, the square of the magnitude of the reflection coefficient for an infinite length dielectric column, $|\Gamma_\infty|^2$, is denoted by T, and the length of the sample, L, is measured in terms of fractions of a wave-length in the dielectric, n. Equation (19) is applicable only for two discrete sets of physically realizable points which occur at the maxima of the reflection coefficient.

The reflected signal is proportional to $|\Gamma|^2$, and its variation with the length of the dielectric column is shown in Figs. 4, 5, and 6 for both the short-circuit and open-circuit plungers and for several values of loss tangent for the medium. The locus of the values of $|\Gamma_n|^2$ for lengths which are multiples of $\lambda_d/4$ and $\lambda_d/2$, from Eq. (19) is indicated as a dotted curve although it actually represents only a set of discrete points. This curve does not represent an upper envelope for the $|\Gamma|^2$ function and coincides with it only at the set of specific points indicated.

It can be seen that Eq. (19) contains the locus of the maxima of $|\Gamma|^2$, which occur at the minimum impedance points for the terminated dielectric column. In the neighborhood of these maxima of the reflected signal, $|\Gamma|^2$ is a relatively slowly varying function.

The magnitude of the minima of $|\Gamma|^2$, as the dielectric column length is increased, decreases to a minimum minimum value, which is usually very close to zero, and then increases, approaching $|\Gamma_\infty|^2 = T$ as a limit. These minima, however, do not occur at exactly the $\lambda_d/2$ or odd $\lambda_d|4$ points. The behavior of the reflected signal in the neighborhood of the minimum points is considered in more detail in Appendix B.

By using a micrometer drive to move the terminating plunger through the liquid dielectric column and recording the positions giving the maximum reflected signal, the wave-length in the dielectric-filled guide may be determined quite accurately. Very reproducible results are obtained from the positions of the successive maxima. The values of λ_d determined from the positions of the successive minima are less reliable, however, the differences in the positions for the first few minima giving values which are too small.

B. Experimental Equipment

A block diagram of the experimental unit is shown schematically in Fig. 7. Two such systems were constructed, one operating at 24,000 megacycles and one at 10,000 megacycles. Both units employ wave-guide components using rectangular guide which is operated in the $TE_{1,0}$ mode. The electrical operation of the system follows the standard experimental procedures developed for measurements in general in the microwave region.

The dielectric cell consists of a standard section of either solid coin silver, $\frac{1}{2}'' \times \frac{1}{4}''$ O.D. $\times 0.040''$ wall, or silver plated, $1'' \times \frac{1}{2}''$ O.D. $\times 0.050''$ wall, rectangular guide which is surrounded by a thermostatically controlled constant temperature bath. The volume of the

liquid sample required depends on the loss factor and should be sufficient to give a length of dielectric column from about 1.5 to 5 or more wave-lengths in the liquid-filled guide.

The liquid-filled section of guide may be separated from the remainder of the system by some form of lossless solid dielectric diaphragm which is adjusted so that it introduces only a negligible impedance transforming action. Two forms of such a window which were used are shown in Fig. 8, and a number of other variations are possible. The diaphragms shown are thick sections made of Teflon, a very low loss plastic, which are one-half wave-length long and thus do not affect the circuit electrically. Since the measurements to determine the loss of the liquid sample are always made for an impedance minimum at the face of the liquid, the positions of the solid diaphragms are adjusted so that there is a voltage maximum, and therefore the minimum loss, at the flange-flange joint between the dielectric cell and the rest of the system.

An alternate type of window is one consisting merely of a very thin mica sheet or film of Teflon clamped between a choke-flange joint. For a sufficiently thin section, i.e., electrically thin, the impedance transformation introduced has a negligible effect on the magnitude of the observed reflection coefficient. The junction loss is somewhat greater in this case, however, but its power loss is still negligible relative to the power absorption by the dielectric sample for medium and high loss materials.

The solid dielectric diaphragm at the input to the cell is necessary both to fix the location of one end of the liquid dielectric column and to prevent the formation of a meniscus which might introduce an appreciable curvature into the dielectric discontinuity if the liquid cell were to be inverted and no solid membrane used. For plane dielectric discontinuities perpendicular to the axis of a uniform wave guide, there will be no higher mode generation and thus no appreciable error will be introduced due to the conversion of power into higher modes at the input to the dielectric cell. The flange junction is the only discontinuity in the metallic walls of the guide, and the higher mode generation is a minimum for this type of recessed discontinuity, particularly if it is located at a voltage maximum point in the guide.

The two types of reflecting plungers used as terminations are shown in Fig. 9. The short-circuiting plunger is of the standard choke type of construction. Both the choke sections of plunger (A) and the quarter-wave-length impedance transforming section of plunger (B) must be filled with a low loss solid dielectric. Teflon was used here also since its electrical, mechanical, and chemical properties are all quite suitable. Small grooves were cut along the sides of the plungers to allow free passage for the liquid.

C. Calculation of Dielectric Constants

After determining the constants of the apparatus, the liquid cell is filled with the dielectric sample which is allowed to reach thermal equilibrium. The reflecting terminating plunger is then slowly withdrawn and the amplitudes and positions of the successive maxima of the reflection coefficient recorded. The wave-length in the cell, λ_d, is twice the separation between adjacent maxima, and, for low loss dielectrics, ϵ' could be immediately computed from Eq. (16).

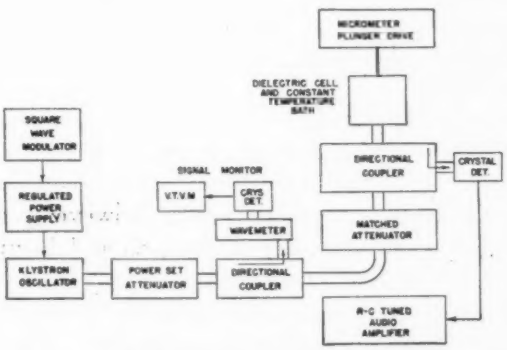

FIG. 7. Block diagram of experimental equipment.

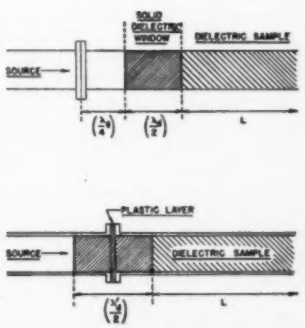

FIG. 8. Construction of solid dielectric membranes.

For medium and high loss dielectrics, however, the dissipation factor, D, must also be determined before computing ϵ'.

The dissipation factor for the system, D, may be computed analytically by the method of successive approximations as follows.

Let M_n be the ratio of the maximum of the observed reflected signal for $L=n\lambda_d$ to that for an effectively infinite dielectric column,†† so that

$$M_n=[|E^-|^2_{L=n\lambda_d}]/[|E^-|^2_{L=\infty}]$$
$$=|\Gamma_n|^2/|\Gamma_\infty|^2, \quad (20)$$

where

$n=1/2, 1, 3/2, \cdots$ for the short-circuit plunger;
$n=1/4, 3/4, 5/4, \cdots$ for the open-circuit plunger.

Then, in order to simplify the form of the final equation, define

$$x=(\lambda_d/\lambda_g), \quad (21)$$

$$y=(1-x)/(1+x). \quad (22)$$

Physically, x represents the characteristic impedance of a guide filled with an ideal dielectric having the same λ_d and y the corresponding reflection coefficient for an infinitely long column.

Substituting Eq. (19) into Eq. (20) results in a quadratic equation for $\exp(-2n\alpha_d\lambda_d)$, which may be solved for the attenuation per wavelength, $(\alpha_d\lambda_d)$ in nepers, to give the expression:

$$(\alpha_d\lambda_d)=(1/2n)\ln[K_1(1+(1+K_2)^{\frac{1}{2}})], \quad (23)$$

where

$$K_1=C_1(1-M_nT)/(M_n-1), \quad (24)$$

$$K_2=C_2(M_n-1)[(1-M_nT^2)/(1-M_nT)^2], \quad (25)$$

or, to a first approximation, K_1 and K_2 may be expressed as

$$K_1\approx(1/y)(1-y^2M_n)/(M_n-1), \quad (24a)$$

$$K_2\approx(M_n-1)[(1-y^4M_n)/(1-y^2M_n)^2]. \quad (25a)$$

The exact expressions for T, C_1, and C_2 are:

$$T=|\Gamma_\infty|^2=|(Z_d-1)/(Z_d+1)|^2 \quad (26a)$$

$$=\frac{1-x(1-x/2)[1+\cos(\tan^{-1}D)]}{1+x(1+(x/2))[1+\cos(\tan^{-1}D)]} \quad (26b)$$

$$\approx y^2[1+D^2(x/(1-x^2)^2)-\cdots]; \quad (26c)$$

$$C_1=(F/T)=[1-|Z_d|^2]/[|1-Z_d|^2] \quad (27a)$$

$$=\frac{1-\frac{1}{2}x^2[1+\cos(\tan^{-1}D)]}{1-x(1-(x/2))[1+\cos(\tan^{-1}D)]} \quad (27b)$$

$$\approx(1/y)[1-\tfrac{1}{2}D^2[x(1+x)/(1-x^2)^2]+\cdots]; \quad (27c)$$

$$C_2=(T/F^2)=\frac{|1-Z_d|^2\cdot|1+Z_d|^2}{(1-|Z_d|^2)^2} \quad (28a)$$

$$=1+x^2\sin^2(\tan^{-1}D)/[1-x^2\cos^2(\tfrac{1}{2}\tan^{-1}D)]^2 \quad (28b)$$

$$\approx 1+D^2[x^2/(1-x^2)^2]-\cdots. \quad (28c)$$

The dissipation factor, D, is then determined by the equation

$$D=\tan[2\tan^{-1}(\alpha_d\lambda_d/2\pi)]$$
$$=\tan\{2\tan^{-1}[2.303\log K_1(1+(1+K_2)^{\frac{1}{2}})/4\pi n]\}. \quad (29)$$

The determination of D from the experimental data is then evidently a process of successive approximations, which, however, converges very rapidly. For $D\leqslant 0.1$, K_1 and K_2 may be considered as functions solely of y and M_n and only one calculation need be made. For larger values of dielectric loss, the first value obtained for D must be used to recompute K_1 and

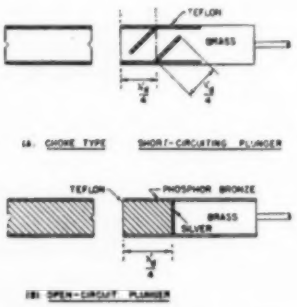

FIG. 9. Construction of terminating plungers.

†† It is not essential to refer the observed reflection coefficients to $|\Gamma_\infty|$ since the ratio of any two maxima of $|\Gamma|$ could be used to calculate the loss factor. The use of $|\Gamma_\infty|$ simplifies the equations, however, and it can easily be observed experimentally. The condition for an equivalent infinite length of dielectric column is obtained within a few wave-lengths for high and medium loss liquids. For lower loss liquids, the value of $|\Gamma_\infty|$ may be estimated from the average of successive maxima and minima of $|\Gamma|$ for lengths of the liquid column from two to three times larger than that for the minimum minimum value of $|\Gamma|$, or a lossy tapered plunger may be substituted for the reflecting plunger.

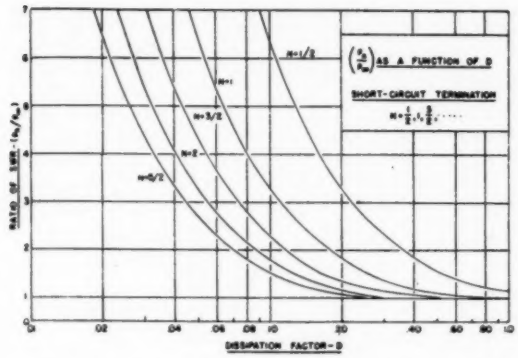

FIG. 10. Ratio of SWR's, (ρ_n/ρ_∞), for a short-circuit plunger, $n=\frac{1}{2}, 1, \frac{3}{2}, \cdots$.

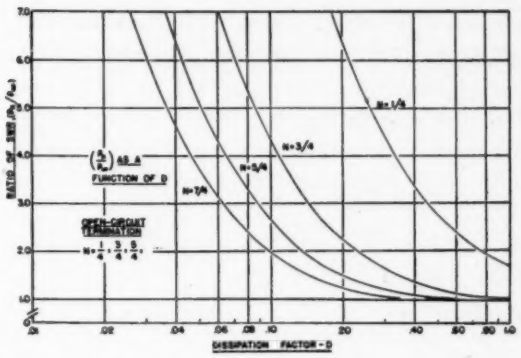

FIG. 11. Ratio of SWR's, (ρ_n/ρ_∞), for an open-circuit plunger, $n=\frac{1}{4}, \frac{3}{4}, \cdots$.

K_2 to determine a second, closer approximation for D. If $D \leqslant 0.3$, then the approximate form of Eqs. (26)–(28) may be used. For $0.3 < D \leqslant 1.0$, the D^2 term in these approximate equations should be replaced by $4\sin^2(\frac{1}{2}\tan^{-1}D)$ for (26) and (27), and by $[\sin^2(\tan^{-1}D)]$ for (28). Since values of $D > 1.0$ are very seldom obtained for pure non-conducting compounds, the exact defining equations for the factors T, C_1, and C_2 need not be used.

Having measured λ_d and calculated D, the constants of the medium, ϵ', ϵ'', and $\tan\delta$, may be calculated exactly from Eqs. (16), (17), or (2).

D. Graphical Determination of Loss Factor

The dissipation factor of the system may be determined by an alternate graphical method which involves less computational work. The ratios of the reflection coefficients, M_n, cannot be plotted in any simple manner as functions of the dissipation factor, D. This can be done, however, for the ratio of the maxima of the standing wave ratio to the standing wave ratio for an effectively infinite length dielectric column.

The experimental procedure for this second method is essentially the same as that described previously. A unidirectional coupler is used to observe the variation in the reflected signal as the length of the dielectric column is changed in order to determine the positions for the maxima of the reflection coefficient. Since the SWR is desired at these points, a slotted line may be inserted into the system between the dielectric cell and the unidirectional coupler to measure the SWR's, ρ_n and ρ_∞, directly. This is not essential, however, since the observed value of λ_d may be used in conjunction with the measured ratio of the reflection coefficient, M_n, to compute the ratio of the standing wave ratios, thus using only the data obtained with the unidirectional coupler. This is outlined in more detail in Appendix A.

Since the magnitude of the reflection coefficient, and therefore the SWR, is a slowly varying function in the neighborhood of these maximum points, a small deviation in the position of the plunger from the exact $\lambda_d/4$ or $\lambda_d/2$ points will introduce only a very small error into the measured value of $|\Gamma_n|$ or of ρ_n.

The determination of the dissipation factor may then be made as follows. Let

$$\rho_n = (1+|\Gamma_n|)/(1-|\Gamma_n|) = VSWR,$$

where

$n = 1/2, 1, 3/2, \cdots$ for the short-circuit plunger;
$n = 1/4, 3/4, 5/4, \cdots$ for the open-circuit plunger.

Then at the set of points at which ρ_n is measured, the per unit input impedance of the dielectric column is

$$\begin{aligned} Z_n &= |Z_d| \cdot e^{j\phi_d} \cdot \tanh(n\alpha_d\lambda_d), \\ Z_\infty &= |Z_d| e^{j\phi_d}. \end{aligned} \tag{30}$$

Substituting these expressions into the equation for the SWR, expanding the radicals into power series, and collecting terms results in the equation

$$\frac{\rho_n}{\rho_\infty} = \frac{1}{\tanh(n\alpha_d\lambda_d)}\left[1 - 4\sin^2(\tfrac{1}{4}\tan^{-1}D) \times \frac{|Z_d|^2 - |Z_n|^2}{(1-|Z_d|^2)(1-|Z_n|^2)} + \cdots\right] \tag{31}$$

in which the characteristic impedance, $|Z_d|$, which involves ϵ', is eliminated except in a correction term which is small even for large values of the dissipation factor. Thus the ratio of ρ_n to ρ_∞, to a very good approximation, has the form

$$\rho_n/\rho_\infty \approx \coth(n\alpha_d\lambda_d) = \coth[2\pi n \tan(\tfrac{1}{2}\tan^{-1}D)]. \quad (32)$$

Two sets of curves of this ratio *vs.* D are plotted in Figs. 10 and 11 for $n=\frac{1}{2}, 1, \frac{3}{2}, \cdots$ and for $n=\frac{1}{4}, \frac{3}{4}, \cdots$, respectively. The dissipation factor can then be read directly from the appropriate curve using the experimentally measured ratio of the SWR for any one value of n to the SWR for an effectively infinite dielectric column.

The value of D obtained graphically in this way agrees within about 2–4 percent or less with that computed algebraically, and the computational time required is negligible. If more accurate results are desired, this value may be used as the first approximation to determine the correction terms in the algebraic equations, and then $(\alpha_d\lambda_d)$ or D computed either from Eq. (31) or from Eqs. (23) to (29) of the previous section. Since the initial value for D is very close to the correct one, only one calculation need be made.

APPENDIX A

Conversion from $|\Gamma_n|^2/|\Gamma_\infty|^2$ to (ρ_n/ρ_∞):

If only the relative magnitude of the reflected signal is observed, then the ratio of any two reflection coefficients may be determined exactly, although the absolute magnitude of either one is unknown. A ratio of two reflection coefficients cannot be converted directly into a ratio of the corresponding SWR's, however, since additional information is required.

If the wave-length in the dielectric is known, then ρ_∞ and $|\Gamma_\infty|$ may be expressed as functions of $x=(\lambda_d/\lambda_0)$ and of D as follows:

$$\rho_\infty = (1/x)[1+(1/(1-x^2)) \times \sin^2(\tfrac{1}{2}\tan^{-1}D) - \cdots], \quad (33)$$

$$|\Gamma_\infty| = y[1+(2x/(1-x^2)^2) \times \sin^2(\tfrac{1}{2}\tan^{-1}D) - \cdots], \quad (34)$$

which are usually valid within about 1 percent or less for $D \leqslant 1.0$. For $D \leqslant 0.25$, the expression "$\sin^2(\frac{1}{2}\tan^{-1}D)$" may be replaced by "$D^2/4$."

Then to convert from the ratio $M_n=(|\Gamma_n|^2/|\Gamma_\infty|^2)$ to the ratio (ρ_n/ρ_∞), the equation

$$\rho_n/\rho_\infty = (1/\rho_\infty) \cdot \{[|1/\Gamma_\infty|+(M_n)^{\frac{1}{2}}]/[|1/\Gamma_\infty|-(M_n)^{\frac{1}{2}}]\} \quad (35)$$

may be used. This may then be used in conjunction with the curves of Fig. 10 or 11 to obtain an approximate value of D. However, since ρ_∞ and $|\Gamma_\infty|$ are also affected by D, a successive approximation method will still be required unless at least one SWR, such as ρ_∞, is actually measured.

APPENDIX B

Dielectric Column Lengths for Minimum Reflected Power

For a dielectric column terminated by a reflecting plane, the maximum values of the reflected power at the face of the dielectric sample occur for lengths which are multiples of $\lambda_d/2$ for a short-circuit termination or odd multiples of $\lambda_d/4$ for an open-circuit termination. The magnitude of $|\Gamma|^2$ at these positions is given by Eq. (19).

Similarly, the sets of values of $|\Gamma|^2$ for dielectric column lengths which are odd multiples of $\lambda_d/4$ for a short-circuit termination, or multiples of $\lambda_d/2$ for an open-circuit termination, are given by the equation,

$$|\Gamma_n|^2 = \frac{T-2Fe^{-2n\alpha_d\lambda_d}+e^{-4n\alpha_d\lambda_d}}{1-2Fe^{-2n\alpha_d\lambda_d}+Te^{-4n\alpha_d\lambda_d}}, \quad (36)$$

$n=1/4, 3/4, \cdots$ for a short-circuit termination;

$n=1/2, 1, 3/2, \cdots$ for an open-circuit termination.

These dielectric column lengths are in the immediate vicinity of the lengths which result in a minimum value of $|\Gamma|^2$, but the magnitude of the actual minima may be appreciably different from the values given by Eq. (36), which applies only at the exact $\lambda_d/4$ or $\lambda_d/2$ points. The variation of $|\Gamma|^2$ in the neighborhood of the positions for minimum reflected signal may be seen in Figs. 4–6. The locus of the values of $|\Gamma_n|^2$ from Eq. (36) is plotted on these figures as a dotted curve. This curve does not represent a lower envelope for the $|\Gamma|^2$ function and coincides with it only at the set of discrete points indicated.

The magnitude of the minima of $|\Gamma|^2$, as the dielectric column length is increased, decreases

to a minimum minimum value, which is usually very close to zero, and then increases, approaching $|\Gamma_\infty|^2$ as a limit. This minimum minimum value occurs for a dielectric column length which depends on the loss tangent of the medium, being longer for the lower loss media. The actual minima of $|\Gamma|^2$, although they occur for values of dielectric column length which are only slightly greater than the exact multiples of $\lambda_d/4$ or $\lambda_d/2$, may have values which are quite appreciably smaller than the values given by Eq. (36) for those minima occurring for column lengths less than that for the minimum minimum value. For values of L greater than this, the magnitudes of the actual minima are very close to the values occurring at the exact $\lambda_d/4$ or $\lambda_d/2$ lengths.

The approximate dielectric column length for this minimum minimum value of $|\Gamma|^2$ may be determined very closely from Eq. (36) by considering it to represent a smooth curve. Its minimum value then evidently occurs for the value of L given by the equation

$$L=(1/2\alpha_d)\ln_e[(1+|Z_d|)^2/1-|Z_d|^2]. \quad (37)$$

The length of the dielectric column, therefore, which is an odd multiple of $\lambda_d/4$ for the short-circuit plunger or a multiple of $\lambda_d/2$ for the open-circuit plunger, and which is closest to this value of L, is in the immediate vicinity of (but slightly shorter than) the length resulting in the minimum value of $|\Gamma|^2$.

Erratum: On the One-Dimensional Theory of Steady Compressible Fluid Flow in Ducts with Friction and Heat Addition

[J. App. Phys. 18, 891 (1947)]

BRUCE L. HICKS
Ballistic Research Laboratories, Aberdeen Proving Ground, Maryland
DONALD J. MONTGOMERY
Office of Naval Research (London Branch), London, England
AND
ROBERT H. WASSERMAN
University of Chicago, Chicago, Illinois

THE attention of the senior author has been called to a paper by D. G. Samaras.[1] Reference in our article should have been made to this paper which represents part of the theory of one-dimensional flow developed in England during the war.

The references in our paper are believed to be reasonably complete through 1945.

[1] D. G. Samaras, Can. J. Res. (F)24, 272 (1946).

A Method of Determining the Angle of Arrival

A. W. Straiton, W. E. Gordon, and A. H. LaGrone
Electrical Engineering Research Laboratory, The University of Texas, Austin, Texas
(Received October 6, 1947)

A method is presented for determining the angle of arrival of the direct and reflected wave for line of sight cases. The method assumes one direct and one reflected wave. The phase difference equipment, as developed by the Electrical Engineering Research Laboratory, measures the difference in phase at 3.2-cm wave-length between two points separated vertically by ten feet [F. E. Brooks, Jr. and C. W. Tolbert, *Equipment for Measuring Angle-of-Arrival by the Phase Difference Method*, Electrical Engineering Research Laboratory, Report No. 2, May 1946] and the signal strength at each point. The normal procedure involves the raising of either transmitter or receiver while the other is held at a fixed level. The data to which the method is applied were collected at the Navy Electronics Laboratory desert site near Gila Bend, Arizona, during April 1947. The results are compared to calculations based on the meteorologically measured distribution of the refractive index and ray theory.

I. METHOD

FOR line of sight propagation the angles of arrival of the direct and reflected wave, θ_D and θ_R, respectively, are derived in the Appendix (Eqs. (14) and (15)) in terms of the phase difference between two points, $d\beta$, and the signal strengths of the direct, reflected, and resultant waves.

$$\theta_D = (d\beta + A_s - A_0)/600,$$
$$\theta_R = \theta_D - (T_s - T_0)/600.$$

The quantities A and T may be expressed as functions of the ratios of signal strengths (Appendix Eqs. (5) and (7)), but are more readily evaluated graphically by means of Figs. 1, 2, and 3. From Fig. 1 and the signal strength-height curve, a value of K is obtained. At the particular height for which values of angles of arrival are desired, the signal strength ratio of Figs. 2 and 3 is evaluated and with K, values of A and T are determined. The above equations are evaluated by substitution.

Comparatively few of the signal strength-height curves showed the characteristics associated with a constant reflection coefficient, K. The difference between the signal strength maxima and minima were frequently different for the two receiving antennas and the maxima for a single antenna were frequently different.

In all cases, the value of K was determined separately for each antenna. In addition, the value of K was determined individually for each

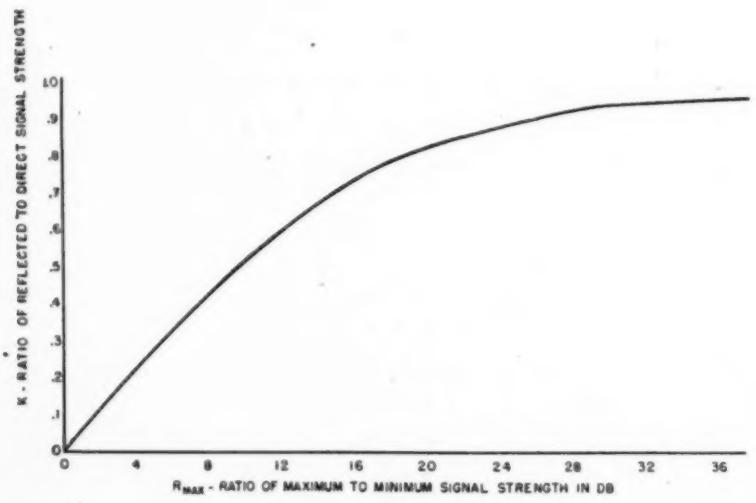

FIG. 1. Curve for finding reflection coefficient.

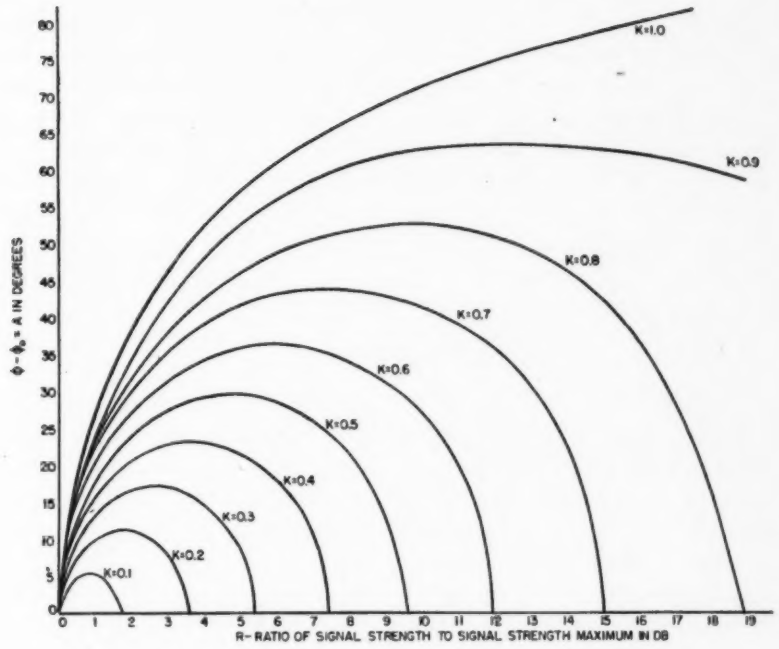

FIG. 2. Curve for finding A.

transmitter height considered. The procedure for doing this was to plot the maxima and minima signal strength values as a function of height. A straight line was then drawn between maxima and the signal strength was assumed constant above the highest maximum reached and below the first maximum in the interval where line of sight prevails. The same procedure was used for the minima. At any transmitter height, the value of K was found from the decibel difference between the maximum and minimum lines corresponding to that height.

II. EXAMPLE OF METHOD

1. The data.—The data for an example of this kind are shown in Fig. 4(A). The phase angles are relative to the zero phase angle determined from a nearby reference transmitter. The signal strengths are free space values but only the relative values are needed for the angle of arrival determinations.

2. Determination of K.—From the signal curves in Fig. 4(A), the ratio of the minimum to maximum signal strength is seen to be 10.3 db. Then from the K curve in Fig. 1, a value of 0.53 is found for K, corresponding to the signal strength ratio of 10.3 db.

3. Determination of A and T.—For a transmitter height of 70 feet, the ratio of the signal to the maximum signal strength is seen to be 2.2 db for the z antenna and 3.7 db for the circle antenna. From Fig. 2, the values of A corresponding to these points are found to be

$$A_z = 26°, \quad A_0 = 30°.$$

Similarly, from Fig. 3, the values of T are found to be

$$T_z = -83°, \quad T_0 = -106°.$$

4. Determination of $d\beta$.—The phase difference between the z and 0 antennas is read directly from the phase curve. For a height of 70 feet this phase difference is seen to be $-148°$.

5. Determination of angle of arrival.—The angle of arrival of the direct wave is found from Eq. (14) to be

$$\begin{aligned}\theta_D &= (d\beta + A_z - A_0)/600 \\ &= (-148+26-30)/600 \\ &= -0.253°.\end{aligned}$$

Similarly, the angle of arrival of the reflected ray, θ_R, is determined from the relationship

$$\begin{aligned}\theta_R &= \theta_D - (T_z - T_0)/600 \\ &= -0.253-(-83+106)/600 \\ &= -0.291°.\end{aligned}$$

6. Angle of arrival height curves.—By repeating the process outlined above for a number of

different transmitter heights, the variations of the angle of arrival of the direct and reflected rays with height may be obtained. The angle of arrival curves corresponding to the phase difference and signal strength curves of Fig. 4(A) are shown in Fig. 4(B). The characteristic of the angles of arrival *vs.* height curves will be discussed later in the report.

III. APPLICATION OF THE METHOD

1. 1757 April 27, 1947

a. Data.—The data for this time are shown in Fig. 5. The radio data consist of the phase difference and signal strength curves as functions of the height of the transmitter. The meteorological data are shown by the M curve. (Modified index of refraction *vs.* height.)[1]

b. Angles of arrival graphs.—The angles of arrival of the direct and reflected rays for the time in question are shown in Fig. 6. The solid dots indicate the angle of arrival of the direct ray and the circles indicate the angle of arrival of the reflected ray. The reference line for the direct rays on the angle of arrival curve is for the values obtained from ray tracing procedures using small height intervals to compensate for the varying gradient.

c. Reference line for reflected rays.—The reference line for the reflected rays was obtained from the path profile corresponding to an M gradient of 0.04 per foot, which was the average for this test. This profile with a greatly exaggerated vertical scale is shown in Fig. 7. From this profile, it is seen that the section between 6.5 and 17 miles is almost a straight line (shown dotted in Fig. 7), and the plane determined by the line was taken as the reflecting plane. (A similar analysis is discussed in detail by Hamlin, *et al.*)[2]

2. Additional Examples of Angles of Arrival Measurements

a. 1013 April 29, 1947.—The phase difference, signal strength, and M curves for this time are shown in Fig. 8 and the corresponding angle of arrival graphs are shown in Fig. 9.

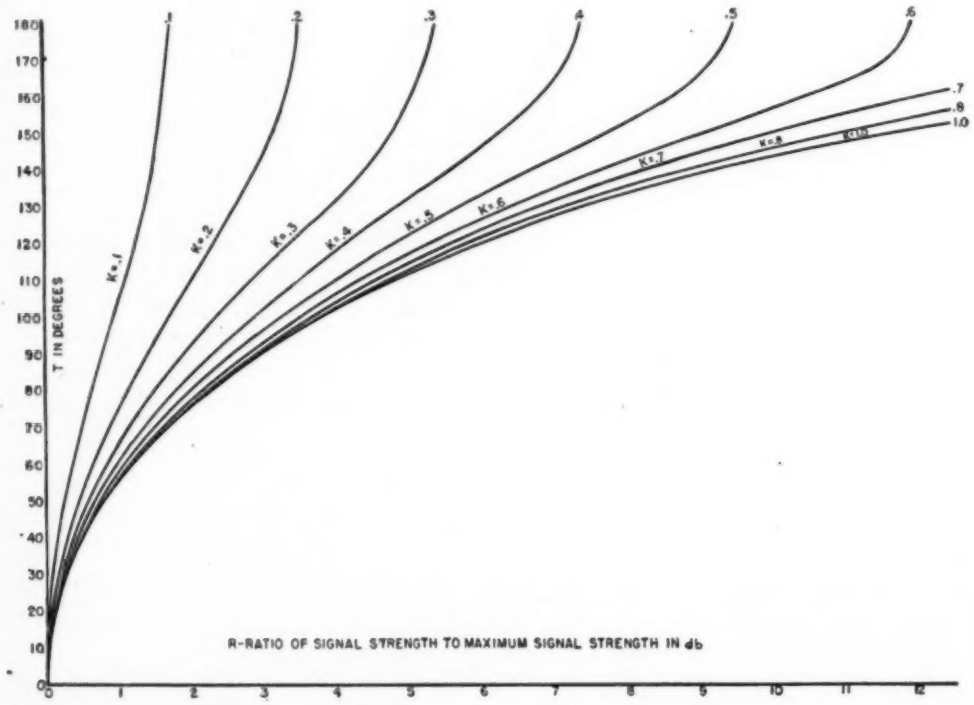

FIG. 3. Curve for finding T.

[1] $M=(79/T)(P+4800e/T)+0.048h$ where T, P, e, and h are temperature in degrees Kelvin, atmospheric pressure in millibars, vapor pressure in millibars, and height in feet. This makes use of a plane earth representation. For the standard atmosphere $dM/dh=0.036$ M units per foot.

[2] E. W. Hamlin, W. E. Gordon, and A. H. LaGrone, *X-Band Phase Front Measurements in Arizona During April 1946*, Electrical Engineering Research Laboratory, Report No. 6, February 1947.

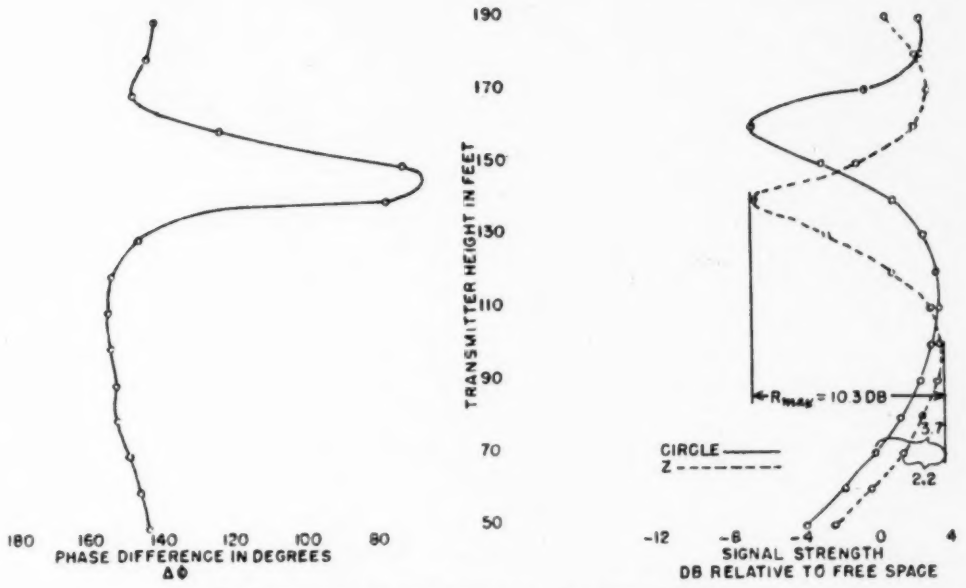

PHASE DIFFERENCE AND SIGNAL STRENGTH CURVES
4A

FIG. 4.

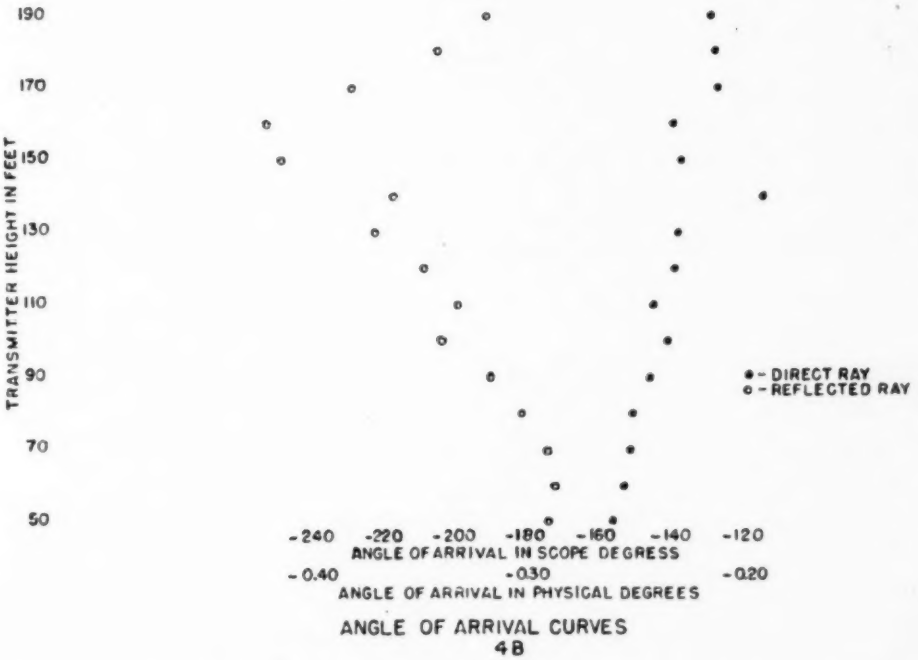

ANGLE OF ARRIVAL CURVES
4B

SENTINEL - GILA BEND PATH RECEIVER HEIGHT 200 FEET 23 APRIL 1947 TIME 1235

b. Other examples.—The angle of arrival on April 28, 1947, at 0834 and on April 29 at 1123 and 1731 are shown in Figs. 10, 11, and 12. Numerous angle of arrival height curves were obtained with characteristics similar to those shown.

3. Discussion

It is fully realized that the ray tracing cannot be relied upon to give exact results for the complicated profile and variable M gradient present. However, the ray tracing was used only as a means of obtaining a comparison with the

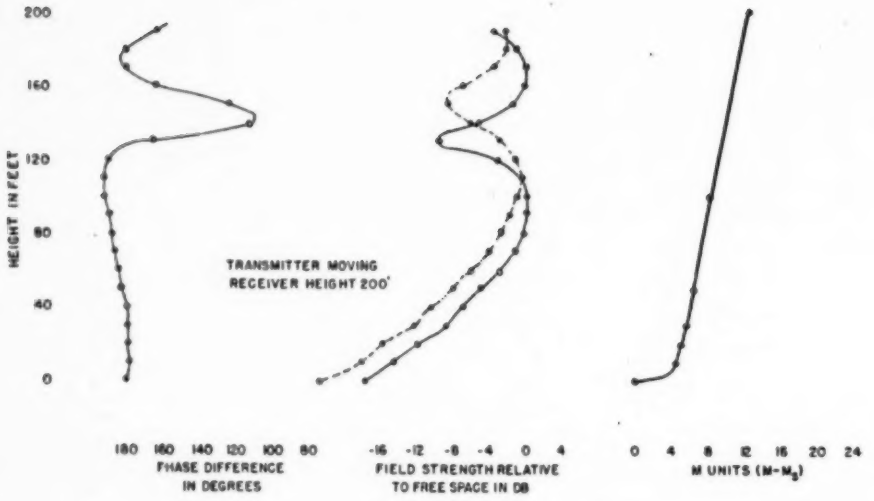

FIG. 5. Data for April 27, 1947 at 1757.

measured angles of arrival. The direct ray cleared the rise shown on the profile at 20 miles by less than a Fresnel zone for transmitter heights less than 75 feet and was blocked by this rise for transmitter heights less than 10 feet.

For the reflected ray, the situation was even more complicated. For most transmitter heights, the reflected ray would not clear the rise at 20 miles by a Fresnel zone. In addition, lines drawn from the receiver to the ends of the available reflecting plane and from there to the transmitter were commonly greater than the line to and from the "reflecting point" by less than one wave-length. The point *A* on the angle of arrival curves indicates the lowest height for which the reflection from the plane surface chosen would clear the rise at 20 miles. The point *B* indicates the transmitter height at which the reflection point for the plane chosen would move into the irregular section of the profile starting at the point *B* of Fig. 7.

The agreement of the measured angle of arrival of the direct ray and the angles from ray tracing is good. Although this deviation is close

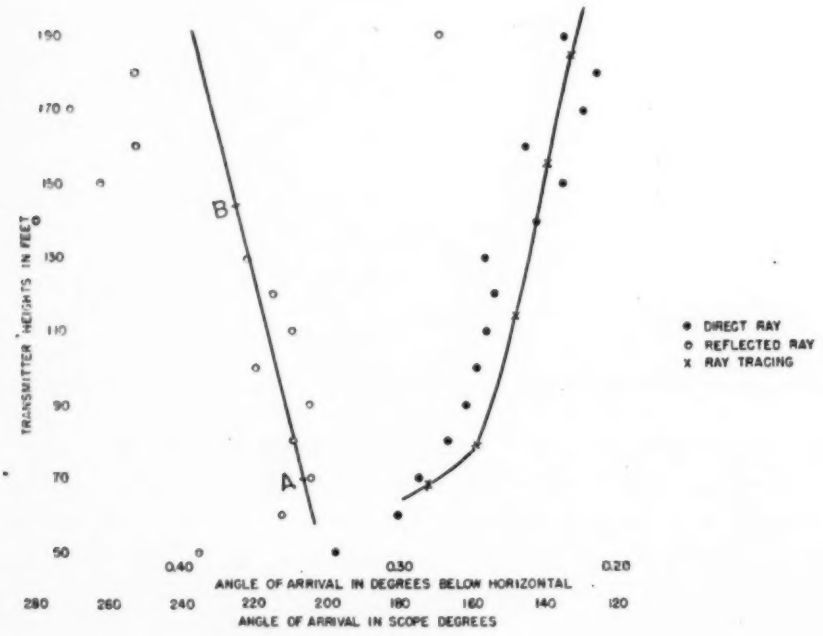

FIG. 6. Angle of arrival for April 27, 1947 at 1757.

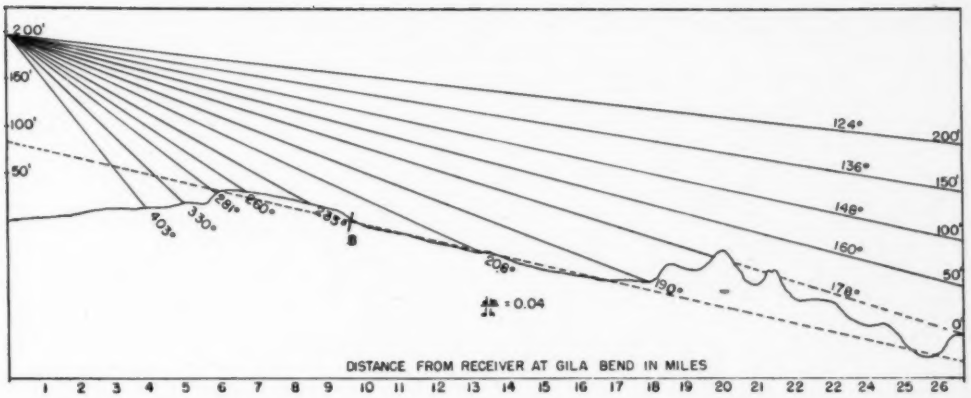

FIG. 7. Path profile.

to the limit of accuracy of the measurements, it is felt that the variations may be partly accounted for by the limitations of ray tracing.

The agreement of the measured reflected ray angles of arrival with the reflection from the arbitrary plane chosen was reasonably good considering all the assumptions involved in using the reference plane. From the profile of Fig. 7, it is seen that the equivalent reflecting point moves to the left along the reflecting plane chosen as the transmitter height is increased. When the transmitter reaches a height of 180 feet, the reflecting point has passed the limit of the available reflecting plane. The angles of arrival for a transmitter height of 190 feet changed radically from the preceding trend and may be due to the change in reflecting surface. The location of this point was duplicated on a number of the tests. The accuracy of the measurements for the low signal strength around 140 and 150 feet is much lower and the positioning of these reflected ray points is not as accurate.

It is noticed that in some of the examples the angle of arrival tends to remain constant for lower transmitter height with the ray apparently coming from the center of the level reflecting surface near 14 miles from the receiver. Since the transmitter is shielded from a considerable section of this reflecting surface for these heights, this would seem to indicate that the wave is diffracted over the rise at 20 miles and reflected from the plane.

The data for Fig. 12 indicate a fairly constant discrepancy of 15 scope degrees between the measured angles of arrival and the angles of arrival determined by ray tracing. It is difficult to account for this deviation although it is believed to be due to discrepancies in measuring

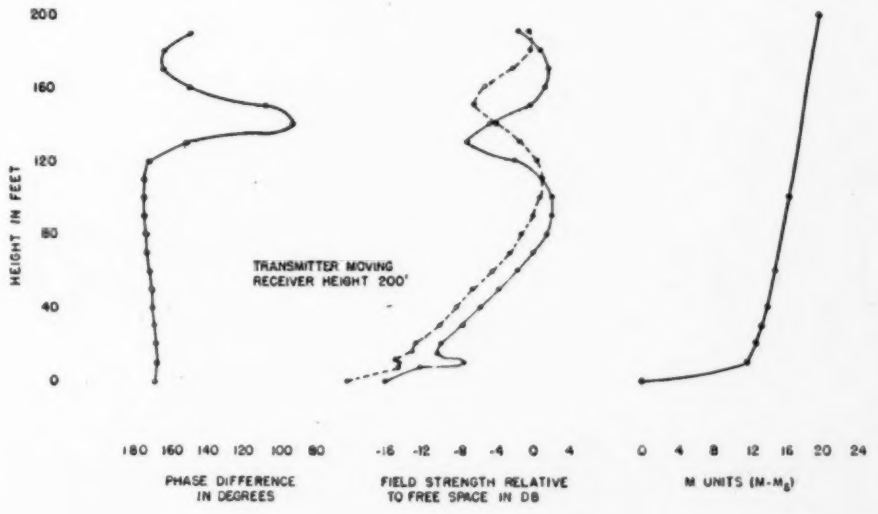

FIG. 8. Data for April 29, 1947 at 1013.

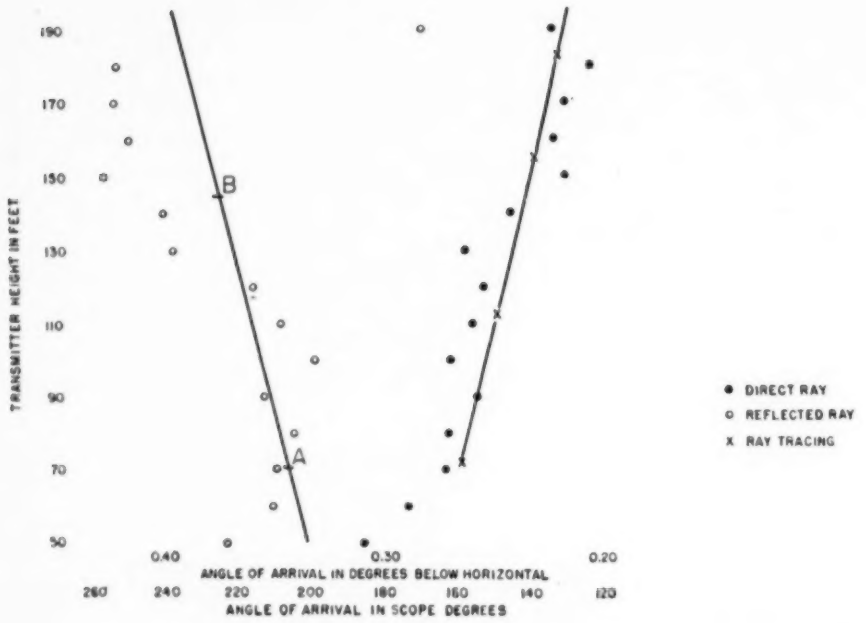

FIG. 9. Angle of arrival for April 29, 1947 at 1013.

the reference angle and to failure to level the receiving antennae accurately.

IV. CONCLUSIONS

The method is applicable in the optical region for a single pair of direct and reflected waves. The determination of the angles of arrival of the direct and reflected waves by the method herein described from the measurements presented by the Electrical Engineering Research Laboratory Phase Difference Equipment is consistent with meteorologically measured distributions of the refractive index.

V. APPENDIX

Derivation of Angle of Arrival Equations

1. Symbols.—The following symbols are used in the derivation of the angle of arrival equations.

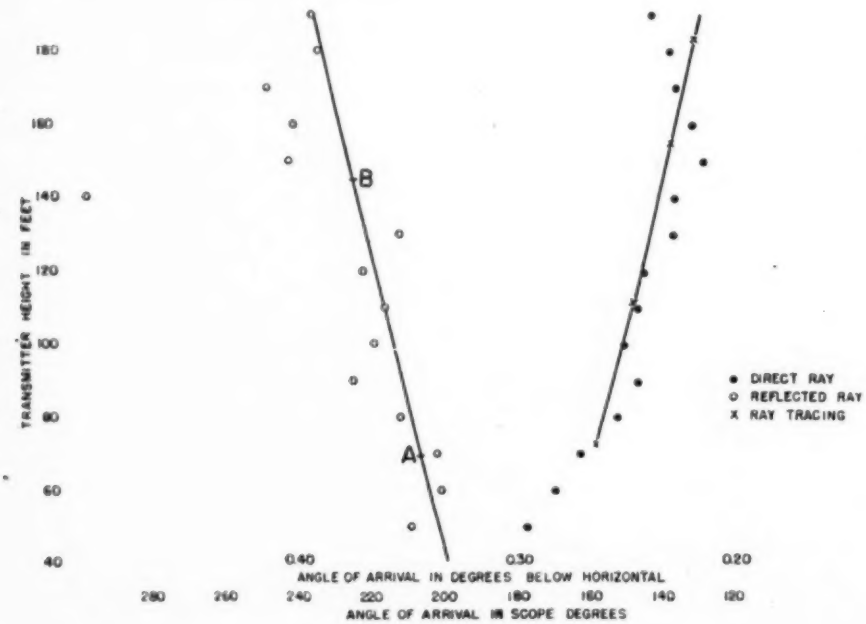

FIG. 10. Angle of arrival for April 28, 1947 at 0834.

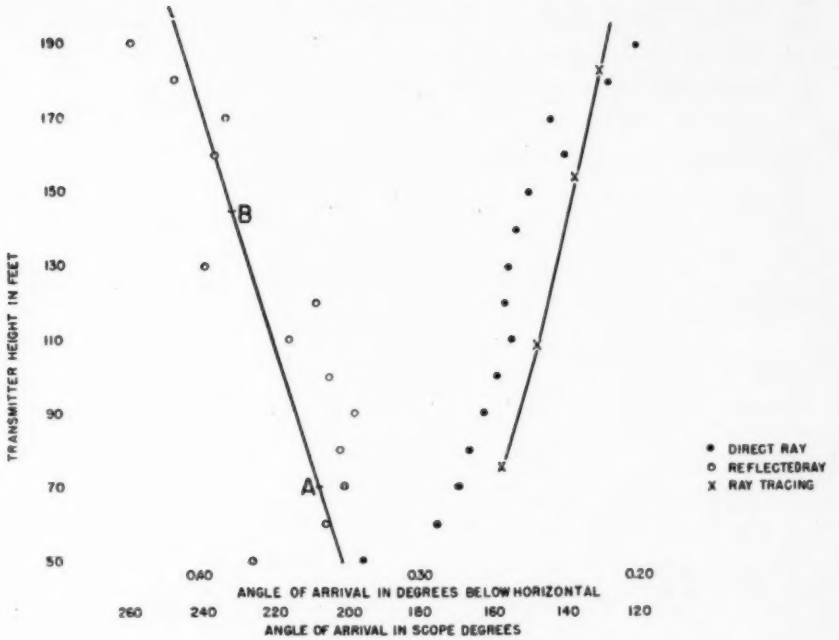

FIG. 11. Angle of arrival for April 29, 1947 at 1123.

V_D—signal strength of direct wave in volts per meter.
KV_D—signal strength of reflected wave in volts per meter.
V—signal strength of resultant wave in volts per meter.
β—phase of resultant wave.
β_D—phase of direct wave.
β_R—phase of reflected wave.
β_0, β_{D0}, β_{R0}, β_z, β_{Dz}, and β_{Rz}—the subscripts 0 and z applied to β indicate phase at the lower and upper antennae, respectively.
$d\beta$—phase difference between z and 0 antennae.
R—ratio of signal strength to signal strength maximum.
R_{max}—ratio of minimum to maximum signal strength.
T—$\beta_D - \beta_R$.
A—$\beta - \beta_D$.
D—separation of z and 0 antennae.
L—wave-length.
θ_D—angle of arrival of direct ray in degrees.
θ_R—angle of arrival of reflected ray in degrees.

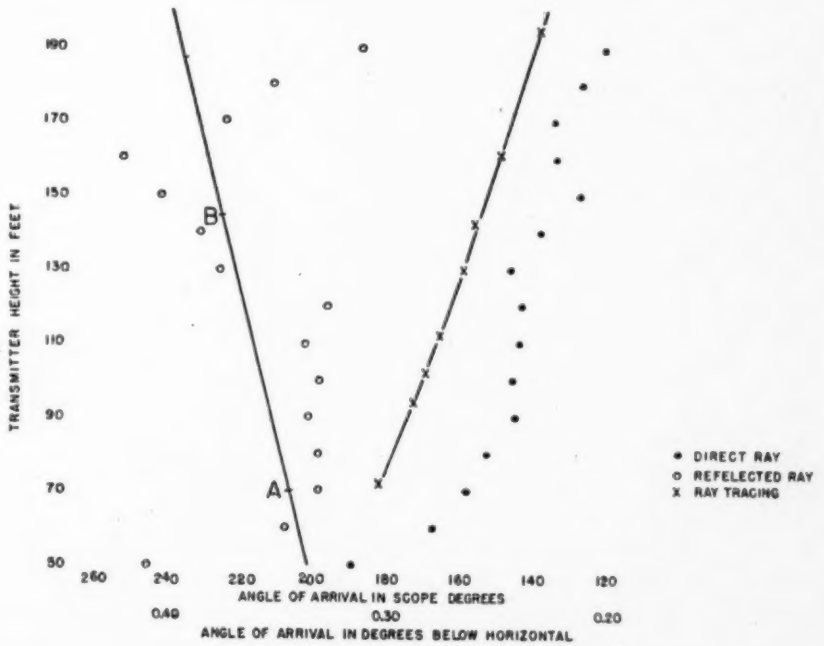

FIG. 12. Angle of arrival for April 29, 1947 at 1731.

2. Signal strength relationships.—If a direct and reflected ray are received simultaneously, the combined signal strength is given by

$$V = V_D(1+2K\cos(\beta_D-\beta_R)+K^2)^{\frac{1}{2}}. \quad (1)$$

When $\cos(\beta_D-\beta_R)=1$, V will be maximum indicated as V_{max}, and

$$V_{max}/V_D = 1+K. \quad (2)$$

When $\cos(\beta_D-\beta_R)=-1$, V will be minimum indicated as V_{min} and

$$V_{min}/V_D = 1-K. \quad (3)$$

Combining Eqs. (2) and (3), the value of K may be found as

$$K=(V_{max}/V_{min}-1)/(V_{max}/V_{min}+1) = (R_{max}-1)/(R_{max}+1). \quad (4)$$

Solving Eq. (1) for $\cos(\beta_D-\beta_R)$ and replacing V_D by Eq. (2), it is found that

$$\cos T=\cos(\beta_D-\beta_R)= (V/V_{max})^2(1+K)^2/2K-(1+K^2)/2K = R^2(1+K)^2/2K-(1+K^2)/2K. \quad (5)$$

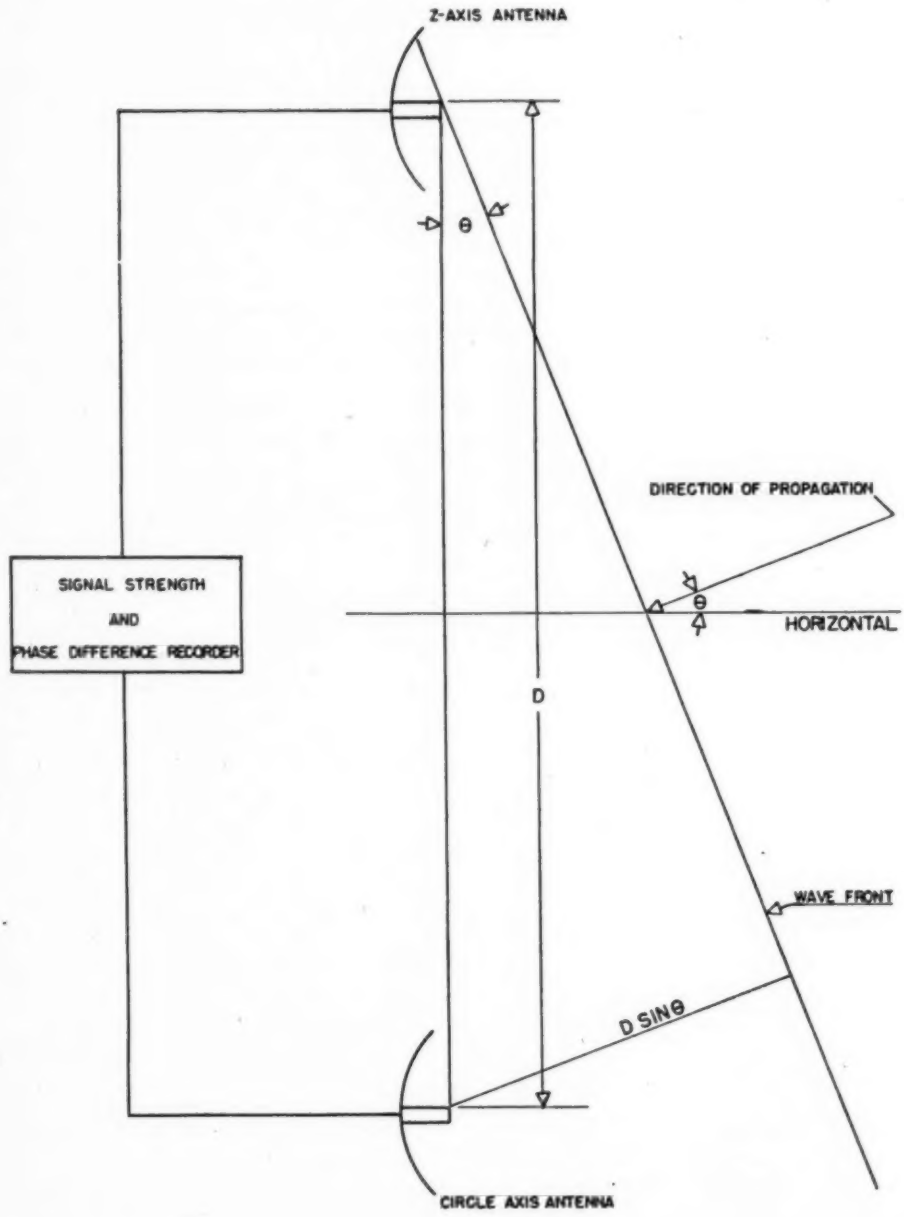

FIG. 13. Principle of measurements.

3. Phase relationships.—The relationship between the phases of the direct, reflected, and combined waves is given by

$$\tan\beta = (\sin\beta_D + K\sin\beta_R)/(\cos\beta_D + K\cos\beta_R). \quad (6)$$

By trigonometric transformation this may be written

$$\tan A = \tan(\beta-\beta_D) = [-K\sin(\beta_D-\beta_R)]/[1+K\cos(\beta_D-\beta_R)] \quad (7)$$
$$= (-K\sin T)/(1+K\cos T).$$

4. Angle of arrival equations.—If only one plane wave were received at the two antennae, as shown in Fig. 13, its angle of arrival could be determined from the phase difference between the two antennae. A wave traveling in a direction making a vertical angle θ with the horizontal, will have a longer path to the lower horn than to the upper horn. This extra distance is given by $D\sin\theta$ and the phase delay at the lower horn is given very closely by

$$\beta_0-\beta_z = 2\pi D\theta/L. \quad (8)$$

For a spacing of 10 feet between antennae and a wave-length of 3.2 cm Eq. (8) becomes

$$\theta = (\beta_0-\beta_z)/600. \quad (9)$$

For the direct and reflected waves this may be written

$$\theta_D = (\beta_{D0}-\beta_{Dz})/600, \quad (10)$$

and

$$\theta_R = (\beta_{R0}-\beta_{Rz})/600. \quad (11)$$

Applying the subscripts z and 0 to the definition of A (Eq. (7)),

$$\beta_0-\beta_{D0} = A_0, \quad (12)$$

$$\beta_z-\beta_{Dz} = A_z. \quad (13)$$

Subtracting (13) from (12) yields

$$(\beta_0-\beta_z)-(\beta_{D0}-\beta_{Dz}) = A_0-A_z.$$

But $\beta_0-\beta_z = d\beta$, and $\beta_{D0}-\beta_{Dz} = 600\theta_D$. From which the angle of arrival of the direct wave is given by

$$\theta_D = (d\beta+A_z-A_0)/600. \quad (14)$$

Similarly, using the definition of T as

$$T = \beta_D-\beta_R,$$

and applying successively the subscripts 0 and z as before, it is found that

$$\beta_{R0}-\beta_{Rz} = \beta_{D0}-\beta_{Dz}-T_0+T_z.$$

But $\beta_{R0}-\beta_{Rz} = 600\theta_R$ and $\beta_{D0}-\beta_{Dz} = 600\theta_D$. The angle of arrival of the reflected ray is then given by

$$\theta_R = \theta_D-(T_z-T_0)/600. \quad (15)$$

5. Sign of A and T.—As the height of the transmitter is raised the distance traveled by the reflected ray in excess of that traveled by the direct ray will increase. If the phase of the direct ray is taken as reference, the phase lag of the reflected ray will be increasing. If phase lag of the reflected wave is less than 180 degrees greater than the "in phase" condition of β_D and β_R, the signal strength will be decreasing with height, β_R will lag β_D and the resultant phase, β, will fall between them. Then $T = \beta_D-\beta_R$ is positive and $A = \beta-\beta_D$ is negative. This means that for any standard interference pattern, T is positive and A negative when the signal strength is decreasing with height. Conversely, T is negative and A is positive when the signal strength is increasing with height.

The Choice of Operating Mode for Standing Wave Type Linear Accelerators for Electrons

ELLIOTT J. LAWTON
General Electric Research Laboratory, Schenectady, New York
(Received December 4, 1947)

Experimental studies of the wave-length spacing between modes of the spectrum of arrays of 10 and 16 cavities with different cavity-to-cavity couplings have been made. The results indicate greatest mode separation near the center, $\pi/2$ mode of the mode spectrum making this mode best for operation. Use of the end π-mode of the spectrum should lead to a limiting length of approximately 3 to 6 ft., while choice of the center $\pi/2$ mode would result in a limiting accelerator length of 10 to 20 ft. at 10.7 cm.

INTRODUCTION

A STANDING wave type of linear accelerator for electrons is usually made up of a series of resonant cavities that form the accelerating gaps. These are mechanically joined together in line so that each is electrically coupled to and will excite its neighbor cavity when fed from an u.h.f. source. The fundamental cavity spacing is $\beta(\lambda_0/2)$ where $\beta=(V/C)$ and λ_0 is the resonance wave-length for the structure, V represents the velocity of the electron for the given gap spacing, and C represents the velocity of light.

The general construction of such an accelerator is shown in Fig. 1 and by the photograph of Fig. 2. Cavities are formed by joining together alternate copper washers and large diameter ring spacers at regular intervals. The number of washers per $\beta(\lambda_0/2)$ interval establishes the desired over-all mode of oscillation for the structure, while the dimensions of washer and spacer determine the value of λ_0 and coupling K between cavities. Termination of the structure is at a current loop.

Operation depends on establishing a standing wave field distribution along the axis of the line of cavities such that a complete phase reversal takes place over each fundamental cavity length. An electron whose velocity matches the phase velocity of this wave will experience an accelerating force at each gap or cavity.

An accelerator made up of an array of n such cavities will have a mode spectrum that has either $n+1$ or n modes, depending on the point of termination. The accelerator design could be based on any one of these modes provided the required number of partitions to establish the mode were included in each $\beta(\lambda_0/2)$ interval along the length, so that a complete phase reversal took place over this fundamental cavity length for the particular mode. The choice of the operating mode must necessarily consider the wave-length distribution of the modes throughout the spectrum, as it is desirable that the separation between operating and adjacent interfering modes be a maximum as the limiting length of the accelerator will be fixed by the onset of interference caused by the crowding of these unwanted modes. The Q of the structure to establish the mode obviously is also a further consideration, both from a power requirement and a mode separation standpoint, since the limiting mode separation need not be as great for a high Q structure as for one of a lower Q.

GENERAL DISCUSSION

The different modes of oscillation of the array of cavities that form the accelerator result from the mutual coupling between individual cavities and groups of cavities. Termination of a given group of cavities restricts the number of modes to those in which the traveling waves on reflection at the termination constructively interfere. A given number of n cavities, therefore, can contain only b half-waves, where b, defined as the mode order, can have integral values from 0 to n. The phase change per cavity is $\pi(b/n)$, and the number of cavities per phase reversal is (n/b). It is assumed here that one individual cavity contains one partition in a symmetrical division. When the division or termination is at the midplane of the cavity proper on either side of the partition, such as is represented by lines

AA in Fig. 3, two modes of oscillation are possible: the $b=0$ order in which the resonant elements on either side of the partition are oscillating in phase or the $b=1$ order in which the two are oscillating π-radians out of phase. The 0 and π-modes represent the lowest and highest order modes that will be found in an array of n such cavities. The phase change per cavity or between cavities of the remaining cavities will have values other than 0 and π, depending on the mutual coupling between cavities or groups of n/b cavities required for one complete phase reversal.

The wave-length of the 0-order mode will have a value approximating that of the "cut-off" value for a cylinder of diameter corresponding to that of the cavity proper. This is the longest wave-length that can be propagated in a cylinder of this diameter, and its value is given by 1.31 D in the case of a straight cylinder. The wave-length of the π-mode will differ from that of the 0 mode because of the effect of the mutual coupling between oscillating elements. The value will be lower than that for the 0-order mode, and the difference between the two will be proportional to the coupling between cavities. A group of n such cavities, therefore, will contain $n+1$ modes of oscillation, all of which are crowded into a wave-length band width proportional to the coupling K, between cavities. If the coupling could be reduced gradually, all $n+1$ wave-lengths would converge towards a value corresponding to that of the 0-order mode or "cut-off" value for the cylinder. If, on the other hand, the coupling were gradually increased, all wave-lengths except the 0-order mode would converge towards that of the π-mode which would have a value equal to zero at 100 percent coupling. In this case there would be no partitions and only the 0-order mode would exist. These two points are illustrated in Fig. 4 for the case of two experimental cavities of AA type termination in which the coupling was varied by changing the diameter of the coupling hole between cavities. The coupling coefficient, K, is the wave-length difference between the 0- and π-order modes expressed as a percentage of the 0-order mode.

When the terminations are shifted to the midplanes through adjacent partitions so that the partition is included at the two ends of the symmetrical division, such as represented by lines BB in Fig. 3, only one mode corresponding to the zero-order, zero-phase change per cavity would exist. A group of n such cavities, therefore, would have only n modes of oscillation, since the highest order π-mode present in the AA type termination would not be permissible.

Assuming a sinusoidal variation of field along the length of an array of in-line cavities, the field distribution for the five modes of an $n=4$ number of cavities of AA type termination would be as shown in Fig. 5. For a given $\beta(\lambda_0/2)$ interval it can be seen that the π-mode would need one partition per phase reversal, while the $\pi/2$ mode would necessarily need $n/b=2$ to establish the mode.

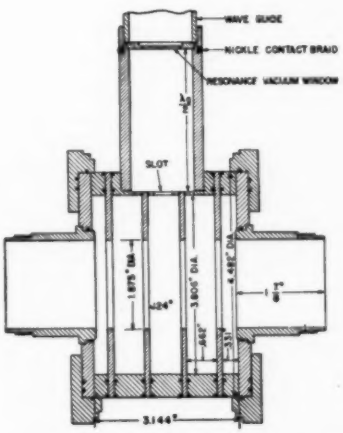

FIG. 1. Two-cavity, cavity-terminated, $\beta=0.75$ accelerator design. $K=17.75$ percent, $\lambda_0=10.705$ cm.

FIG. 2. Two cavity, $\pi/2$ mode design accelerator: $\beta=0.75$, λ_0; 10.701 cm, $K=17.75$ percent.

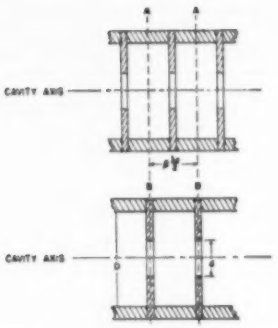

FIG. 3. Schematic cavity arrangement showing the fundamental cavity with AA cavity and BB partition terminations.

EXPERIMENTAL CONSIDERATIONS

The resonance wave-lengths of the various modes were measured at low power with a standard type of equipment such as shown in the block diagram of Fig. 6. In this equipment the frequency-modulated 726 reflex type tunable oscillator furnished excitation for both the wavemeter and the cavity. The modulating voltage for the oscillator also supplied the horizontal sweep for the Du Mont 208 oscilloscope so that horizontal deflection was proportional to frequency over the modulated range. The vertical deflection plates of the scope were connected to the rectified output of the cavity and wavemeter, so that the two resonance peaks appeared on the screen of the scope if the resonance of cavity and wavemeters (W.M.) frequencies fell within the modulated range. Coincidence of W.M. peak with that of the cavity resonance peak afforded a means of determining wavelength. Measurements with this equipment could be reproduced on an average to 1 part in approximately 10,000.

Excitation of a given cavity or group of cavities was with a small antennae extending through and $\frac{1}{8}$-in. axial hole in a conduction plate that terminated the cavity. Likewise, signal pick-up was with a loop extending through a similar hole in the termination plate on the opposite end of the cavity or cavities.

Since extremely high Q was not an important factor in determining the resonant wave-length, soldered joints between cavities were not necessary. This greatly facilitated mode separation studies, as the experiments could be carried out with demountable cavities that could be clamped together and easily changed. An experimental length of any number of n cavities could thus be formed by adding fundamental cavity lengths. The wave-length of the various modes present at each cavity could be measured and the wave-length spacing between modes thus determined.

EXPERIMENTAL RESULTS

The wave-lengths of the mode spectra for varying numbers up to 10 experimental cavities of AA termination are shown in the mode chart of Fig. 7. The dimensions of the experimental cavity are shown in the figure. In the chart the arrows along a given horizontal line point to the particular wave-lengths of the modes of the spectrum corresponding to the number of AA cavities indicated opposite the line along the ordinate. Also is shown the spectra for a few groups of cavities of BB type termination. The wave-lengths in this case are indicated by dots on the chart. It can be seen that the wave-lengths are essentially the same in the two cases and that the π-mode is absent in the BB termination case. The slight differences and slight shift of the pattern with increasing numbers of cavities is due to small known dimensional changes between cavities. The modes of the spectrum for a given n number of cavities will be observed to reappear at multiple intervals of n, indicating the fundamental n/b number necessary to establish the particular modes. For example, the 0 and π-modes for $n=1$ cavities appear at each

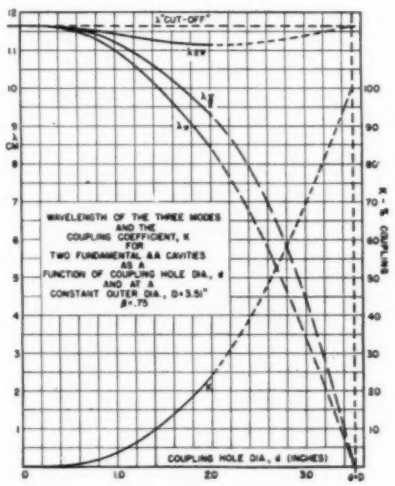

FIG. 4.

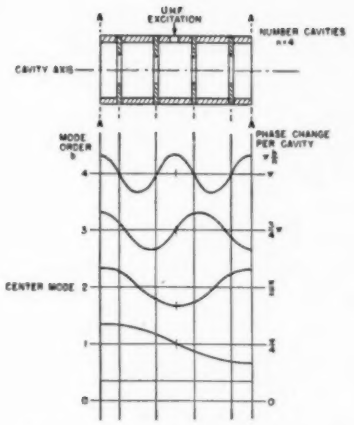

FIG. 5. Axial field distribution for the five modes of four resonant cavities.

cavity addition, indicating one cavity required. The additional $\pi/2$ mode for the $n=2$ cavity spectrum reappears at each multiple of 2 cavities, indicating two cavities necessary to establish this mode. Further, it will be observed that all the modes of the spectrum for a given number of cavities are crowded into the wave-length interval between the 0 and π-modes and that there is less crowding of the modes near the center $\pi/2$ mode than near the two ends, making these best for operation.

Mode separation, $\Delta\lambda$, as a function of the number of cavities for the π and the $\pi/2$ modes of the 10 experimental cavities is shown in Fig. 8. The data indicates that the nearest mode to center $\pi/2$ mode approaches as

$$\Delta\lambda_{\pi/2}=(K/200)\lambda_{2\pi}\sin(\pi/2N_{\pi/2})$$

and for the end π-mode

$$\Delta\lambda_{\pi}=(K/100)\lambda_{2\pi}\sin(\pi/2N_{\pi}^{1.75}).$$

N_{π} and $N_{\pi/2}$ in these expressions are the fundamental structures n/b to establish the modes and the number that must be included in a $\beta(\lambda_0/2)$ interval of accelerator length. For N_{π} this would be one AA division or cavity and for $N_{\pi/2}$ two AA divisions, or twice the number of N_{π} cavities in the same space. K is the coupling coefficient and, as previously defined, is the wave-length difference between the 0 and π-modes expressed as a percentage of the wave-length of the 0-order mode $\lambda_{2\pi}$. $K(\lambda_{2\pi}/100)$, therefore, would represent this difference. In the case of the $\pi/2$ mode, as can be seen from Fig. 7, $K(\lambda_{2\pi}/200)$ represents the maximum difference between $\lambda_{\pi/2}$ and $\lambda\pi$-wave-lengths. Experimentally it has been found that as the coupling is increased $\lambda_{\pi/2}$ shifts slightly towards the $\lambda\pi$-mode, and a value $0.4K(\lambda_{2\pi}/100)$ more nearly fits the experiment for the $\pi/2$ mode over the coupling range of interest (see Fig. 4). $\lambda_{2\pi}$, in terms of the resonance wave-length λ_0 and coupling K, can be expressed as $[\lambda_0/1-(K/100)]$ and $[\lambda_0/1-.6(K/100)]$ for the π and $\pi/2$ modes, respectively. For large values of N_{π} and $N_{\pi/2}$ the two expressions for $\Delta\lambda$ approach,

$$\Delta\lambda_{\pi/2}=0.40(K/100)\lambda_{2\pi}(\pi/2)[1/N_{\pi/2}],$$
$$\Delta\lambda_{\pi}=(K/100)\lambda_{2\pi}(\pi/2)(1/N_{\pi}^{1.75}).$$

Assuming equal Q_s for the two modes, a minimum peak-to-peak mode separation of 0.01 cm at $\lambda_0=10.7$ cm, and $K=9.05$ percent, the maximum number of fundamental cavities in the two cases would be $N_{\pi/2}=60$ and $N_{\pi}=20$. At 10.7 cm there are approximately six cavities per foot length of tube for $\beta=1$, so that the maximum accelerator length in each case would be 10 ft. and 3 ft., respectively, which would also represent the limiting output in Mev at 1 Mev/ft. gradient.

The above assumptions need some justification. The Q_s of the two modes, at a given coupling K, will differ because of the additional partition necessary to establish the $\pi/2$ mode. The difference, however, is slight as the Q of the π-mode design at *equal coupling* was found experimentally to be approximately only 20 percent higher than that for the $\pi/2$ mode design.

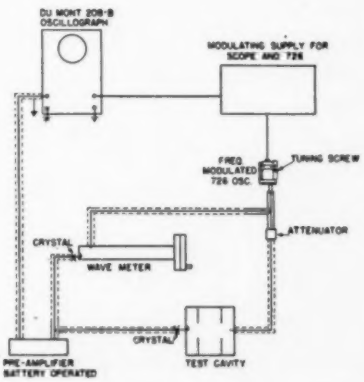

FIG. 6. Schematic arrangement of frequency-modulated wave-length measuring equipment.

The corresponding increase in limiting length of the π-mode design of the accelerator resulting from the sharper resonance would be $1.2^{1/1.75}$ or only 1.1 times at the chosen 0.01-cm minimum peak-to-peak separation.

The assumed minimum $\Delta\lambda = 0.01$ cm was arbitrarily taken as approximately twice the peak-to-peak value for complete separation for an average $Q = 10{,}000$. (A match between accelerator cavity and transmission line is assumed, so that the loaded $Q_L = Q/2 = 5000$.) The Q of the $\pi/2$ and π-mode designs at $K = 9.05$ percent was found to be 9000 and 10,400, respectively.

Choice of coupling coefficient $K = 9.05$ percent necessarily involved the power required to produce the desired axial field of 1 Mev per foot value. At a given value of λ_0 and minimum practical partition thickness (0.125″), an increase in K must be brought about through an increase in coupling hole diameter d, which results in a decrease in axial field at a given power input. The value $K = 9.05$ percent was determined from the results of actual acceleration tests with two 2-cavity tubes of the same length corresponding to a $\beta = 0.75$, but of different coupling resulting from different coupling hole diameters. One of these had a hole diameter 1.366″ and $K = 9.05$ percent, while the other had a $d = 1.875$″ and a $K = 17.75$ percent. The power required to maintain 1 Mev/ft. in the two cases at equal Q's was 0.648 megawatt and 1.22 megawatts/ft., respectively. These values are for the initial $\beta = 0.75$ accelerator cavity lengths and are larger than the expected values for the final $\beta = 1$ design because of the shorter length lower Q cavity. These values extrapolated to the final $\beta = 1$ length indicated 0.270 megawatt per foot for the $K = 9.05$ percent design, and 0.53 megawatt per ft. for the 17.75 percent design. The former power value approaches a practical value for present-day r-f power supplies, such as the HK7 type magnetron while the latter value is too large. Even in the $K = 9.05$ percent case, 1−HK7 magnetron would be needed for approximately each 1.25 ft. of tube at 1 Mev per ft. gradient.

Although the experimental evidence in the case of the group of 10 cavities indicated optimum separation at the $\pi/2$ mode, it was found experimentally that as the coupling was increased the maximum separation shifted towards the lower modes. This is illustrated in Fig. 9 in which wave-length differences between adjacent modes are plotted against mode order b, for the 17 modes of an 8 fundamental $\pi/2$ cavity design accelerator of coupling $K = 17.75$ percent. Similar data for the lower coupling $K = 6$ percent 10-cavity experimental tube is shown in Fig. 10. The mode spectrum for the $\pi/2$ cavity array is also shown. It is also of interest, in the case of the $\pi/2$ mode design, to note the agreement between the experimental values of separation for the π and $\pi/2$ modes and those calculated from the expressions for $\Delta\lambda_\pi$ and $\Delta\lambda_{\pi/2}$, respectively. The maximum separation appears to be at the fourth-order mode instead of the center mode in the higher coupling case, while in the lower coupling case the optimum is at the center mode of the array. To establish this mode, however, $n/b = 4$ partitions per phase reversal or $\beta(\lambda_0/2)$ interval would be needed. This would double the partition loss so that the 30 percent gain in separation as indicated in Fig. 9 over the $\pi/2$ mode would be more than offset by the lower Q.

The maximum number of cavities could be

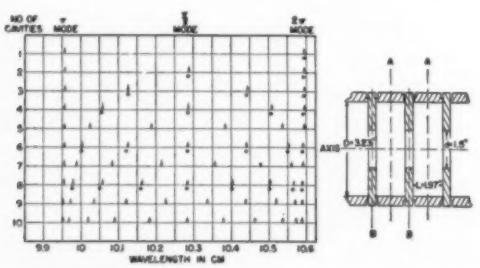

FIG. 7. Mode chart for experimental group of 10 cavities: ↓ cavity termination AA, ● partition termination BB.

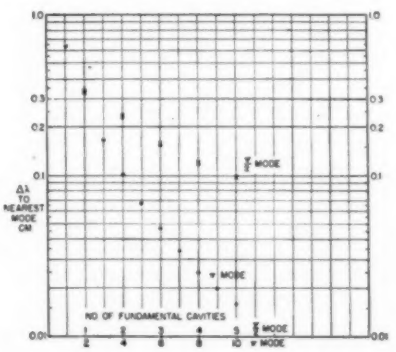

FIG. 8. Mode separation for π and $\pi/2$ modes as a function of the number of fundamental cavities.

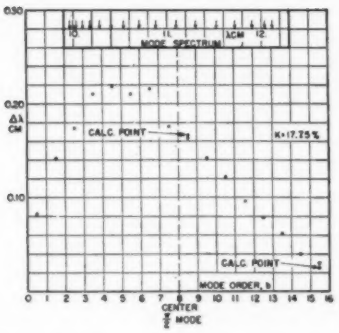

FIG. 9. Wave-length spacing between adjacent modes of the 8 fundamental $\pi/2$ cavity design accelerator as a function of mode order b.

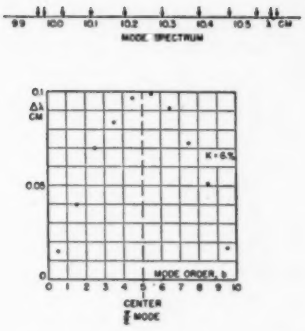

FIG. 10. Wave-length difference between adjacent modes of the group of 10 experimental cavities as a function of mode order b.

approximately doubled by symmetrical excitation at a point along the group of cavities where the field is maximum for the chosen operating mode but zero for the adjacent mode or modes. This is illustrated in Fig. 5, where it can be seen that if power is introduced at the midpoint of the group of 4 cavities, and if either the π or $\pi/2$ mode were the operating mode, excitation of either of these would be possible without exciting the adjacent modes. Unfortunately this condition holds only at the center of a group of even number of cavities, so that the entire power necessarily would have to be fed into this one cavity. There obviously is an upper limit to the maximum number of cavities that could be excited in this manner that would depend on the maximum practical power limit of the guide and maximum number of magnetrons that could be coupled into the one cavity.

Increased mode separation through suppression of undesirable modes and strapping means, while possible, would undoubtedly increase the losses and excitation power.

CONCLUSIONS

The experimental evidence presented would indicate that the center $\pi/2$ mode is the most practical choice of an operating mode for resonant cavity standing wave type of linear accelerators for electrons. At 10.7-cm wave-length and a practical value of coupling a limiting length at which mode interference would predominate is indicated between 10 feet and 20 feet.

ACKNOWLEDGMENTS

The author wishes to acknowledge the many helpful suggestions made by Mr. W. C. Hahn and Dr. L. Tonks. Mr. J. S. Balwit and Mr. Ray Johnston helped in the construction and testing.

Theory of Plastic Flow *versus* Theory of Plastic Deformation*

W. PRAGER
Brown University, Providence, Rhode Island
(Received January 26, 1948)

Typical theories of plastic flow and plastic deformation are discussed, and the concept of neutral change of stress is introduced. A neutral change of stress can be considered as a limiting case of either loading or unloading. It therefore seems reasonable to demand that the stress-strain relations for both loading and unloading should predict the same change of strain when applied to a neutral change of stress. It is shown that this condition is satisfied by the theories of plastic flow but not by the theories of plastic deformation.

1. INTRODUCTION

THE theories of plasticity that have been proposed for metals in the strain hardening range can be divided into two groups: theories of plastic deformation and theories of plastic flow.[1] The theories of the first group are based on the assumption that for continual loading the state of strain is uniquely determined by the state of stress. The theories of the second group, on the other hand, assume that the (infinitesimal) increment of strain is uniquely determined by the existing stress and the increment of stress. Under the special conditions prevailing with the customary arrangements for testing materials under combined stresses the theories of both groups furnish identical predictions, and the available empirical evidence of more general character is too limited to allow a definite decision in favor of one or the other group.[2] Under these circumstances it seems worth while pointing out that for the so-called *neutral* changes of stress (i.e., changes which constitute neither loading nor unloading) the theories of plastic deformation lead to certain difficulties that do not arise with the theories of plastic flow.

2. A TYPICAL THEORY OF PLASTIC DEFORMATION

In order to keep the stress-strain relations mathematically as simple as is possible without loosing essential features of the mechanical behavior, the plastic materials considered in this paper are assumed to be incompressible. Moreover, all viscosity effects are neglected, i.e., the stress-strain relation is assumed to be independent of the speed of deformation. For moderate strain rates and temperatures both assumptions are well justified for structural metals. Finally, the discussion is restricted to *small* deformations. This seems desirable because otherwise we would have to cope, at the same time, with the essential non-linearity of the stress-strain relations in the plastic range and the non-linearity arising from the consideration of finite deformations.

It is useful to represent the stress tensor as the sum of the stress deviation $\mathbf{S}$ and the spherical tensor $-p\mathbf{I}$, where $\mathbf{I}$ denotes the unit tensor and, p the mean pressure, i.e., the negative arithmetic mean of the three principal stresses. If the principal values of the stress deviation are denoted by s_1, s_2, and s_3, we have

$$s_1+s_2+s_3=0. \tag{1}$$

The *octahedral shearing stress* is defined as

$$\tau=[\tfrac{1}{3}(s_1^2+s_2^2+s_3^2)]^{\frac{1}{2}}; \tag{2}$$

it is the shearing stress occurring in planes that have the same orientation with respect to the principal directions of stress as have the faces of an octahedron with respect to its axes. In the mathematical theory of plasticity the octa-

* This paper, which was presented to the 1947 Annual Meeting of the Society of Rheology, was prepared in the course of research conducted under Contract N7onr-358 sponsored jointly by the Office of Naval Research and the Bureau of Ships.

[1] This terminology was introduced by A. A. Ilyushin in his paper "Relation between the theory of Saint Venant-Lévy-Mises and the theory of small elastic-plastic deformations" (Russian with English summary), Priklad. Mat. i Mek. 9, 207 (1946).

[2] See, for instance, K. Hohenemser and W. Prager, "Beitrag zur Mechanik des bildsamen Verhaltens von Flusstahl," Zeits. f. angew. Math. Mech. 12 (1932), available as RTP Translation No. 2468 (Durand Reprinting Committee).

hedral shearing stress is frequently used as a scalar measure for the intensity of stress.

For an *incompressible* elastic material, the generalized Hooke's law has the form

$$2G_0\mathbf{E}=\mathbf{S}, \tag{3}$$

where G_0 denotes the shear modulus and $\mathbf{E}$ the strain tensor. Equation (3) is easily generalized to yield a typical stress-strain relation of the *deformation type:*

$$2G\mathbf{E}=\mathbf{S}, \tag{4}$$

where the *secant shear modulus* G is assumed to be a function of the octahedral shearing stress: $G=G(\tau)$. The stress-strain relation (4) is assumed to hold for the first *loading* from the natural state; for *unloading* it must be replaced by the differential form of Hooke's law:

$$2G_0d\mathbf{E}/dt=d\mathbf{S}/dt, \tag{5}$$

where $d\mathbf{E}/dt$ and $d\mathbf{S}/dt$ denote the rates of change of the strain tensor and of the stress deviation.

To specify the domains of application of (4) and (5), we must establish a criterion for loading and unloading. It seems reasonable to define as *loading* any (infinitesimal) change of stress which leads to an increase of the octahedral shearing stress. Thus, we shall speak of loading or unloading according to whether $\dot{\tau}$ is positive or negative, the dot indicating differentiation with respect to time.

If we set

$$G(\tau)=G_0/[1+g(\tau)], \tag{6}$$

the particular theory of plastic deformation considered above is therefore characterized by the following set of stress-strain relations:

$$\begin{aligned} 2G_0\mathbf{E}&=\mathbf{S}[1+g(\tau)] && \text{for } \dot{\tau}>0,\\ 2G_0d\mathbf{E}/dt&=d\mathbf{S}/dt && \text{for } \dot{\tau}<0. \end{aligned} \tag{7}$$

Stress-strain relations of this type were introduced by A. Nadai;[3] on account of their mathematical simplicity they are widely used in the modern literature.

[3] A. Nadai, *Plasticity, a Mechanics of the Plastic State of Matter* (McGraw-Hill Book Company, Inc., New York, 1931), p. 75. For more general theories of plastic deformation see W. Prager, "Strain-hardening under combined stresses," J. App. Phys. **16**, 837 (1945), and A. Gleyzal, "General stress-strain laws of elasticity and plasticity," J. App. Mech. **13**, A261 (1946), where compressibility is taken into account.

For loading, the total strain $\mathbf{E}$ can be considered as the sum of the *elastic* (or reversible) strain $\mathbf{E}'$ and the *plastic* (or permanent) strain $\mathbf{E}''$. The elastic strain is related to the stress deviation by Hooke's law:

$$2G_0\mathbf{E}'=\mathbf{S}. \tag{8}$$

Substituting this into the first Eq. (7), we find that the plastic strain $\mathbf{E}''=\mathbf{E}-\mathbf{E}'$ is given by

$$2G_0\mathbf{E}''=g(\tau)\mathbf{S}. \tag{9}$$

According to (7), the rate of plastic strain which corresponds to a given rate of stress is therefore found from

$$\begin{aligned} 2G_0d\mathbf{E}''/dt&=g(\tau)d\mathbf{S}/dt+g'(\tau)\dot{\tau}\mathbf{S} && \text{for } \dot{\tau}>0,\\ 2G_0d\mathbf{E}''/dt&=0 && \text{for } \dot{\tau}<0, \end{aligned} \tag{10}$$

where $g'(\tau)$ stands for $dg/d\tau$. We shall refer to (10) as the differential form of the stress-strain relations of the theory of plastic deformation considered here. It should be noted that (10) is homogenous in the time derivatives of $\mathbf{E}''$, $\mathbf{S}$, and τ, and thus not affected by a distortion of the time scale. This means that (10) does not represent any viscosity effects, in spite of the appearance of time derivatives.

3. A TYPICAL THEORY OF PLASTIC FLOW

The stress-strain relation of a theory of plastic flow establishes a relation between the (infinitesimal) increment of strain $d\mathbf{E}$, on one hand, and the existing stress $\mathbf{S}$ and the increment $d\mathbf{S}$, on the other hand. From the formal mathematical point of view, it seems preferable to write this relation in terms of time derivatives rather than differentials. Since viscosity effects are to be disregarded, the stress-strain relation must be homogeneous in these time derivatives.

A typical stress-strain relation of the *flow type* is given by

$$\begin{aligned} 2G_0d\mathbf{E}/dt&=d\mathbf{S}/dt+h(\tau)\dot{\tau}\mathbf{S} && \text{for } \dot{\tau}>0,\\ 2G_0d\mathbf{E}/dt&=d\mathbf{S}/dt && \text{for } \dot{\tau}<0, \end{aligned} \tag{11}$$

where $h(\tau)$ is a suitable function of the octahedral shearing stress. If this stress-strain relation is adopted, the rate of plastic strain is found to be

$$\begin{aligned} 2G_0d\mathbf{E}''/dt&=h(\tau)\dot{\tau}\mathbf{S} && \text{for } \dot{\tau}>0,\\ 2G_0d\mathbf{E}''/dt&=0 && \text{for } \dot{\tau}<0. \end{aligned} \tag{12}$$

Stress-strain relations of this type, with a particular choice of $h(\tau)$, were first used by W. Prager.[4] The general form (11) was suggested by H. J. Laning in 1942 in an unpublished manuscript; further stress-strain relations of the flow type have been discussed by G. H. Handelman, C. C. Lin, and W. Prager.[5]

In spite of the superficial similarity of the first Eqs. (10) and (12), there is this important difference: whereas the first Eq. (10) can be integrated with respect to time to yield the first Eq. (7), the first Eq. (12) is not so integrable. Thus, if a certain state of stress **S** is reached by a continuous loading process starting from the natural state, Eq. (10) predicts a corresponding state of strain which is independent of the precise manner in which the stress **S** is reached. According to Eq. (12), on the other hand, the state of strain will depend on the manner in which the **S** is reached from the natural state.

4. SIMPLE LOADING

Following A. A. Ilyushin,[6] we shall speak of *simple loading* when all stress components increase proportionally with time (or with the same monotonically increasing function of time) during the entire loading process. It is easy to show that the theories of plastic deformation and of plastic flow can be made to agree under these circumstances. Indeed, from

$$\mathbf{S}=\mathbf{S}^*t, \tag{13}$$

where the symmetric tensor $\mathbf{S}^*$ is independent of t, it follows that

$$\tau=\tau^*t, \tag{14}$$

where τ^* is independent of t and is related to the principal components of $\mathbf{S}^*$ in the same manner as is τ to the principal components of **S**. Substituting (13) and (14) into the first Eq. (12) and integrating with respect to t, we obtain

$$2G_0\mathbf{E}''=H(\tau)\mathbf{S}, \tag{15}$$

where

$$H(\tau)=(1/\tau)\int_0^\tau \tau h(\tau)d\tau. \tag{16}$$

Equations (9) and (15) coincide when $g(\tau)=H(\tau)$. With a suitable choice of the functions $g(\tau)$ and $h(\tau)$ the theories of plastic deformation and flow discussed here will therefore furnish identical predictions in the case of simple loading.

It is unfortunate that almost all experiments concerning the plastic behavior of metals in the strain-hardening range have been conducted under the conditions of simple loading and are, therefore, without value as far as a decision between the theories of plastic deformation and flow is concerned.[7] Pointing out this fact, A. A. Ilyushin[6] recently argued that as long as there was no definite experimental evidence in favor of the flow theory, the mathematically much simpler deformation theory seemed preferable. This argument, however, overlooks an important difficulty which is encountered in the application of the deformation theory to neutral changes of stress.

5. NEUTRAL CHANGE OF STRESS

In simple tension any change of stress constitutes either loading or unloading. For more general states of stress, however, this is no longer true and a change of stress may constitute loading, or unloading, or neither loading nor unloading. Indeed, if the change of the octahedral shearing stress is adopted as a criterion for loading or unloading, we must consider the following three cases: (1) $\dot{\tau}>0$ (loading), (2) $\dot{\tau}<0$ (unloading), (3) $\dot{\tau}=0$ (neutral change of stress). A neutral change of stress occurs, for instance, when the stress components are varied in such a manner that the principal stresses preserve their values while the principal directions rotate with respect to the material.

[4] W. Prager, "On isotropic materials with continuous transition from elastic to plastic state," Proc. Int. Cong. App. Mech. 1938, pp. 234–237; "A new mathematical theory of plasticity," Rev. Fac. Sci. Istanbul (**A**)**5**, 215 (1941); "Fundamental theorems of a new mathematical theory of plasticity," Duke Math. J. **9**, 228 (1942).

[5] G. H. Handelman, C. C. Lin, and W. Prager, "On the mechanical behavior of metals in the strain-hardening range," Quart. App. Math. **4**, 397 (1947).

[6] A. A. Ilyushin, "On the theory of plasticity in the case of simple loading of plastic bodies with strain-hardening" (Russian with English summary), Priklad. Mat. i Mek. **11**, 293 (1947). The importance of the type of plastic deformation which corresponds to simple loading had already been recognized by K. Hohenemser and W. Prager who used the term "free deformation" (reference 3, p. 5).

[7] Experiments upon which such a decision could be based have recently been outlined by D. C. Drucker, "Stress-strain relations for strain-hardening materials—Discussion and proposed experiments," to be published in Proc. Ann. Sympos. App. Math., 1947.

A neutral change of stress can be considered as a limiting case of either loading or unloading. It therefore seems reasonable to demand that the stress-strain relations for both loading and unloading should predict the same change in strain when applied to a neutral state of stress. The stress-strain relations of the theory of plastic flow fulfill this condition. Indeed, with $\dot{\tau}=0$ (neutral change of stress), the first and second Eqs. (12) coincide. The stress-strain relations of the theory of plastic deformation, on the other hand, do not satisfy this condition. For $\dot{\tau}=0$, the first Eq. (10) gives

$$2G_0 d\mathbf{E}''/dt = g(\tau) d\mathbf{S}/dt, \tag{17}$$

while the second Eq. (8) is

$$2G_0 d\mathbf{E}''/dt = 0. \tag{18}$$

Equations (17) and (18) coincide only if $g(\tau)=0$, which is obviously absurd. Thus, the stress-strain relations of the deformation theory predict different changes of strain for the same neutral change of stress according to whether this change of stress is considered as a limiting case of loading or unloading. If the surface tractions on a body made of a plastic material with the stress-strain relations (10) were varied so that part of the body was being loaded and the remainder unloaded, the rates of stress would not be continuous across the surface separating the region of loading from that of unloading. Quite independent of future empirical evidence concerning the two theories, this fact casts severe doubts on the validity of the theory of plastic deformation.

Calendar of Meetings

June

14–18 American Association of Physics Teachers and American Society for Engineering Education, Austin, Texas
14–19 Symposium on Molecular Structure and Spectroscopy, Columbus, Ohio
17 American Mathematical Society, University of British Columbia, Vancouver, British Columbia
21–23 American Physical Society, Madison, Wisconsin
21–25 American Institute of Electrical Engineers (Summer General Meeting), Mexico City, Mexico
21–25 American Society for Testing Materials (Annual Meeting), Detroit, Michigan
21–September 3 Gordon Research Conferences (formerly Gibson Island Research Conferences), American Association for the Advancement of Science, New London, New Hampshire
23–25 National Colloid Symposium, Cambridge, Massachusetts
24–26 American Physical Society, Pasadena, California
28–July 1 American Astronomical Society, Pasadena, California
28–July 16 Northwest Conference on Nuclear Science, Reed College, Portland, Oregon

July

8–11 General Assembly, International Union of Pure and Applied Physics, Amsterdam, Holland
12–18 Conference on the Physics of Metals, under auspices of Netherlands Physical Society and Netherlands Committee of the International Union of Pure and Applied Physics, Amsterdam, Holland
12–18 International Commission of Optics, Schveningen (The Hague), Netherlands
21–23 American Society of Civil Engineers, Seattle, Washington
28–August 3 International Union of Crystallography, Cambridge, Massachusetts
29–31 Second Symposium on Applied Mathematics, American Mathematical Society with the cosponsorship of the American Institute of Physics, Cambridge, Massachusetts

August

2–6 Instrumentation Conference (Gordon Research Conferences), New London, New Hampshire
10 International Astronomical Union, Zurich, Switzerland
18–20 Society of Automotive Engineers (West Coast Meeting), San Francisco, California
19–28 International Union of Geophysics, Oslo, Norway
24–27 American Institute of Electrical Engineers (Pacific General Meeting), Spokane, Washington
24–September 1 18th International Geological Congress, London, England
30–September 4 American Chemical Society (Eastern Session), Washington, D. C.

The Theory of Extreme Values and Its Implications in the Study of the Dielectric Strength of Paper Capacitors

BENJAMIN EPSTEIN
Coal Research Laboratory, Carnegie Institute of Technology, Pittsburgh, Pennsylvania

AND

HAMILTON BROOKS
Protective Devices Engineering Department, Westinghouse Electric Corporation, East Pittsburgh, Pennsylvania

(Received December 23, 1947)

In this paper it is shown that the statistical theory of the distribution of extreme values is pertinent to the study of the way in which the breakdown strengths of paper capacitors depend on capacitor size. The theory presented in this paper permits a quantitative explanation of this phenomenon and results are given which should be useful to design engineers.

1. INTRODUCTION

IN a recent paper[1] one of the authors pointed out that the statistical theory of the distribution of extreme values is relevant to the study of the dependence of the strength of specimens on their size. The term strength is meant to be quite general in scope: we may have in mind mechanical strength, electrical strength, ability to stop the passage of light rays or to prevent the diffusion of a gas, resistance of painted specimens to the corrosive effects of the atmosphere, or perhaps the life span (or the intervals between repairs) of a device which ceases to function when any one of a number of vital parts breaks down. From a statistical point of view, problems of this sort are all essentially equivalent if we conceive of materials as being permeated by small defects spread in a random way throughout the body. These defects give rise to local weaknesses which may reduce the strength of a specimen locally to a value which is considerably smaller than the theoretical strength of the specimen. Assuming now that the randomly distributed flaws have a certain density per unit volume (or unit area or unit length), the statistical formulation of the problem becomes evident. If the flaw concept is accepted, then the strength of a given specimen is determined by the weakest point in the specimen or the smallest value to be found in a sample of size n, where n is the number of flaws. Clearly, n increases as the size of the specimen increases, and, therefore, the problem of finding how the strength depends on the size of the specimen is equivalent statistically to the study of the distribution of the smallest value as a function of n, the sample size. This is a statistical problem on which much work has been done.

It should be mentioned in passing that the flaw concept was first introduced by A. A. Griffith[2] in his investigations on the rupture of solids. As far as is known to the present authors, F. T. Peirce[3] of the British Cotton Industry Research Association was the first to realize the close connection between the strength of a specimen and the distribution of smallest values. His insight into the problem is summed up in the statement: "It is a truism, of which the mathematical implications are of no little interest, that the strength of a specimen is that of its weakest link."

2. APPLICABILITY OF THE FLAW CONCEPT TO THE STUDY OF THE BREAKDOWN STRENGTH OF PAPER CAPACITORS

Turning to the subject of this paper, it is evident that the flaw concept must play a basic role in determining the distribution of breakdown strength of paper capacitors. It is an undisputed fact that no matter how carefully capacitor paper is manufactured, or how carefully capacitors are manufactured, defects of various kinds (such as conducting particles) are present in the finished product. The defects de-

[1] B. Epstein, "Statistical aspects of fracture problems," J. App. Phys. **19**, 140 (1948).

[2] A. A. Griffith, Phil. Trans. Roy. Soc. **221A**, 163 (1920); Proc. Int. Cong. App. Mech. **1**, 55 (1924).

[3] F. T. Peirce, J. Textile Inst. **17**, 355 (1926).

pending on their size and orientation create a local weakening of the capacitor by reducing the nominal paper thickness of the capacitor. This means that the breakdown strength of a given capacitor is equal to its strength at its weakest point (the place where the largest effective penetration of the paper has occurred). It is clear that if we restrict ourselves to some class of capacitors all made with the same number of layers of paper of a given thickness, then the most probable value of the breakdown voltage of capacitors of increasing microfarad rating, and hence greater paper area, must decrease. It will be shown how such a phenomenon can be quantitatively studied through the use of the statistical theory of the distribution of extreme values in random samples of size n drawn from a population having some probability density function $f(x)$. This theory will predict that under certain assumptions about the distribution of effective defect sizes, the most probable value of the breakdown voltage $V^*(A)$ corresponding to capacitors of area A, is related to A by a relationship of the form

$$V^*(A) = \alpha - \beta \log A,$$

where α and β are positive constants determined by the density of conducting particles per unit area and by the size distribution of these particles. This result includes the one observed experimentally by one of the authors[4] of this paper for capacitors ranging in size from 0.01 microfarad to 100 microfarads, all capacitors being made with three layers of 0.5-mil thick oil impregnated paper.

3. THE STATISTICAL THEORY OF THE DISTRIBUTION OF EXTREME VALUES

Since the dielectric strength of a capacitor in the immediate neighborhood of a conducting particle is determined by the size of the particle, it is immaterial from a statistical point of view whether one considers, on the one hand, the distribution of dielectric strengths in the neighborhood of flaws, or on the other, the distribution of the sizes of conducting particles. In this paper it will prove convenient to study the distribution of dielectric strengths of capacitors by considering the distribution of the largest values in samples of size n drawn from a population of conducting particles following some size distribution law described by a continuous probability density function $f(x)$.

The statistical theory of the distribution of extreme values of samples of size n, drawn from a population possessing the probability density function $f(x)$, is interesting and important in its own right. Limitations of space, however, do not justify a detailed description of the theory. An excellent account of the basic theory as it exists at the present time will be found in a recent book by H. Cramér.[5] The basic work on the asymptotic theory, i.e., the distribution of the extreme values for large samples ($n \to \infty$) was done by R. A. Fisher and Tippett,[6] and Gumbel.[7] The latter author has also applied the theory to the study of floods,[8] the distribution of ages in mortality tables,[9] and to other physical phenomena.

It is sufficient for the purposes of this paper to write down a few basic formulae concerning the distribution of largest values in samples of size n drawn from a distribution described by a continuous probability density function $f(x)$,

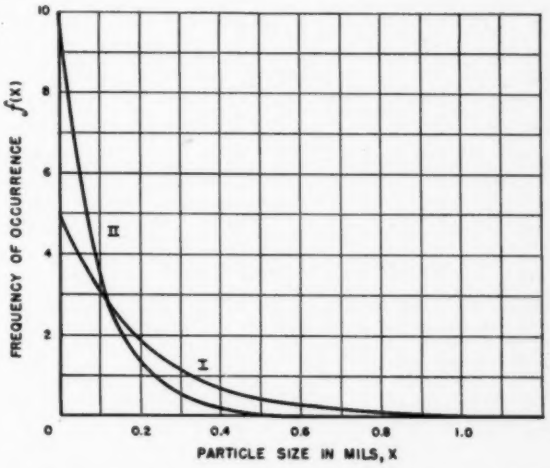

FIG. 1. Distribution of particle size, $f(x) = \lambda e^{-\lambda x}$. (I) $\lambda = 5$, (II) $\lambda = 10$.

[4] H. Brooks, A.I.E.E. Tech. Pap., 47–164 (1947).

[5] H. Cramér, *Mathematical Methods of Statistics* (Princeton University Press, Princeton, New Jersey, 1946).

[6] R. A. Fisher and L. H. C. Tippett, Proc. Camb. Phil. Soc. **24**, 180 (1928).

[7] E. J. Gumbel, Ann. Inst. Henri Poincaré **5**, 115 (1936).

[8] E. J. Gumbel, Ann. of Math. Stat. **12**, 163 (1941).

[9] E. J. Gumbel, *La Durée Extrême de la Vie Humaine* (Actualités Scientifiques et Industrielles, Hermann et Cie, Paris, 1937).

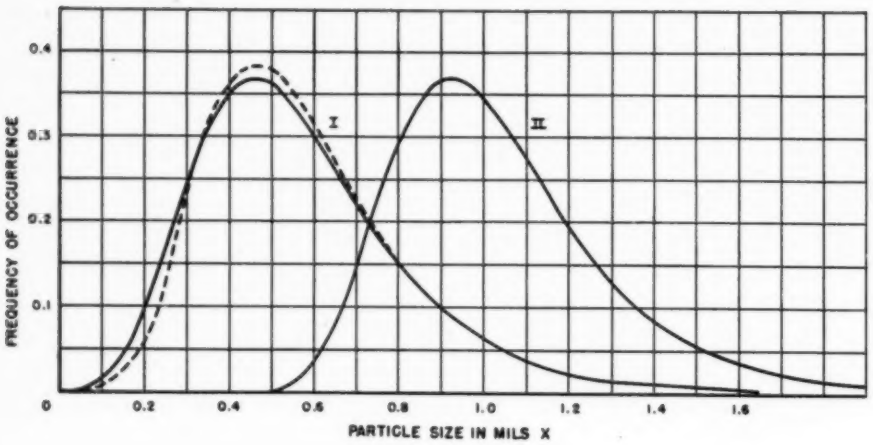

FIG. 2. Distribution of largest conducting particle taken from size distribution $f(x) = 5e^{-5x}$. (I) sample size $n_1 = 10$. (II) sample size $n_2 = 100$. Exact distribution - - -. Approximate distribution——.

subject to trivial analytic restrictions. If the cumulative function associated with $f(x)$ is

$$F(x) = \int_{-\infty}^{x} f(x)dx,$$

then the distribution of the largest values in sample size n drawn from the population is given by the probability density function

$$g_n(x) = nf(x)(F(x))^{n-1}, \tag{1}$$

or by the cumulative distribution function

$$G_n(x) = \int_{-\infty}^{x} g_n(x)dx = (F(x))^n. \tag{2}$$

Using (1) and (2) one can already draw graphs of $g_n(x)$ and $G_n(x)$ for any given $f(x)$. The *mode* of $g_n(x)$ (i.e., the *most probable value* of the largest value in samples of size n drawn from a population with probability density function $f(x)$) is found by equating $g_n'(x)$ to zero. If a solution x_n^* exists, then

$$f^2(x_n^*)(n-1) = -f'(x_n^*)F(x_n^*). \tag{3}$$

If the initial distribution is limited, the distribution of the largest value increases monotonically and no mode in the proper sense exists.

Equations (1), (2), and (3) are adequate if one is merely interested in giving a crude description of the distribution of the largest value in samples of size n drawn from a parent population $f(x)$. It is necessary to go further, however, if one wishes to study the distribution of largest values quantitatively, particularly for large values of n.

In order to study the distribution of largest values, it is convenient to introduce a new random variable ξ, which is defined as

$$\xi = n(1 - F(x)). \tag{4}$$

In terms of this variable, (1) becomes

$$h_n(\xi) = (1 - \xi/n)^{n-1}. \tag{5}$$

The probability density function $h(\xi)$ as $n \to \infty$ is

$$h(\xi) = \lim_{n\to\infty} h_n(\xi) = e^{-\xi}, \quad \xi > 0. \tag{6}$$

Using Eqs. (4) and (6) one can now completely specify the distribution of x, the largest value in samples of size n for large values of n.

4. APPLICATION OF THEORY TO BREAKDOWN STRENGTH OF CAPACITORS

Data on the size distribution of conducting particles have been analyzed by one of the authors[4] of this paper, and it appears that a reasonable approximation to the true state of affairs is to assume that the size distribution of conducting particles, $f(x)$, is of exponential type

$$f(x) = \lambda e^{-\lambda x}, \quad x > 0. \tag{7}$$

In Fig. 1 the probability density function is shown for $\lambda = 5$ and $\lambda = 10$.

It is interesting to see what happens if one studies the distribution of largest values in samples of size n drawn from parent population of the form (7). In this case,

$$F(x) = \int_0^x f(x)dx = \int_0^x \lambda e^{-\lambda x}dx = 1 - e^{-\lambda x}.$$

The distribution, $g_n(x)$, of largest values in samples of size n is given by

$$g_n(x) = nf(x)(F(x))^{n-1}$$
$$= n\lambda e^{-\lambda x}(1-e^{-\lambda x})^{n-1}, \quad x>0, \quad (8)$$

and the cumulative distribution function $G_n(x)$ by

$$G_n(x) = (F(x))^n = (1-e^{-\lambda x})^n, \quad x>0. \quad (9)$$

The most probable value of the largest value in samples of size n, x_n^*, is the solution of

$$\begin{aligned} f^2(x_n^*)(n-1) &= -f'(x_n^*)F(x_n^*), \\ \lambda^2 e^{-2\lambda x_n^*}(n-1) &= \lambda^2 e^{-\lambda x_n^*}(1-e^{-\lambda x_n^*}), \\ ne^{-\lambda x_n^*} &= 1, \\ x_n^* &= \log n/\lambda. \end{aligned} \quad (10)$$

This result is important since it states that the mode of the distribution of the largest value in samples of size n drawn from $f(x)=\lambda e^{-\lambda x}$ increases as the logarithm of n.

To get an approximation to the distribution of largest values in samples of size n for large n, we introduce ξ, where

$$\xi = n(1-F(x)) = ne^{-\lambda x}. \quad (11)$$

Taking the logarithm of both sides of (11) it follows that the distribution of x for large n is approximately given by

$$x = \log n/\lambda - \log \xi/\lambda, \quad (12)$$

where ξ is distributed with the probability density function

$$h(\xi) = e^{-\xi}, \quad \xi>0.$$

Letting $\eta = \log \xi$, the approximate distribution of x becomes

$$x = \log n/\lambda - \eta/\lambda, \quad (13)$$

where η is distributed as $e^{\eta}e^{-e^{\eta}}$, $-\infty<\eta<\infty$. The exact distribution of x, the largest value in sample of size n, is given by (8), and it is interesting to see how this exact distribution differs from the approximate formula in (13). In Fig. 2 are given both the exact and approximate distributions of x, the size of the largest conducting particle drawn from a population of exponential type with $\lambda=5$ and with sample sizes $n_1=10$ and $n_2=100$.

It is easy to go from the consideration of the distribution of the size of the largest conducting particle in samples of size n to the distribution of breakdown voltages of capacitors. Assume that the capacitors under consideration belong to a definite classification, all made with the same number of sheets of paper of a certain thickness and differing only in their total surface. Let V_0 be the theoretical breakdown strength of the given thickness of oil impregnated paper when free of any defects, let δ be the density (number per square inch) of all conducting particles of any size in a square inch of paper, let γ be the breakdown voltage per mil of impregnated paper, and let λ as before be the constant in the exponential size distribution (7), then the direct application of (10) yields the result that the most probable value of the breakdown voltage of capacitors of total surface area A is given by

$$V^*(A) = V_0 - \gamma \log(A\delta)/\lambda, \quad (14)$$

where $A\delta$ is the expected number of defects in capacitors of area A. It also follows that if $A'=10A$, then

$$V^*(A) - V^*(A') = \gamma \log 10/\lambda = 2.303\gamma/\lambda. \quad (15)$$

In other words, the effect of increasing the total area of a capacitor by a factor of 10 will reduce the most probable value of the breakdown voltage by the amount on the right-hand side of (15). In actual practice γ is not strictly a con-

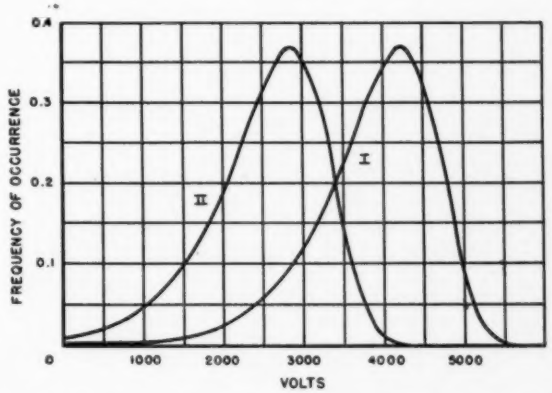

FIG. 3. Distribution of breakdown voltages in capacitors under the following assumptions: Frequency distribution of size of conducting particles $=5e^{-5x}$. Number of conducting particles per square inch $=1$. Dielectric strength of impregnated paper (volts per mil) $=3000$. Breakdown voltage of impregnated paper with no defects $=7000$. Area of paper in capacitors (square inches). Case I $=100$. Case II $=1000$.

TABLE I. Breakdown voltages of 250 capacitor samples made with two sheets of oil impregnated 0.4-mil paper.

No.	Volts	No.	Volts	No.	Volts	No.	Volts	No.	Volts
1	1500	51	1620	101	1620	151	1740	201	1740
2	1740	52	1620	102	1740	152	1620	202	1440
3	1500	53	1620	103	1800	153	1740	203	1560
4	1440	54	1380	104	1740	154	1740	204	1500
5	1620	55	1740	105	1680	155	1740	205	1680
6	1620	56	1500	106	1500	156	1500	206	1740
7	1860	57	1740	107	1680	157	1740	207	1740
8	1740	58	1560	108	1740	158	1740	208	1740
9	1560	59	1620	109	1680	159	1800	209	1500
10	1560	60	1440	110	1740	160	1740	210	1680
11	1680	61	1740	111	1620	161	1740	211	1440
12	1620	62	1620	112	1800	162	1800	212	1740
13	1620	63	1680	113	1680	163	1680	213	1680
14	1680	64	1800	114	1440	164	1860	214	1620
15	1440	65	1740	115	1800	165	1680	215	1500
16	1560	66	1440	116	1680	166	1740	216	1800
17	1620	67	1620	117	1740	167	1740	217	1560
18	1620	68	1680	118	1740	168	1800	218	1740
19	1620	69	1620	119	1800	169	1800	219	1440
20	1740	70	1680	120	1680	170	1740	220	1560
21	1680	71	1680	121	1740	171	1620	221	1740
22	1620	72	1680	122	1500	172	1740	222	1500
23	1620	73	1740	123	1560	173	1740	223	1680
24	1680	74	1680	124	1740	174	1800	224	1740
25	1620	75	1620	125	1620	175	1740	225	1800
26	1740	76	1620	126	1500	176	1620	226	1620
27	1620	77	1740	127	1560	177	1680	227	1680
28	1740	78	1560	128	1380	178	1560	228	1500
29	1680	79	1680	129	1620	179	1800	229	1800
30	1620	80	1380	130	1800	180	1380	230	1560
31	1740	81	1740	131	1740	181	1320	231	1740
32	1740	82	1740	132	1740	182	1680	232	1800
33	1740	83	1680	133	1620	183	1740	233	1440
34	1080	84	1620	134	1740	184	1740	234	1380
35	1680	85	1620	135	1740	185	1800	235	1500
36	1800	86	1800	136	1740	186	1800	236	1620
37	1620	87	1740	137	1680	187	1200	237	1440
38	1740	88	1620	138	1800	188	1740	238	1740
39	1620	89	1740	139	1740	189	1800	239	900
40	1740	90	1740	140	1680	190	1500	240	1740
41	1680	91	1620	141	1500	191	1740	241	1800
42	1800	92	1680	142	1740	192	1680	242	1800
43	1560	93	1560	143	1680	193	1680	243	1680
44	1860	94	1560	144	1740	194	1620	244	1740
45	1800	95	1740	145	1680	195	1500	245	1800
46	1620	96	1500	146	1260	196	1560	246	1740
47	1800	97	1800	147	1560	197	1680	247	1560
48	1740	98	1740	148	1800	198	1620	248	1620
49	1620	99	1620	149	1680	199	1620	249	1740
50	1800	100	1680	150	1740	200	1440	250	1800
			Average				1656		
			Standard Deviation				130		

Frequency distribution of data in Table I.

Voltage interval	Number of observations in interval
801– 900	1
901–1000	0
1001–1100	1
1101–1200	1
1201–1300	1
1301–1400	6
1401–1500	28
1501–1600	18
1601–1700	86
1701–1800	105
1801–1900	3
	250 total

stant but is a function of thickness and this will require an additional correction which is easily made from known empirical formulae connecting breakdown voltage and insulation thickness.

Substitution in Eq. (13) gives the approximate distribution of the breakdown voltage in capacitors of area A, and this is

$$V(A) = V^*(A) + \gamma\eta/\lambda, \tag{16}$$

where η is distributed as $e^{\eta}e^{-e^{\eta}}$, $-\infty < \eta < \infty$. The exact distribution of $V(A)$ is given by

$$V(A) = V_0 - \gamma x, \tag{17}$$

where x is a random variable whose probability density function is given by

$$g_A(x) = A\delta\lambda e^{-A\delta\lambda x}(1-e^{-\lambda x})^{A\delta-1}, \quad x>0. \tag{18}$$

In Fig. 3 is given the approximate distribution of $V(A)$, the breakdown voltage in capacitors of area A, where $\delta=1$, $\gamma=3000$ volts per mil, $\lambda=5$, $A_1=100$ sq. in., $A_2=1000$ sq. in., and with $V_0=7000$ volts. The exact distribution is so close to the approximate distribution that it is sufficient to give only the latter.

5. THE THEORY OF EXTREME VALUES AS AN AID TO THE DESIGN ENGINEER

It should be pointed out that formulae (14), (15), and (16) can be useful to a design engineer. The unknown constants in these equations are V_0, γ, δ, and λ. Focusing attention only on δ and λ, the two parameters associated with the distribution of conducting particles, one can make the following statements:

(a) If λ is held constant and δ, the number of conducting particles per square inch is decreased (increased), then the most probable value of the breakdown voltage for capacitors of area A will be larger (smaller). However, the difference between the most probable value of the breakdown voltage for capacitors of area A and A', respectively, will remain the same since this

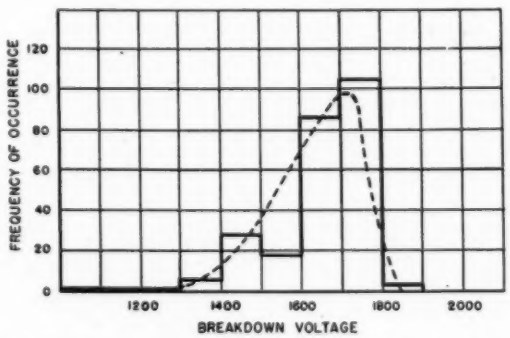

FIG. 4. Frequency histogram of breakdown voltages of 250 capacitors made with two sheets of 0.4-mil paper and 33.75 square inch area.

difference depends only on λ according to (15). The distributions in (16) will all be shifted by a constant amount in the direction of increasing voltage if δ is decreased and in the direction of decreasing voltage if δ is increased, holding λ fixed.

(b) If δ is held constant and λ is increased (decreased), then the most probable value of the breakdown voltage of capacitors of area A will be larger (smaller). The difference between the most probable value of breakdown voltage for capacitors of areas A and A', respectively, will be smaller (larger) according as λ is increased (decreased). The distribution in (16) will be shifted in the direction of increasing voltage (in the direction of decreasing voltage) and the spread will become narrower (broader) as λ is increased (decreased).

Changes in both γ and λ can be similarly studied. Statements (a) and (b) can be made precise by putting numerical values into (14), (15), and (16).

6. A NUMERICAL EXAMPLE

To illustrate the theory consider the data in Table I. These data give the breakdown voltage of 250 samples, each sample consisting of two layers of 0.4-mil kraft paper which had been oil impregnated. The electrode area was 16.875 sq. in. and the total area for the two sheets was 33.75 sq. in. To see the effect of increasing capacitor size on the breakdown voltage, one can use a simple device. The data, taken in order, are split into twenty-five groups, each containing a sample of ten successive observations. The smallest value of the breakdown voltage in each group of ten can be taken as the breakdown voltage of a capacitor whose area is ten times as large as any of its component parts. The twenty-five breakdown voltages obtained in this way constitute a random sample from a population of capacitors each having an area of 337.5 sq. in. The twenty-five values are given in Table II, and in Figs. 4 and 5 are given frequency distributions for the original sample of 250 and the derived sample of 25. The observed frequency distributions of breakdown voltage and their dependence on area are in substantial agreement with the statistical theory presented in this paper.

The design engineer is in a position to make some predictions about the effect of increasing capacitor sizes from a series of tests like that

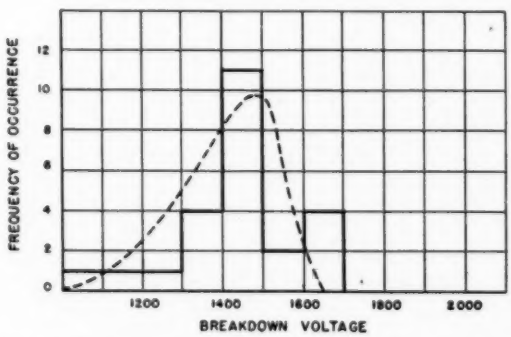

FIG. 5. Frequency histogram of breakdown voltages of 25 capacitors made with two sheets of 0.4-mil paper and 337.5 square inch area.

TABLE II. Breakdown voltages of 25 capacitors each composed of 10 successive capacitor samples taken from Table I.

No.	Volts
1	1440
2	1440
3	1620
4	1080
5	1560
6	1380
7	1440
8	1380
9	1620
10	1500
11	1500
12	1440
13	1380
14	1620
15	1260
16	1500
17	1680
18	1380
19	1200
20	1440
21	1440
22	1440
23	1500
24	900
25	1560
Average	1428.0
Standard deviation	169.7

Frequency distribution of data in Table II.

Voltage interval	Number of observations in interval
801– 900	1
901–1000	0
1001–1100	1
1101–1200	1
1201–1300	1
1301–1400	4
1401–1500	11
1501–1600	2
1601–1700	4
	25 total

given in Table I. According to Eq. (16) the distribution of breakdown voltages of capacitors of area A is given by:

$$V(A) = V^*(A) + \gamma\eta/\lambda.$$

The only unknowns are $V^*(A)$ and the ratio γ/λ. (Of course, if we assign a definite value to γ such as 3000 volts per mil, then λ is the second unknown.) These may be determined by finding the mean and the standard deviation of $V(A)$. These values are 1656 and 130, respectively. Since the mean and standard deviation of the random variable η are -0.577 and $\pi/(6)^{\frac{1}{2}}$, respectively,* it follows that

$$V^*(A) - 0.577\gamma/\lambda = 1656,$$
$$(\pi/6^{\frac{1}{2}})\gamma/\lambda = 130.$$

This gives $\gamma/\lambda = 101$ and $V^*(A) = 1715$. According to Eq. (15) the effect of increasing the capacitor area to $A' = 10A$ leads to a shift in the distribution of breakdown voltage in the direction of decreasing voltage by an amount $2.303\gamma/\lambda$. In this case the decrease is 232 volts. The observed difference is 228 volts = 1656 (the average of the breakdown voltages of 250 capacitors in Table I) minus 1428 (the average of the breakdown voltages of 25 capacitors in Table II). There is certainly good agreement between theory and observation in this case. It is clear that the design engineer has a useful tool for determining quantitatively the effect of increasing capacitor size and can, if he wishes, predict such things as the percentage of capacitors of any given size that would fail to survive some specified voltage.

* The mean value of η is $E(\eta) = \int_{-\infty}^{\infty} \eta e^{\eta} e^{-e^{\eta}} d\eta$
$= \int_0^{\infty} \log t e^{-t} dt = -0.577.$
The variance of η is $E(\eta^2) - (E(\eta))^2$
$= \int_0^{\infty} (\log t)^2 e^{-t} dt - \left(\int_0^{\infty} \log t e^{-t} dt \right)^2.$
The standard deviation of $\eta = [E(\eta^2) - (E(\eta))^2]^{\frac{1}{2}} = \pi/(6)^{\frac{1}{2}}$.

Magnetization in Perpendicularly Superposed Direct and Alternating Fields

F. J. Beck and J. M. Kelly*
Yale University, New Haven, Connecticut
(Received January 15, 1948)

The magnetic properties of an iron specimen under the influence of perpendicularly superposed direct and alternating fields are investigated. For the low and intermediate values of direct longitudinal magnetic field intensity the steady component of the longitudinal intensity of magnetization first increases, goes through a maximum, and then diminishes as the transverse alternating magnetic field intensity is increased. Static hysteresis loops in the longitudinal direction show a suppression of hysteresis with increasing transverse alternating magnetic field intensity. However, dynamic hysteresis loops in the transverse direction indicate that this suppression is merely apparent. Curves of the dynamic longitudinal magnetic induction *vs.* transverse magnetic field intensity and transverse magnetic induction are included.

INTRODUCTION

SINCE ferromagnetic materials are often operated under the combined influence of direct and alternating magnetizing forces, as in the case of transformer coupled amplifiers, magnetic amplifiers, and airborne magnetometers, a knowledge of the resulting magnetization is of considerable value. Of perhaps greater importance is the fact that such information may prove significant in providing a clearer understanding of the magnetization process.

The use of a superposed alternating magnetic field to suppress the effects of hysteresis was demonstrated by Ashworth[1] for iron and nickel wires. His specimens were magnetized longitudinally by means of a coaxial solenoid through which a direct current was passed and transversely by causing an alternating current to flow along the wire. Curves of the steady component of the intensity of magnetization against alternating current, with the direct longitudinal magnetic field intensity as a parameter, are given for the case of iron. Wright[2] and Niwa and Asami[3] working with superposed coaxial longitudinal fields obtained results which are in essential agreement with those of Ashworth.

Recent work in the subject has followed a somewhat different course from the earlier work. Webb[4] has investigated the variation of incremental permeability of iron, nickel, and a nickel iron alloy with the direct longitudinal field, when the wire specimens are traversed with an alternating current of frequency of 10^6 cycles per second. In general, the incremental permeability decreases with the direct longitudinal magnetic field intensity approximately in a hyperbolic fashion. In a similar study, Gorelik,[5] through measurements of internal impedance at a frequency of 16,000 cycles per second, reports results which are in general agreement with those of Webb. In a subsequent communication Gorelik, Goronina, and Joukova[6] give the ballistically determined hysteresis loops in the longitudinal direction, with the direct current which flows along the nickel-iron wire as a parameter. The loops exhibit suppression of

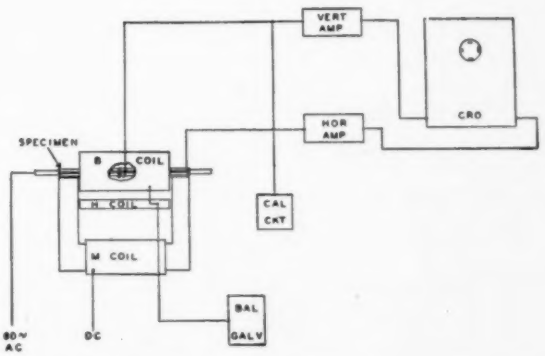

FIG. 1. Block diagram of circuit arrangement.

* Dunham Laboratory of Electrical Engineering, Yale University. Assisted by contract N6ori-44, Task Order 13 of the Office of Naval Research.

[1] J. R. Ashworth, Phil. Mag. **27**, 357 (1914).
[2] W. R. Wright, Phys. Rev. **11**, 161 (1918).
[3] Y. Niwa and Y. Asami, Dept. of Com., Tokyo Tech Reports No. 124 (1923).
[4] J. S. Webb, Proc. I.R.E. **26**, 433 (1938).
[5] G. Gorelik, Comptes Rendus U.R.S.S. **43**, 196 (1944).
[6] G. Gorelik, X. Goronina, and I. Joukova, Comptes Rendus U.R.S.S. **44**, 235 (1944).

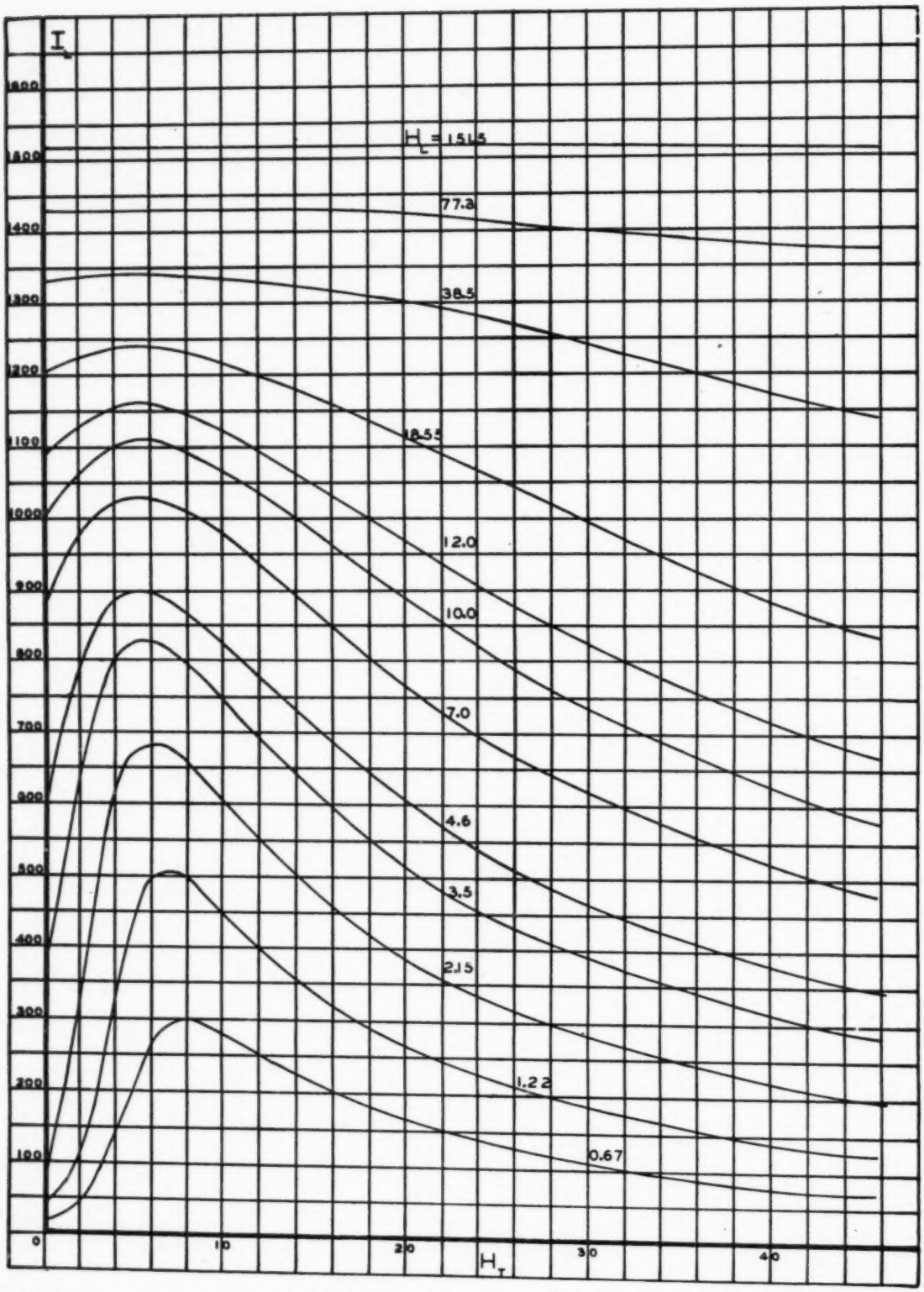

FIG. 2. Steady component of the longitudinal intensity of magnetization in gauss *vs.* the maximum value of the transverse alternating magnetic field intensity in oersteds with the longitudinal magnetic field intensity as a parameter.

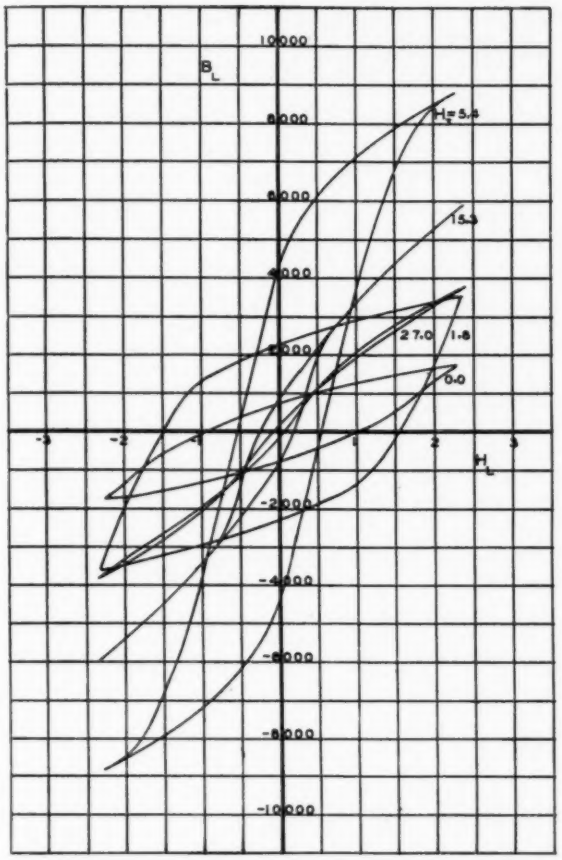

FIG. 3. Static hysteresis loops for a tip value of the longitudinal magnetic field intensity of 2.3 oersteds and with the r.m.s. value of the transverse alternating magnetic field intensity as a parameter.

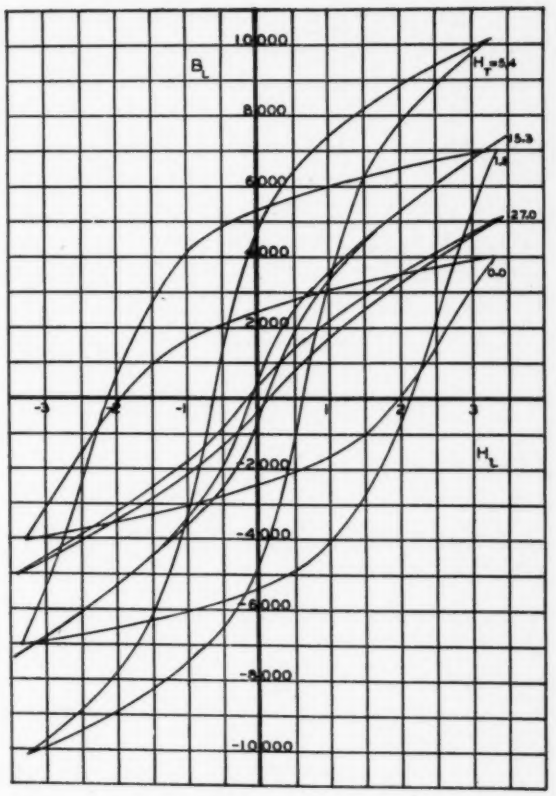

FIG. 4. Static hysteresis loops for a tip value of the longitudinal magnetic field intensity of 3.3 oersteds and with the r.m.s. value of transverse alternating magnetic field intensity as a parameter.

hysteresis in the longitudinal direction and increasing linearity of the relation between B_L and H_L as the alternating current is increased. Berstein[7] has considered the variation in alternating e.m.f. produced in a search coil linking the longitudinal field as a function of the direct longitudinal magnetic field intensity and with the alternating magnetic field intensity as a parameter. He finds that the e.m.f. rises to a maximum value for the low values of direct longitudinal magnetic field intensity and then diminishes as the direct longitudinal magnetic field intensity is further increased.

In the present work the specimen is in the form of a long hollow cylinder which permits the determination of the magnetization in the direction of the cylinder axis (longitudinal axis) and in the circumferential direction (transverse axis). The direct field is applied along the longitudinal axis and the alternating field along the transverse axis. Ballistic (quasi-static) measurements may be made in the longitudinal direction, and dynamic or oscillographic measurements may be made in both the longitudinal and transverse directions. It was felt that this arrangement which permits both static and dynamic observations would give additional information regarding the magnetization in superposed direct and alternating fields.

APPARATUS

The specimen was a seamless iron pipe 25.4 cm long, of 1.15-cm inside diameter and 1.28-cm outside diameter. It was given no heat treatment and its past history was unknown. Magnetic measurements gave a value $I_s = 1530$ gauss for the saturation value of the intensity of magnetization.

[7] I. Berstein, Comptes Rendus U.R.S.S. **43**, 380 (1944).

The specimen was suitably mounted in a Fahy Simplex Permeameter excited by a storage battery. By means of the permeameter "B" and "H" coils, a ballistic galvanometer, and conventional circuit arrangements, it was possible to obtain static magnetization curves and hysteresis loops in the longitudinal direction.

The field in the transverse direction was obtained by mounting a brass conductor, 0.95 cm in diameter, axially in the specimen. This conductor was excited from a 110-volt, 60-cycle supply through a step-down transformer, current being controlled by means of an induction regulator in the primary circuit of the transformer. Precautions were observed in the physical arrangement of the direct and alternating current circuits so that the coupling between these circuits was a minimum. The mean magnetic field intensity within the specimen in the transverse direction is given by

$$H_T = 6.38i,$$

where i is the instantaneous value of the alternating current in amperes.

A coil of 70 turns of AWG No. 34 Formex wire was threaded through the specimen and wound closely to the tube wall to provide a means of determining the transverse magnetic induction (B_T).

A coil of 550 turns of AWG No. 30 Formex wire was wound on a Bakelite form which fitted the specimen snugly and was placed at the middle of its length for the measurement of the dynamic longitudinal magnetic induction (B_L).

Care was taken in the winding and placement of these coils so that the coupling between them was minimized.

The voltage across a resistor in series with the brass conductor measured the transverse magnetic field intensity.

In order to obtain the instantaneous magnetic induction B_T and B_L it was necessary to provide each search coil with a resistance-capacity integrating circuit. Such an integrating circuit should introduce little phase shift and provide a reasonable signal output. These two requirements conflict, so that compromise values of R and C must be selected. The values employed were $R=1$ megohm, and $C=0.1$ μf, which gave satisfactory signal output and an acceptable phase shift.

The output from the longitudinal search coil integrating circuit was connected to a General Radio voltage amplifier and thence to the vertical deflecting plates of a DuMont oscilloscope through the vertical oscilloscope amplifier in cases where this output was of interest. In a similar fashion the output of the transverse search coil integrating circuit or the voltage across the resistor in the alternating magnetizing

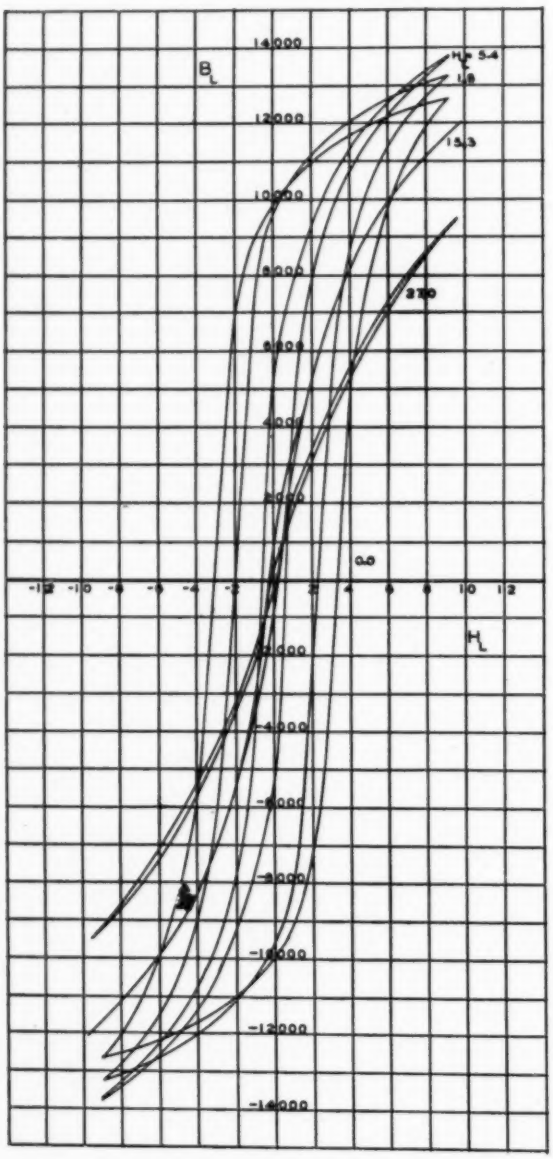

FIG. 5. Static hysteresis loops for a tip value of the longitudinal magnetic field intensity of 9.5 oersteds and with the r.m.s. value of the transverse alternating magnetic field intensity as a parameter.

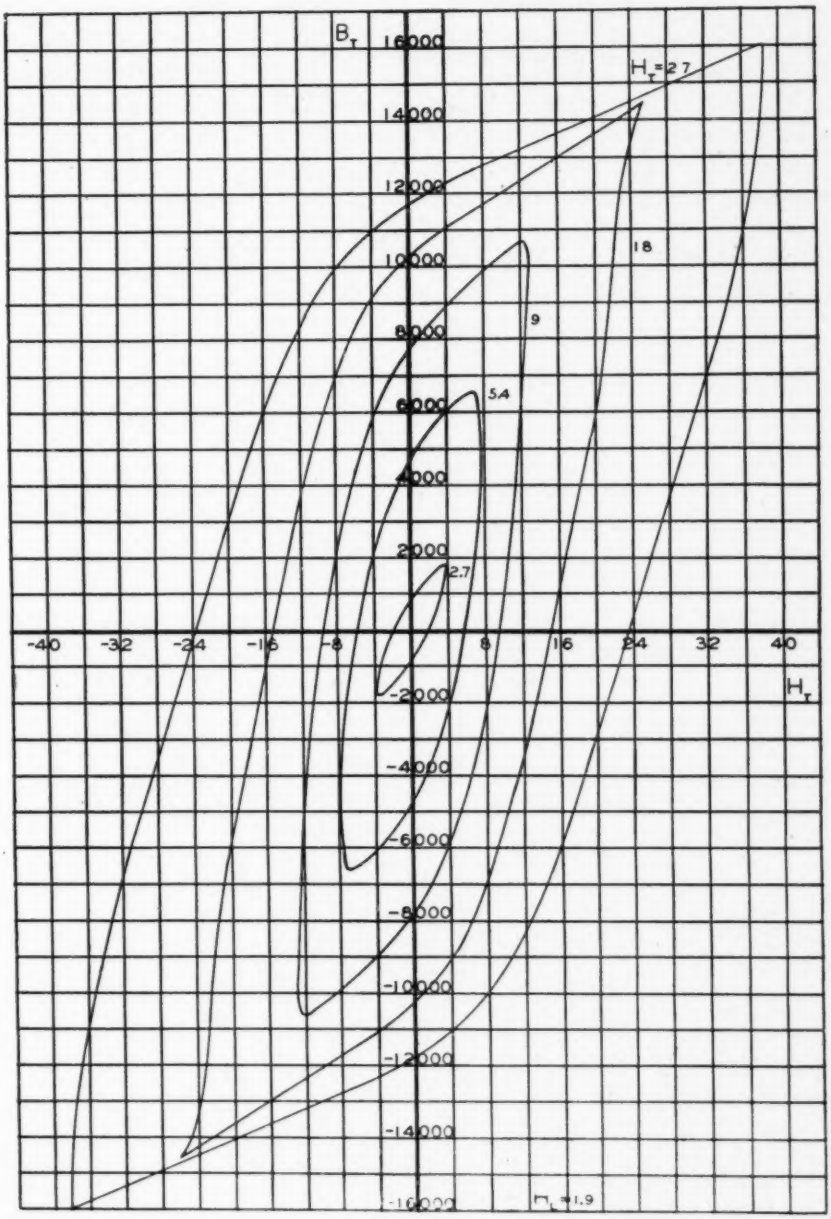

FIG. 6. Dynamic hysteresis loops for a given value of longitudinal magnetic field intensity of 1.9 oersteds and for selected r.m.s. values of the transverse alternating magnetic field intensity.

circuit was connected to an identical General Radio voltage amplifier, and thence either to the vertical or horizontal deflecting plates of the oscilloscope, through the corresponding oscilloscope amplifier. It was thus possible to observe the dynamic variations of B_L, B_T, and H_T as a function of time, or the (B_L, H_T), (B_L, B_T), and (B_T, H_T) loops.

A sine wave calibrating circuit was provided so that each amplifying circuit could be separately calibrated and also so that the wave shape of the alternating magnetic field intensity could be compared with the sine wave. It was found that the distortion of the alternating magnetizing current caused by harmonics was inappreciable over the range of alternating magnetic field intensities investigated.

Figure 1 illustrates in block diagram form the essential features of the experimental arrangement.

EXPERIMENTAL

Ballistic Measurements

To obtain the curves of Fig. 2 the specimen was demagnetized by reversals of a gradually reducing longitudinal field. The longitudinal magnetic field intensity was then increased to a particular value and the material brought to a steady cyclic state by reversals. Ballistic measurement between loop tips then gave the steady longitudinal component of magnetic induction from which the steady longitudinal component of the intensity of magnetization was computed. With the longitudinal magnetic field intensity maintained at the set value, the transverse alternating magnetic field intensity was increased from zero to a selected value and the material again brought to a steady cyclic state by reversals. The steady longitudinal component of the intensity of magnetization was then found

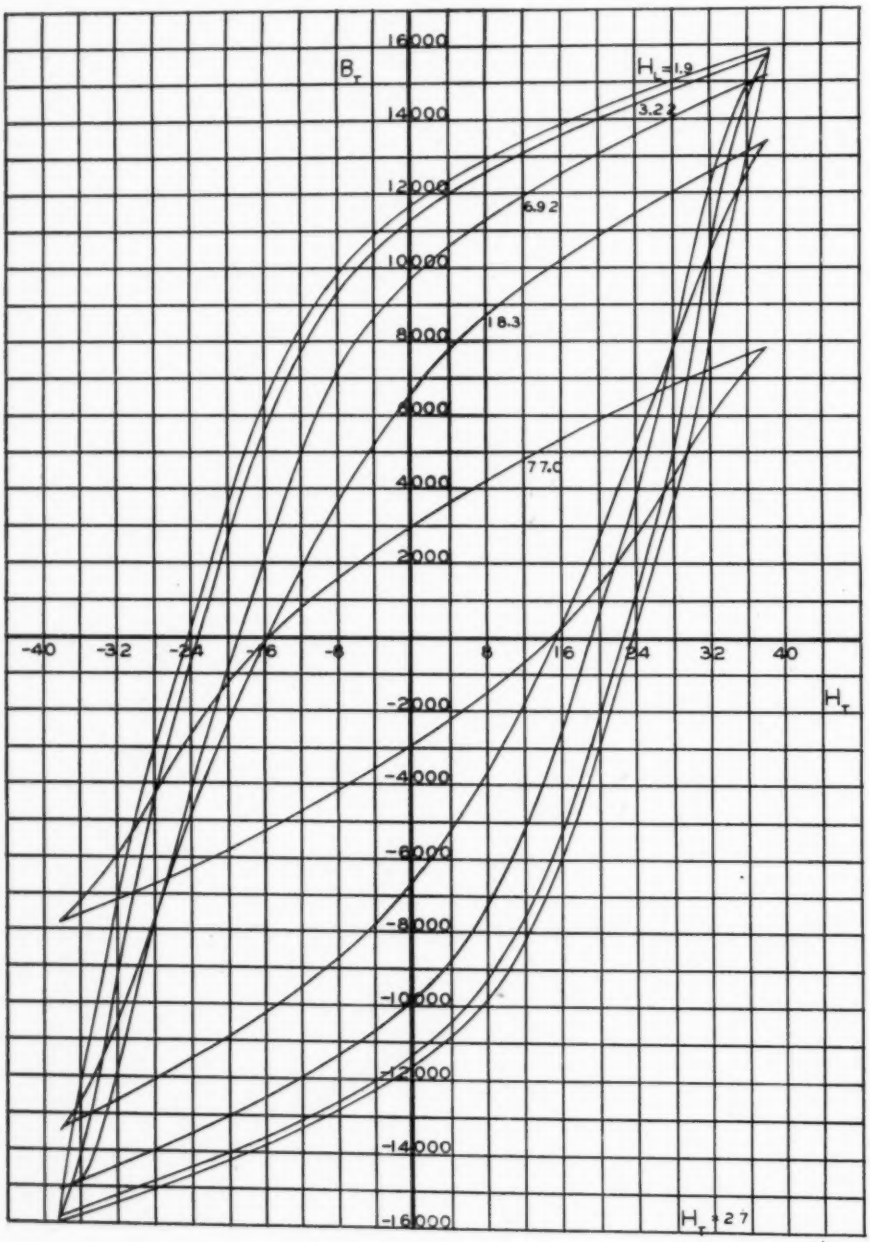

FIG. 7. Dynamic hysteresis loops for a given r.m.s. value of the transverse alternating magnetic field intensity of 27.0 oersteds and for selected values of the longitudinal magnetic field intensity.

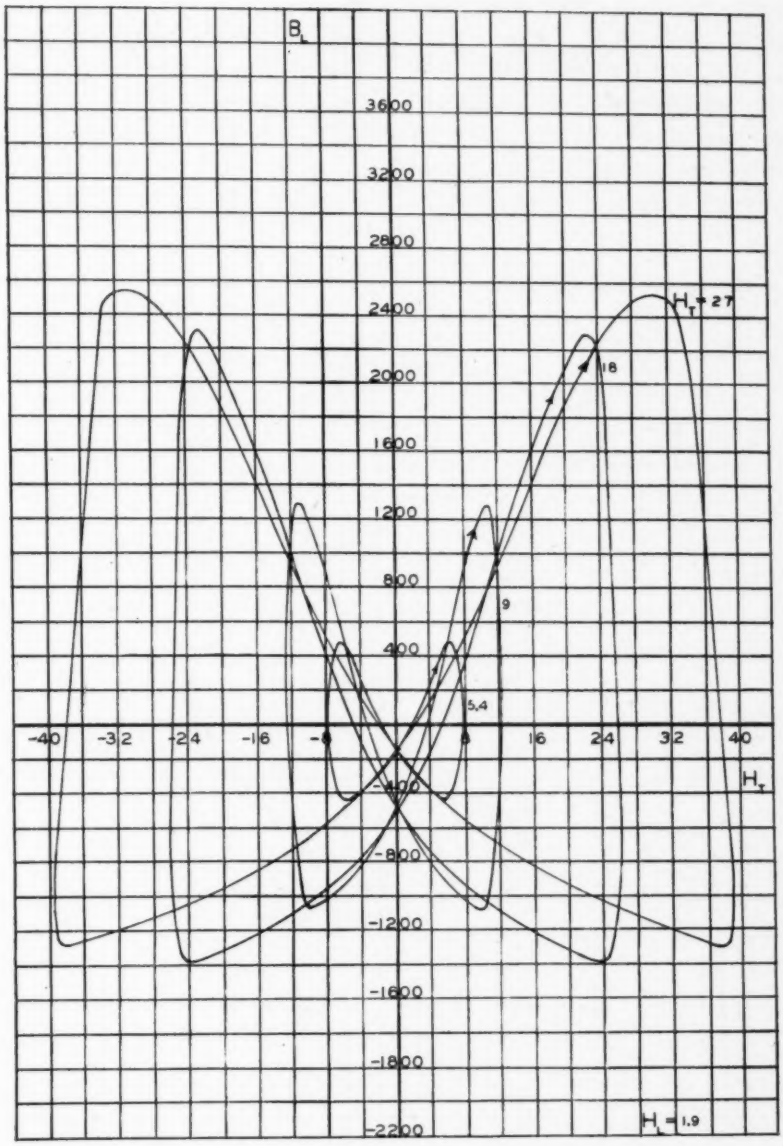

FIG. 8. Dynamic component of the longitudinal magnetic induction *vs.* the transverse alternating magnetic field intensity for a given longitudinal magnetic field intensity of 1.9 oersteds and with the r.m.s value of the alternating magnetic field intensity as a parameter.

for this new state. This procedure was repeated for selected increased values of the transverse magnetic field intensity to $H_{T_{max}} = 45$ oersteds and for the same steps as the transverse magnetic field intensity was returned to zero. Continuing this process for different values of the longitudinal magnetic field intensity gave the family of curves of Fig. 2. Single curves are drawn for both increasing and decreasing H_T.

The static hysteresis loops along the longitudinal axis, illustrated in Figs. 3, 4, and 5, were obtained in the following manner. The material was demagnetized by reversals and then a particular r.m.s. value of the transverse magnetic field intensity was maintained and the hysteresis loop determined in the conventional way. This procedure was repeated for selected tip values of the longitudinal magnetic field intensity with the r.m.s. value of the transverse magnetic field intensity as a parameter.

Dynamic Measurements

If symmetry exists about the longitudinal axis and the transverse axis separately, and if the coupling between the longitudinal and transverse circuits is zero, the changes along the longi-

tudinal axis resulting from transverse alternating fields should have frequencies of 120 cycle per second and multiples thereof, while those along the transverse axis should contain 60 cycle per second changes and its odd harmonics. Any small amount of coupling or slight asymmetry about either axis appears as an asymmetry of the dynamic loops obtained along the longitudinal axis. With the present arrangement it was impossible completely to eliminate the effect of coupling and the effect of slight geometrical asymmetry. It was found, however, that a small amount of torsion could be applied in such a sense as nearly to compensate for the asymmetry

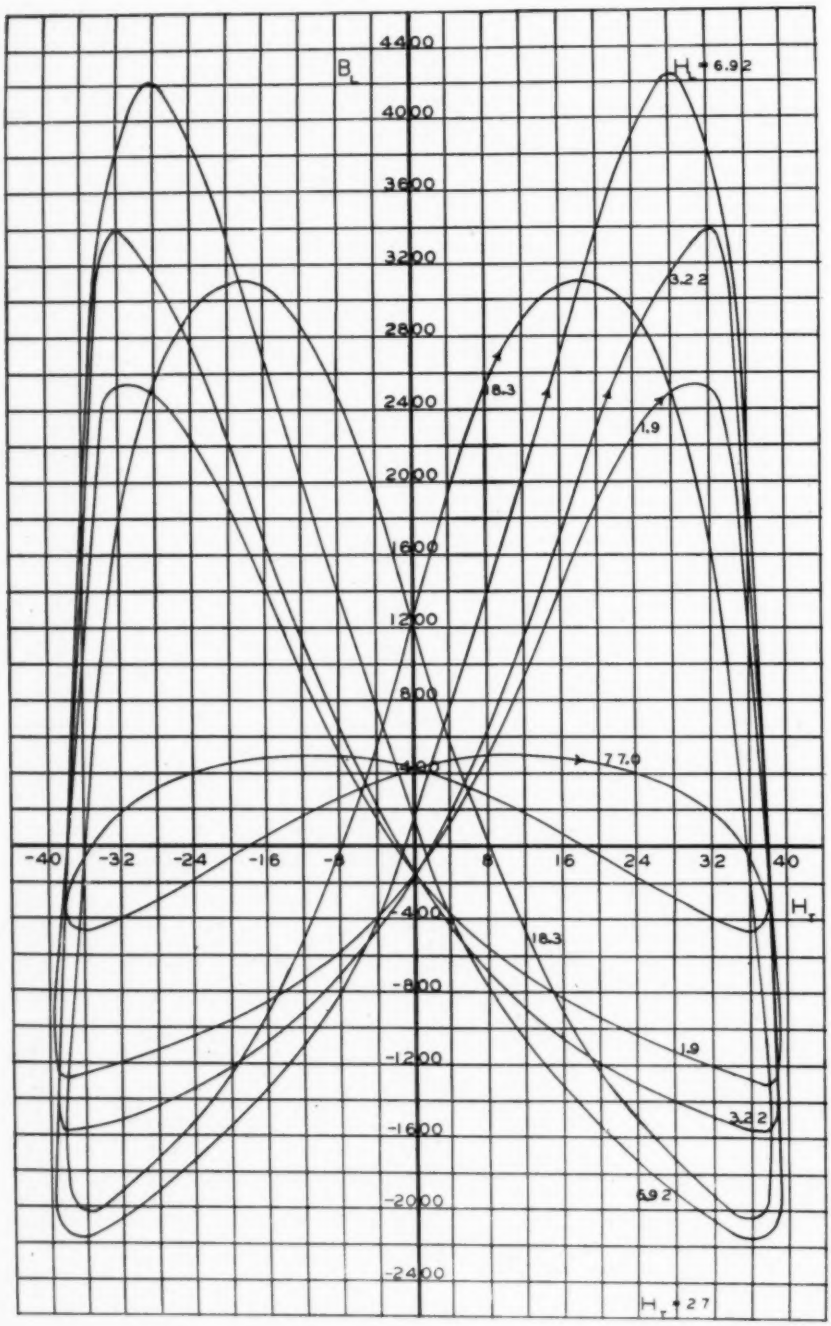

FIG. 9. Dynamic component of the longitudinal magnetic induction *vs.* the transverse alternating magnetic field intensity for a given r.m.s. value of the transverse alternating magnetic field intensity of 2.7 oersteds and with the longitudinal magnetic field intensity as a parameter.

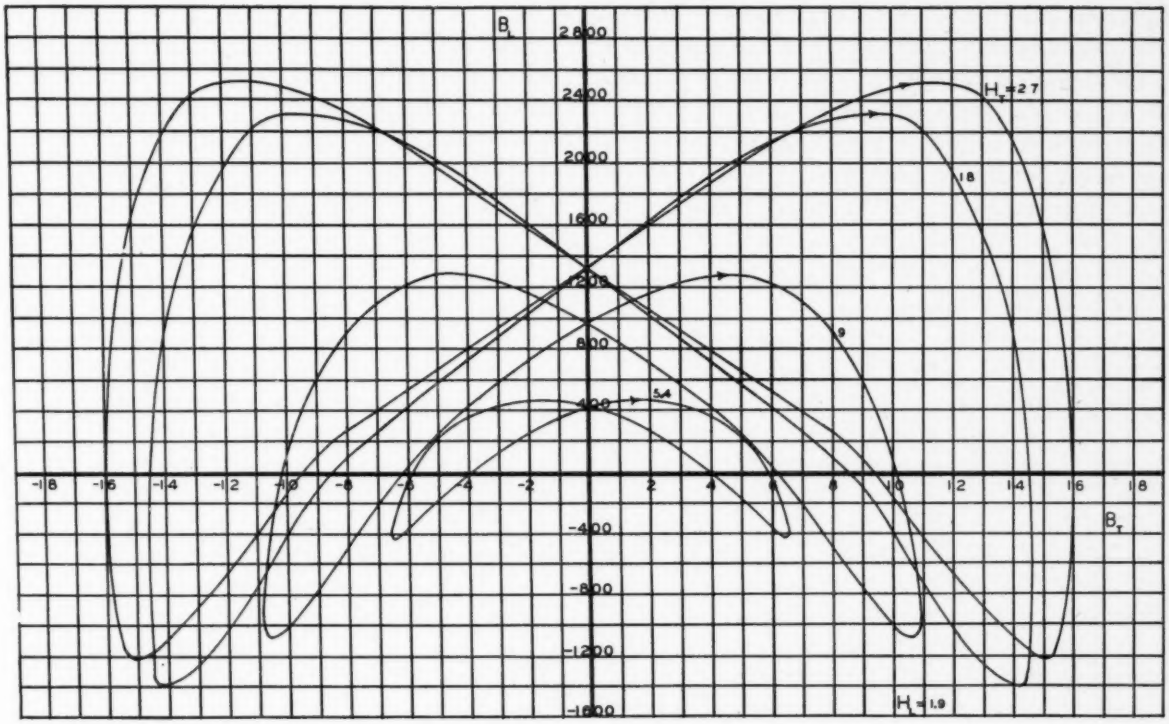

FIG. 10. Dynamic components of the longitudinal magnetic induction *vs.* the transverse magnetic induction for a given value of the longitudinal magnetic field intensity and with the r.m.s. value of the transverse magnetic field intensity as a parameter.

of the observed loops. This was accomplished by a slight change of pressure on the permeameter clamps. This torsion inappreciably affected the static measurements.

To obtain the dynamic loops the specimen was first demagnetized and then the direct longitudinal magnetic field intensity was adjusted to a particular value and the material brought to a steady cyclic state by reversals of this value. The alternating magnetic field intensity was then increased from zero to a given value and the loop, observed on the oscilloscope screen, was adjusted for symmetry by changing permeameter clamping. The calibrating signal was next applied to each circuit and the shape of the alternating magnetic field intensity against a time sweep was compared with the sine wave calibrating signal. The loop was finally re-established on the oscilloscope screen and photographed. The loops here given, selected as typical, were drawn from enlargements of the photographs and are plotted in terms of B and H as determined from the calibrating data.

The curves of Fig. 6 are the dynamic hysteresis loops in the transverse direction which were obtained for a longitudinal magnetic field intensity $H_L=1.9$ oersteds and for a range of r.m.s. values of transverse magnetic field intensity. Those of Fig. 7 are the dynamic hysteresis loops in the transverse direction for an r.m.s. transverse magnetic field intensity of $H_T=27$ oersteds and for selected values of longitudinal magnetic field intensity.

Figure 8 is a plot of the dynamic longitudinal magnetic induction, B_L, against the instantaneous transverse magnetic field intensity, H_T, for a given longitudinal magnetic field intensity, $H_L=1.9$ oersteds, and with the r.m.s. value of the transverse magnetic field intensity as a parameter. In Fig. 9 is plotted a similar family of curves for a given r.m.s. value of the transverse magnetic field intensity, $H_T=27.0$ oersteds, and with the longitudinal magnetic field intensity as a parameter.

The curves of Figs. 10 and 11 present similar data to those of Figs. 8 and 9, respectively, ex-

cept that B_L is here plotted against the instantaneous transverse magnetic induction, B_T.

Photographs of $B_L=f(t)$ were also obtained. Making the assumption that the transverse magnetic field intensity varied sinusoidally, the transverse hysteresis loops were used to reconstruct the loops of Figs. 8, 9, 10, and 11. The agreement was satisfactory, indicating that H_T was sinusoidal over the range of magnetic intensities investigated.

DISCUSSION

The family of curves shown in Fig. 2 are similar to those previously obtained by Ashworth,[1] Niwa and Asami,[3] and may be interpreted in the following manner. The changes in magnetization occasioned by the transverse field in a tangent plane are subject to the control of the longitudinal field. As the transverse field is first increased, the changes in magnetization exhibit an increased longitudinal component be-

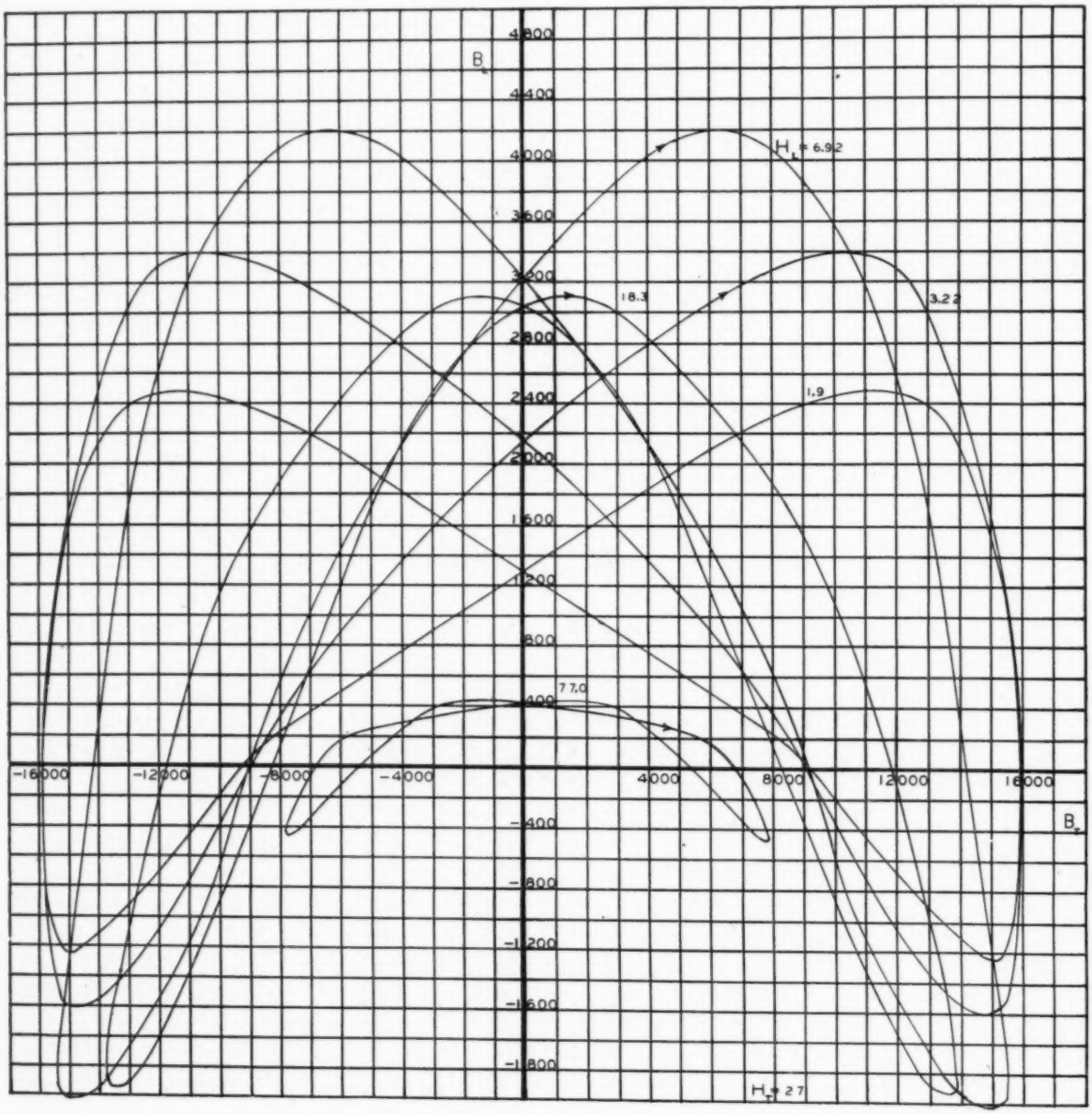

FIG. 11. Dynamic component of the longitudinal magnetic induction *vs.* the transverse magnetic induction for a given r.m.s. value of the transverse alternating magnetic field intensity of 27 oersteds and with the longitudinal magnetic field intensity as a parameter.

cause more material is, at some state in the transverse cycle, under control of the longitudinal field. Further increase in the transverse field shifts the control for more of the cycle to the transverse field itself, and the longitudinal component of the intensity of magnetization then diminishes. Thus, the curves of Fig. 2 for the low longitudinal magnetic field intensities show a rapid increase of the longitudinal component of the intensity of magnetization to a maximum value and a subsequent nearly hyperbolic decrease as the transverse magnetic field intensity increases. For the intermediate values of the longitudinal magnetic field intensity the initial increase is relatively less and occurs at smaller H_T in agreement with the fact that the transverse field now merely disturbs a predominantly longitudinal magnetization. For the large values of longitudinal magnetic field intensities the control by the longitudinal field is sufficiently strong to inhibit changes in magnetization in the transverse direction almost completely over the range of transverse field studied.

The maximum values of the magnetic induction for the static hysteresis loops of Figs. 3–5 are seen to follow the paths of the corresponding curves of Fig. 2. Thus for a low longitudinal field the maximum value of the magnetic induction at first increases appreciably as the transverse field is increased. This increase brings about an increase in the remanent induction and a corresponding increase in the coercive force for the low transverse fields. Thus the area of the static hysteresis loop at first increases. For the larger transverse fields both the remanent induction and the coercive force decrease, the loop area diminishes, and the loop is sheared toward the H axis. For the intermediate value of longitudinal field the remanent induction and the coercive force continually diminish as the transverse field is increased, the area of the loop diminishes, and its sides become more nearly linear. These results are in essential agreement with those of Gorelik, Goronima and Joukova.[6]

The dynamic hysteresis loops in the transverse direction, as illustrated in Fig. 6 for a particular value of longitudinal magnetic field intensity, show, as expected, an increasing area as the transverse magnetic field intensity is increased. It is seen from this that the suppression of hysteresis indicated by the narrowing of static loops is merely apparent. Alternating current losses are still substantial under these conditions. When the transverse magnetic field intensity is held at a constant r.m.s. value and the longitudinal magnetic field intensity is increased, the area of the dynamic hysteresis loops decreases as illustrated in Fig. 7. Here the changes in magnetization occasioned by the transverse field diminish as the longitudinal magnetic field intensity is increased. Thus, the maximum value of the induction, the remanent induction, and the coercive force all decrease as the strength of the longitudinal control field increases. The loops collapse and shear toward the axis of H, the alternating current permeability decreasing in a manner similar to the decrease in incremental permeability observed by Webb[4] and Gorelik.[5]

In addition to the change in the static component of the longitudinal intensity of magnetization associated with the alternating transverse magnetic intensity, there will be a dynamic change. For steady-state conditions the dynamic longitudinal component of the magnetic induction should return to its original value at the end of each half-cycle. Also symmetry requires that there be no 60-cycle component of the dynamic $B_L=f(t)$ curves. The condition

$$\int_0^{T/2} B_L dt = 0$$

is borne out by experiment. Thus, in each half-cycle the dynamic magnetic induction will reach a maximum in the positive direction, pass through zero, reach a maximum in the negative direction, and return to its original value. In Fig. 8 one would expect the general features of all curves to be similar, regardless of transverse magnetic field intensity, but that the range of B_L would reach a limiting value at high H_T because of saturation in the transverse direction. This is seen to be essentially the case, the positive maximum of the dynamic magnetic induction increasing and reaching a limiting value, while the negative maximum first increases and subsequently decreases preserving the condition that the

$$\int_0^{T/2} B_L dt = 0.$$

The same general shape of curve would be expected for each of the curves of Fig. 9. As the longitudinal field is increased the dynamic magnetic induction should first increase since changes from the transverse to the longitudinal direction are favored. However, as the longitudinal field is further increased, the total change in magnetization associated with the transverse field will decrease. Thus, one would expect the range of values of B_L to increase, reach a maximum, and decrease thereafter. This is precisely the type of variation observed by Berstein[7] for the longitudinal e.m.f. As the longitudinal field is increased, less change in magnetization occurs in the transverse direction, and as a result the maximum value of the dynamic magnetic induction in the positive direction shifts toward the lower values H_T.

The variation of the cross-over point of the previous curves on the B_L axis may be more easily understood in terms of the dynamic B_L *vs.* B_T curves. For zero value of the transverse magnetic induction the longitudinal field exerts the only control, so that a positive longitudinal component of the dynamic magnetic induction should always occur at this point. As the transverse magnetic intensity is increased for the curves of Fig. 10, the cross-over point should rise and reach a limiting value as saturation is approached in the transverse direction. Since these curves may be constructed from the corresponding B_T *vs.* H_T and B_L *vs.* H_T curves, it is seen that the variation of the cross-over points in Figs. 8 and 9 is determined by the shape of the hysteresis loops in the transverse direction. The same comments hold for the curves of Fig. 11. When the longitudinal field is made sufficiently great, the dynamic longitudinal magnetic induction corresponding to $B_T=0$ decreases since the whole change along the transverse axis has been reduced. The shift of the positive maximum value of the dynamic magnetic induction in this method of plotting may be great enough to occur at a negative value of the B_T (though at a positive value of H_T on the hysteresis loop). This is illustrated by the curve for $H_L=77$ oersteds and gives rise to the two additional cross-over points in the first and second quadrants.

It is felt that studies of this type, under more precise experimental conditions, and on different ferromagnetic materials subjected to controlled mechanical and thermal treatments, will be of value in obtaining a better understanding of the process of magnetization. The method allows almost any desired cyclic variation of H in a thin lamina (between cylindrical surfaces) and the simultaneous determination of two components of B in this lamina. The effects of demagnetizing fields are substantially zero. Anisotropic states are easily produced in such specimens.

We wish to express our gratitude and acknowledge our indebtedness to Dr. L. W. McKeehan for many helpful discussions of this work.

Explosives with Lined Cavities*

GARRETT BIRKHOFF, DUNCAN P. MACDOUGALL, EMERSON M. PUGH, AND SIR GEOFFREY TAYLOR**

(Received January 16, 1948)

Explosives detonated in contact with thick steel plates produce much deeper holes in the steel when there is a cavity in the explosive in contact with the plate. While this phenomenon has been known for more than 150 years, the enormous increase in penetrating power that can be produced by lining the explosive cavity with thin metal has been discovered only recently. During the war a number of light, low velocity, antitank weapons (e.g., the rocket-propelled Bazooka) were developed which made use of this phenomenon to perforate thick armor plate.

A fairly complete mathematical theory of this essentially new phenomenon is presented together with some of the experimental data that aided in the formulation and testing of the theory. The process is separated into two phases: first, the formation of part of the metal liner into a long thin jet traveling longitudinally at very high velocities (30,000 ft./sec.) and, second, the forcing aside of the target material by the extremely high pressures (0.3-million atmos.) produced by the impact of the high speed jet.

The theories of both of these phases are based upon the classical hydrodynamics of perfect fluids, which is applicable because the strength of the metals involved can be neglected at the high pressures encountered.

FOR over a century mining engineers have known that some of the force of an explosive charge could be concentrated on a small area by hollowing out the charge opposite to the area ("hollow charge principle"). The earliest known reference to this is 1792; a popular account appeared in von Nostrand's Magazine in 1884. The effect became known as the Munroe effect in England and the United States, and as the Neumann effect in Germany, in honor of later workers (1885, 1911).

Early in the recent war a large number of new weapons, based on an important modification of this principle, appeared almost simultaneously in the armed forces of the major combatants. It had been discovered that by lining the hollow with a thin metal liner it became possible to perforate armor plate, concrete walls, or other structures with a surprisingly small weight of explosive charge. Very often these new weapons took the form of a projectile with the lined hollow charge in the nose. Such projectiles had an advantage over the ordinary artillery projectiles in that their ability to perforate was practically independent of their striking velocity. In fact, hand placed and statically detonated hollow charges are at least as effective in perforating armor as those used in projectiles which detonate on impact.

This fact led to a variety of methods of getting the hollow charges to their target. The best known method was the use of rocket propulsion employed in the American and German bazookas which were very effective against tanks, although they had striking velocities far below those of the ordinary antitank artillery projectile. The American bazooka could be carried and operated by individual infantrymen. A cross section of the head of this weapon is shown in Fig. 1. The rocket motor which propelled this projectile is not shown in the figure, since that part of the bazooka has been well publicized. When the windshield or ogive strikes a tank, the impact causes the inertial striker pin in the fuse to detonate the charge. The resulting explosion collapses the steel cone liner into a high speed jet of steel which perforates the armor and sets fire to ammunition, gasoline, or oily waste within the tank. The Germans also had another shaped-charge weapon that could be used by their individual infantrymen to defeat tanks. This

* Published by permission of the Chief Scientist, British Ministry of Supply, and the U. S. War and Navy Departments. Except where otherwise noted, the mathematical theories presented here were developed by the authors during the latter part of 1943 and the early part of 1944 while working in England under the auspices of the British Ministry of Supply, Division of Scientific Research and Technical Development, and in the United States in Divisions 2 and 8 of the National Defense Research Committee and the Ballistic Research Laboratory at the Aberdeen Proving Ground under the auspices of the joint Army-Navy-NDRC Committee on Shaped Charges.

** The authors' names are arranged alphabetically: Garrett Birkhoff, Harvard University; Duncan P. MacDougall, Naval Ordnance Laboratory, Washington, D. C.; Emerson M. Pugh, Carnegie Institute of Technology; Sir Geoffrey Taylor, F.R.S., Trinity College, Cambridge, England.

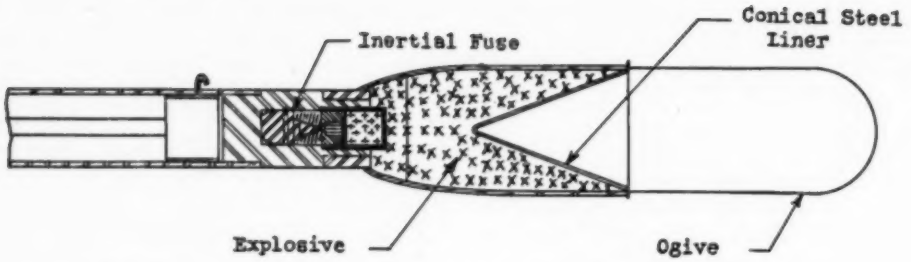

FIG. 1. Cross section of the head of a U. S. Army bazooka, showing conical steel liner in the shaped charge.

weapon, called the Panzerfaust, was launched from a small light steel pipe employing the recoilless mortar principle. It is a rather large shaped-charge projectile stabilized in flight by tail fins. All of these weapons were briefly described in the Popular Science of February, 1945. They made it possible for an infantryman operating from ambush to defeat the largest tank. The Germans also had a shaped-charge weapon for hand placing which was equipped with permanent magnets to hold it to a tank until its time fuse set it off. Characteristically, the Japanese developed a shaped charge (Lunge mine) fastened to the end of a long wooden pole. The Japanese solider was expected to charge out from ambush and jam this charge against the side of a tank. Obviously it was another suicide weapon designed on the principle that the life of one or two Japanese soliders was not too high a price to pay for the destruction of a tank.

Since the ability of these weapons to pierce targets is independent of the striking velocity, much of the experimental work has been done with statically fired charges. Figure 2 shows a typical experimental hollow charge lined with a steel cone. When the booster is detonated, it starts an explosive wave which travels parallel with the axis of the charge and collapses the steel cone starting from its apex. The collapsing cone forms a long thin jet of steel that travels to the right in the figure along the extension of the cone axis at speeds up to 30,000 ft./sec.[1] These high speed jets force their way through armor plate in much the same way as a stream of water from a powerful fire hose would force[2] its way through a bank of soft mud. The pressures produced by the jet traveling at these high velocities are so much greater than the ultimate strength of the armor plate that the strength of the armor plays a negligible role in retarding the penetration. In fact, mild steel provides almost as much protection as hard-steel armor against these weapons.

The lined hollow-charge principle is such a unique and surprising phenomenon that a great deal of thought has been given to possible peacetime applications. Of the many suggestions that have been advanced, only a few have proved to be practical, since the desired results can often be accomplished as well or better in other ways.

Shaped charges have frequently been used for the rapid boring of holes in demolition work. After a hole has been blown with a shaped charge, the cavity can be filled with explosive for further blasting. Such a procedure is quick and easy, but because of the relatively high cost of the explosives used in shaped charges it can seldom be justified on a cost basis. High explosives of the type used in military operations are needed to obtain satisfactory performance with shaped charges. The performance with the cheaper dynamites and other low pressure explosives is definitely inferior.

[1] Rifle bullets ordinarily have muzzle velocities around 2000–3000 ft./sec., though with special devices projectiles have been shot from gun barrels up to 5000 ft./sec. F. Zwicky and F. Whipple have suggested using these jets as artificial meteors for controlled studies, since their velocities are about the same as the velocities of the slower meteors. Shaped charges are carried to the upper atmosphere by V-2 rockets and exploded when the rocket has reached its highest point. Calculations indicate that these "meteors" should be observable from the ground.

[2] Like most analogies this is far from perfect, for while a stream of water washes mud *out* of a mud bank the jet of metal does not wash or erode metal out of the target. Careful weighings have shown that a metal jet is captured by a metal target, which loses no weight except a very small amount at the front surface. The hole is produced by plastic flow of the target material in a radial direction.

Charges lined with linear wedges have been used for cutting cables and bridge beams and in salvage work on sunken ships. A long charge lined with a long linear wedge of metal can be used for cutting in two a large steel plate of a sunken ship with less danger to the workmen than that encountered in using a torch for such an operation. This appears to be quite practical.

A patent[3] has recently been applied for on the use of a group of these charges for increasing the production in certain oil wells. The charges are lowered into a well and fired in such a way as to produce radial holes through the casing and into the surrounding rock structure to increase the oil seepage into the well. This method appears to be superior to the method of cracking the casing and its surroundings with an ordinary charge.

Shaped charges can be used to break large rocks. In some mining operations they may be better than other charges for this purpose. However, recent tests indicate that the effectiveness of a given weight of explosive in breaking rocks is not increased appreciably by forming it into a shaped charge.

It should be possible to use the hollow-charge principle for investigating strength properties of various kinds of materials when they are subjected to exceedingly high pressures. Under favorable conditions these charges produce dynamic pressures, on small areas and for short periods of time, higher than a quarter of a million atmospheres.[4] By varying the kind of explosive and the shape and material of the lining it should be possible to obtain a well graded series of such ultra-high dynamic pressures. The information that can be obtained at these pressures is, of course, severely limited by the difficulties inherent in the control and observation of the results. Preliminary experiments nevertheless indicate that it will be possible to design charges that can be used to determine the ultimate stresses in materials at these very high rates of strain. This information may throw more light on the rate of propagation of dislocations in metallic crystals and of microcracks in glasses. There are at least three types of experiments, each of which may yield information on ultimate shear stresses so that the results of one type may be used to check the results from the other. One type involves the measurement of hole volumes and hole contours when the material is used as a target for standard charges. Another involves the measurement of the depth of the residual penetration, into a standard material like soft steel, of a jet from a standard charge after it has perforated a given thickness of the material tested. A third involves a measurement of the velocity of perforation of the jet through the material. There are still a number of difficulties involved in the interpretation of the results of these three types of experiments which, it is hoped, may be resolved after a more thorough understanding of the phenomenon is obtained.

The linings for hollow charges have been made with a variety of materials and a variety of geometrical shapes. Many different kinds of liners were used in combat weapons. Hemispheres, paraboloids, pear shapes, and trumpet shapes were all tried. None of them appeared to provide remarkable advantages over any of the others, though differences in performance did result from the different shapes. In at least one combat zone hollow charges were improvised by molding plastic explosive around the outside of lamp reflectors that had been salvaged from disabled motor cars.

Hollow conical liners for penetration and hollow wedge-shaped liners for cutting have been encountered most frequently and have been most thoroughly investigated. Both of these shapes are very effective for the purposes for

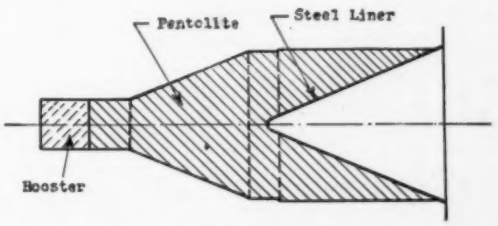

FIG. 2. A typical shaped charge with conical steel liner for use in static experiments. This charge contains 115 g of Pentolite which has a maximum diameter of 1⅜ in. The steel liner is 0.025 in. thick.

[3] Robert H. McLemore, "Formation penetrating with shaped explosive charges," Oil Weekly July 8 (1946).

[4] P. W. Bridgman has measured static pressures up to 100,000 atmospheres, in spaces $\frac{5}{16}$ in. long and $\frac{1}{16}$ in. thick, and has obtained pressures estimated at 400,000 atmospheres but was unable to make observations at the higher pressures.

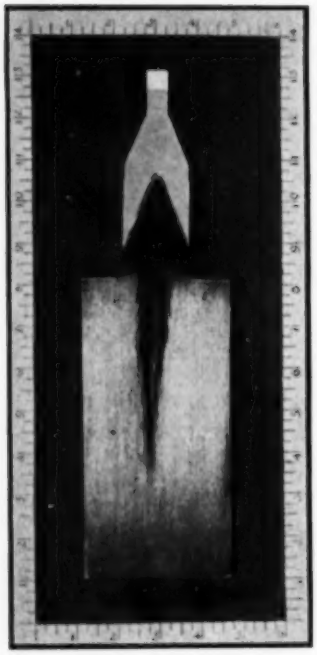

FIG. 3. Photograph of a solid steel cylinder (3.25 in. in diameter, 7 in. in length) which has been shot and then sawed in half to show the nature of the hole produced. A cross-sectioned replica of the charge that produced this hole is shown in the position that the real charge occupied before it was detonated. The real charge contained 0.25 lb. of Pentolite. The cavity liner was a steel cone (0.025 in. thick, 1.63-in. base diameter).

FIG. 4. Photograph of a solid lead cylinder (4 in. in diameter, 9.5 in. in length) which has been treated the same as the steel cylinder in Fig. 3. The steel slug from the liner can be seen embedded in the lead about 5 in. from the bottom of the cylinder.

which they have been used. Consequently, further discussion will be confined to charges with these two shapes of liners. Since most of the reliable data have been obtained with cone-lined charges similar to that shown in Fig. 2, much of the following discussion applies only to them.

The basic principles in the phenomenon[5] are fairly simple. The mechanism of cone collapse and the resulting formation of high speed jets have been revealed independently in the United States, England, and Germany by means of high speed radiographs[6] made of charges during the explosion process. Referring to Fig. 2, the detonation of the booster starts an explosive wave down the charge. When this wave reaches the apex of the thin-walled steel cone it suddenly produces very high pressures on the outside of this cone that cause its walls to collapse. The forces are so great that the strength of the steel has a negligible effect on the process, and the steel can be treated as though it were a perfect fluid. The explosive pressures on the outside cause the thin walls of the cone to move inward nearly perpendicular to their surfaces at high velocities. The moving steel retains a conical shape with the apex moving to the right along the axis. To the left behind the moving apex is found a section of thoroughly collapsed cone which contains metal only from the outer part of the cone. The inner part of the cone forms a jet which is squeezed out from the inner apex of the lining and travels at high speeds along the axis, to the right in Fig. 2. In other words, the metal in the cone lining divides into two parts with the dividing surface between these two parts being a cone lying somewhere between the inner and outer surfaces of the original hollow cone. The metal from the outer cone forms into a slug that travels to the right in Fig. 2 at relatively slow speeds (500 to 1000 meters/sec.). The metal from the inner cone forms into a jet that

[5] Much pioneer work toward understanding this phenomenon was done by W. M. Evans and A. R. Ubbelohde under the auspices of the British Ministry of Supply.

[6] The clearest and most revealing photographs the writers have seen were taken by L. B. Seely and J. C. Clark at the Aberdeen Ballistics Research Laboratory; the earliest photographs were taken by J. L. Tuck in England.

travels to the right along the axis at very high speeds (2000 to 10,000 meters/sec.). It is this jet that is solely responsible for producing the deep holes like those shown in Figs. 3 to 6. Originally it was thought by many that the slugs were responsible for most of the effect, but high speed moving-film studies of the process revealed the true nature of the effect. Further proof was furnished by the fact that slugs frequently lodged in the middle of thick steel plates that had been perforated by jets. Some of the surprising effects that can be produced by these charges are shown in the photographs in Figs. 3 to 6 inclusive.

Figure 3 is a photograph of a solid steel cylinder cut in two to show the effect produced by a charge like that shown in Fig. 2. A replica has been mounted in the position the charge occupied before it was detonated.

Figure 4 is a photograph of a solid lead cylinder that has been treated the same as the steel cylinder in Fig. 3. The hole is wider and deeper in the lead since, because of its low strength, the plastic flow continued longer.

Figure 5 is a photograph of a stack of plates, alternately steel and lead, that has been cut in two to show the effect produced in such a combination by a charge like that in Fig. 2. A replica has been mounted in the position occupied by the charge before it was detonated. This provides a very striking demonstration of the fact that the radial plastic flow produced by the jet is arrested more quickly in materials having high yield strength (like steel) than in those having low yield strength (like lead). The jet that made these holes was not over 2 mm in diameter, as flash radiographs have shown. Even the holes in the steel plates have much larger diameters than the jets that produced them.

Before these flash radiographic studies gave direct information concerning the dimensions of the jet, some interesting experiments were carried out which showed conclusively that the jet must be much smaller than the holes it produced. In these experiments the jet from a shaped charge was aimed at the standard target through a hole drilled in a steel plate. Although the hole produced in the steel target was almost an inch in diameter, the predrilled hole through which the jet had to pass before striking the target could be made as small as $\frac{1}{4}$ in. in diameter, without adversely affecting the penetration in the target and without scoring the sides of the hole. It was suspected that the jet actually had a true diameter considerably less than $\frac{1}{4}$ in., since the jet was known to have an appreciable amount of directional "wobble" which would increase its apparent diameter.

Figure 6 is a photograph of a disk of lead (2 in. thick and 12 in. in diameter) showing the large hole made by a hollow-charge jet that passed through it. The slug, which was much slower than the jet, has been captured by the disk. This disk was 18 in. from the exploding charge, and this accounts for the large distance between the holes made by the slug and the jet. Lack of symmetry in the original charge often causes the slug and jet to travel in slightly different directions.

Figure 7 shows, for comparison, the effect produced on a steel cylinder by detonating on its surface one of these charges with the liner removed. While lined cavity charges produce

FIG. 5. Photograph of a stack of plates treated like the cylinders of Figs. 3 and 4. The plates are alternately steel and lead; the top plate is steel, the next is lead, the third is steel, etc. All of these plates were originally the same size (4 in.×4 in.×0.5 in.). This provides an excellent demonstration that targets retain radial momentum for a short time after the jet has passed through them.

FIG. 6. Photograph of a disk of lead (8 in. diameter, 2 in. thick) which was placed 18 in. from a charge like that in Fig. 3). When this charge exploded, the jet made the hole near the bottom. The slug is embedded near the top of the picture. Obviously the slug and jet often do not travel the same path.

their deepest penetrations when they are placed a short distance away from the target surface, the unlined cavity charges produce their deepest penetrations when they are placed in direct contact with the target.

Figure 8 shows the effect produced by an ordinary charge with no cavity. This charge obviously contained more explosive than the others, since it had the same dimensions but contained no cavity.

These phenomena can be readily understood by applying some very simple theoretical considerations which will now be presented.

THEORY OF JET FORMATION WITH CONICAL AND WEDGE-SHAPED LINERS

An elementary mathematical discussion can be given of the formation of jets from conical and wedge-shaped liners. Consider a charge having a cross section as shown in Fig. 9. In the conical case the charge is obtained by rotating the cross section about the dashed axis of symmetry. The wedge-shaped case is obtained by supposing the cross section to be the same for an indefinite distance perpendicular to the cross section—or, equivalently, to be confined between rigid walls at both ends. We first consider the case of a wedge.

The mechanism of liner collapse is illustrated in Fig. 10. Starting from the booster a detona-

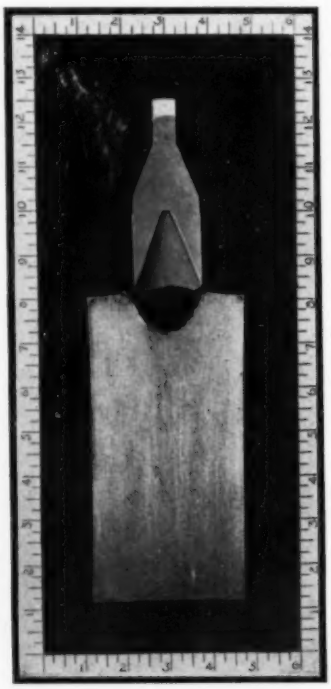

FIG. 7. Photograph of a steel cylinder, like that in Fig. 3, cut in half after being shot with a charge from which the steel cone had been removed. This unlined charge was detonated in contact with the cylinder because it produces its deepest holes at zero standoff, whereas lined charges produce their deepest holes at a larger standoff.

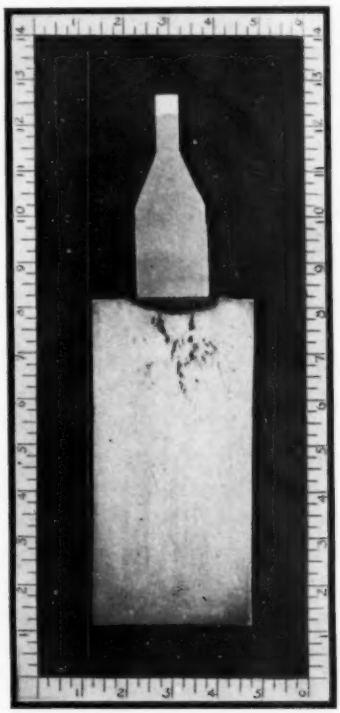

FIG. 8. Photograph of a steel cylinder that has been cut in half after being blasted by a solid charge. This charge contained more explosive than the others, since it was cast in the same mold without a cavity.

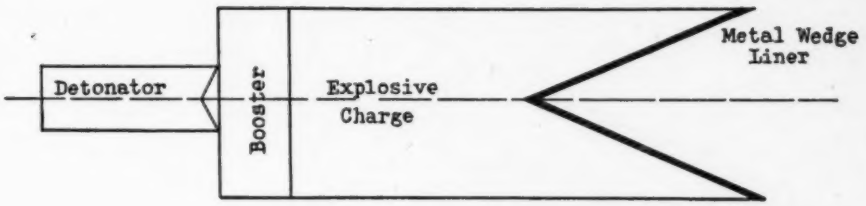

FIG. 9. Hollow charge with wedge-shaped liner ready to be set off with an electric detonator.

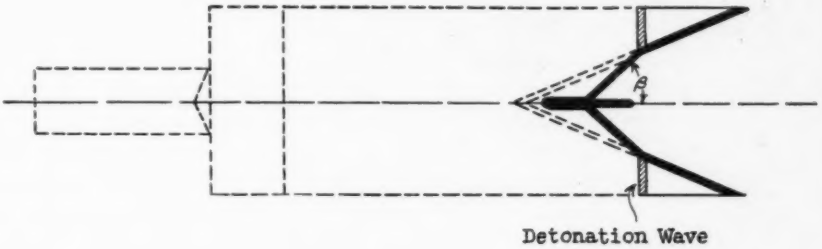

FIG. 10. Hollow charge with wedge-shaped liner in the process of exploding. Detonation wave which was started by the detonator and booster has passed over most of the liner which is in the process of collapsing.

tion wave has traveled to the right in the figure and is in the process of collapsing the liner. This wave has produced pressures so great that the strength of the liner may be neglected and the material may be treated as a non-viscous fluid. We assume that, after the walls have received an original impulse from the detonation wave, the pressure on all sides of the liner quickly equalizes and the walls continue to collapse inward with no appreciable change in velocity. Because of the finite time required for the wave to travel from the apex of the liner to the base, the angle 2β between the moving walls is larger than that between the walls of the original liner.

Actually the effect of the detonation pressures acting for a very short distance is to give the liner a velocity V_0 which bisects the angle between the perpendicular to the original liner surface, and the perpendicular to the collapsing liner surface.[7]

The walls of the collapsing liner are two planes moving inward, as shown in Fig. 11. From Fig. 12 the junction of these planes around A moves to B with a velocity

$$V_1=[V_0\cos\tfrac{1}{2}(\beta-\alpha)/\sin\beta].$$

A moving observer stationed at this moving junction would find any point P in the upper plane moving with a velocity equal to the vector difference between the velocity of the walls and the velocity of the junction. Thus he would see the point P coming toward him with a velocity

$$V_2=[V_0\cos\tfrac{1}{2}(\beta-\alpha)/\tan\beta]+V_0\sin\tfrac{1}{2}(\beta-\alpha).$$

Furthermore, as shown qualitatively by x-ray pictures and as shown in Fig. 13, he will see a "jet" moving off to the right and a "slug" moving to the left.

We now come to the crucial point of the discussion. As viewed by our observer, *the whole process appears to be unchanged by the lapse of time.* In hydrodynamical language[8] it appears to be a "steady motion" from which it follows that we can use Bernoulli's equation

$$\int dp/\rho(p)+\tfrac{1}{2}U^2=\text{const.} \qquad (1)$$

[7] To show that V_0 bisects the angle APP' in Fig. 12, consider a coordinate system having a constant velocity such that the origin moves from P to P' in unit time. In these coordinates a steady-state condition exists in the region of the origin, with the liner flowing in along $P'P$, following a curved path and flowing out along PA. The curved path is caused by pressures on the liner from the detonation wave which have a constant distribution in these moving coordinates. The velocity of the liner passing through this region changes its direction but not its magnitude, since the pressure forces are everywhere perpendicular to the motion.

Let $P'P$ and $P'B$ (parallel to PA) represent, respectively, the entering and emerging velocities of the liner in the moving system. These are equal in magnitude. Since the velocity of the moving system is PP' the velocity of the collapsing liner in the stationary system is the vector sum $PP'+P'B=PB=V_0$. Also, since the triangle BPP' is isosceles and since $P'B$ is parallel to PA, angle BPP' = angle PBP' = angle BPA. Therefore V_0 bisects the angle APP'.

[8] L. L. Milne-Thompson, *Theoretical Hydrodynamics* (Macmillan and Company, Ltd., London, 1938). For Bernoulli's theorem see p. 10, 14; for free streamlines and jets, Chap. XI, expecially paragraph 11.43, where a discussion of two-dimensional jets is given, including a differential equation for the flow pattern.

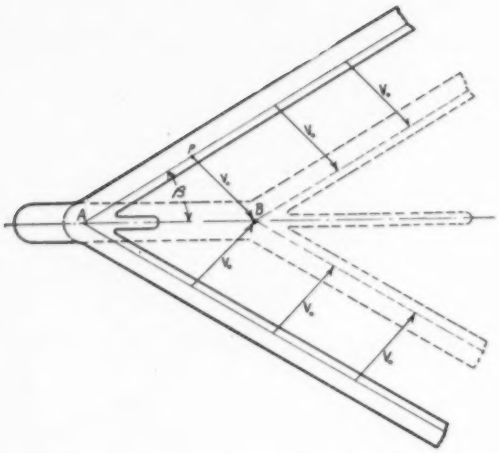

FIG. 11. Formation of jet and slug from a cone or wedge-shaped liner whose sides collapse with constant velocity V_0 as a result of the explosion of a charge that was in contact with the outer surface. The solid lines show conditions at an early instant of time, and the dotted lines show conditions after the walls have moved a distance equal to the velocity V_0.

relating the pressure p and the velocity U. If the liner is nearly incompressible so that $\rho=\rho_0$ is constant, this reduces to the simpler and more familiar equation

$$p+\tfrac{1}{2}\rho_0 U^2=\text{const.} \qquad (1')$$

In either case the pressure at any point in the fluid determines the velocity of the fluid at that point. Assume that the liner moves away from the exploded gases so fast that the pressure on its surface is very low and hence the pressures are constant on all of the surfaces of the collapsing liner. This is a well-known situation, and the boundary streamlines at constant pressure (hence velocity) are called "free streamlines." Hence, as viewed by the observer, the jet and slug will appear to recede with exactly the same speed, V_2, as the walls appear to approach; this is shown in Fig. 13. In particular, during collapse *the jet and slug will have exactly the same length*. This is observed experimentally.

Going back to the stationary system of coordinates, it is seen that the forward jet (traveling to the right in Fig. 13) has a velocity given by

$$V=V_1+V_2,$$

while the backward jet or "slug" (traveling to the left in the moving system of Fig. 13) actually has a small velocity to the right given by

$$V_s=V_1-V_2.$$

It may help to visualize the process to consider that: if the point P (fixed in the upper plane) (Fig. 11) travels to point B (fixed in space) in unit time, the material from the inner surface of the upper plane included between PA and AB moves into the jet, and the front of the jet moves to the right a distance equal to $PA+AB$ in the same time. Thus this material forms the very high velocity jet that is responsible for the deep penetrations. Its velocity is

$$V=V_0\left\{\frac{\cos\tfrac{1}{2}(\beta-\alpha)}{\sin\beta}+\frac{\cos\tfrac{1}{2}(\beta-\alpha)}{\tan\beta}+\sin\tfrac{1}{2}(\beta-\alpha)\right\}. \qquad (2)$$

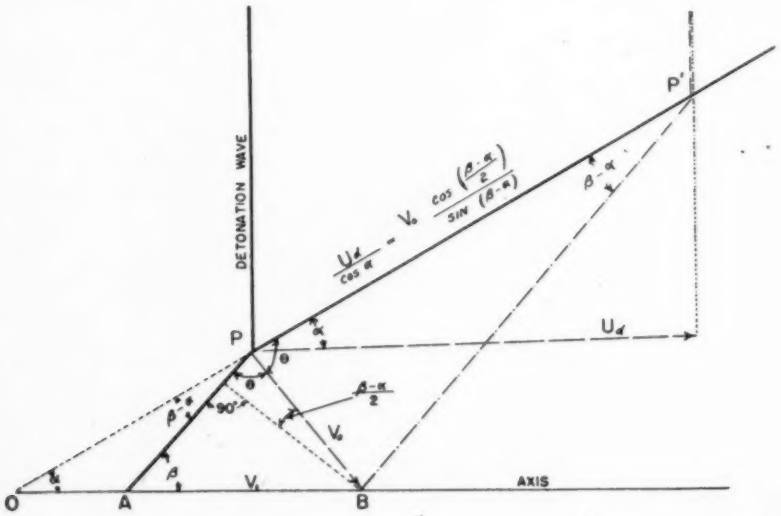

FIG. 12. Geometry of the collapse process. OPP' is the upper half of the original cone or wedge. AP, the collapsing section, is moving with a velocity V_0, whose direction bisects the angle APP'. The detonation wave (velocity U_d) will move from P to P' in unit time at which time $P'B$ will become the collapsing section. The junction A will move to B in unit time at a velocity

$$V_1=V_0(\sin\theta/\sin\beta)=V_0[\cos\tfrac{1}{2}(\beta-\alpha)/\sin\beta],$$

since $\theta=90°-\frac{1}{2}(\beta-\alpha)$.

The material from the outer surface of each plane forms a slug and moves with the relatively low velocity

$$V_s = V_0\left\{\frac{\cos\frac{1}{2}(\beta-\alpha)}{\sin\beta}-\frac{\cos\frac{1}{2}(\beta-\alpha)}{\tan\beta}\right.$$
$$\left.-\sin\tfrac{1}{2}(\beta-\alpha)\right\}. \quad (3)$$

The principle of the conservation of momentum determines the manner with which the material of the collapsing planes divides between the jet and the slug. Let m be the total mass per unit length of the two collapsing planes approaching the junction. Let m_j be that part of m going into the jet and m_s be that going into the slug. Then $m=m_j+m_s$. Equating the horizontal components of momentum before to those after passing the junction A in the moving coordinate system of Fig. 13,

$$\begin{aligned} mV_2\cos\beta &= m_sV_2-m_jV_2,\\ m_j &= m/2(1-\cos\beta),\\ m_s &= m/2(1+\cos\beta). \end{aligned} \quad (4)$$

According to this simple picture, the velocities of the jet and slug and their cross-sectional thickness are constant.

The case of a conical liner may be treated in the same way. However, in this case the walls converge on the axis from all sides. The moving observer must travel at the same rate as in the case of the wedge. However, in order for the process to appear stationary to him the total mass per unit distance along the axis must be constant. This is only approximately true in the case of a liner of constant thickness; to be exactly true, the liner thickness would have to be inversely proportional to the distance from the apex.

In the case of a plane detonation wave traveling parallel to the axis with constant speed U_d, we can even compute V_0 from the fundamental relation

$$\frac{U_d}{\cos\alpha}=\frac{V_0\cos\frac{1}{2}(\beta-\alpha)}{\sin(\beta-\alpha)},$$

which follows by pure geometry from Fig. 12.

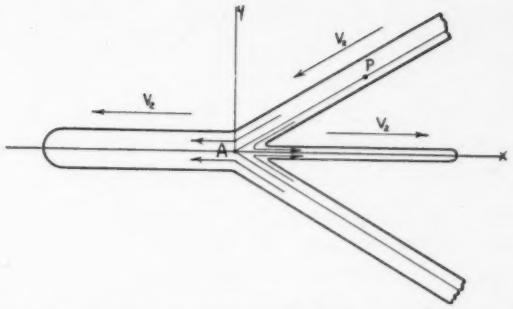

FIG. 13. Formation of jet and slug by a cone or wedge-shaped liner shown in Fig. 11 from the point of view of an observer stationed at the moving junction A.

This replaces formulas (2)–(3) by

$$V=U_d\frac{\sin(\beta-\alpha)}{\cos\alpha}\{\csc\beta+\operatorname{ctn}\beta+\tan\tfrac{1}{2}(\beta-\alpha)\}, \quad (2')$$

$$V_s=U_d\frac{\sin(\beta-\alpha)}{\cos\alpha}\{\csc\beta-\operatorname{ctn}\beta-\tan\tfrac{1}{2}(\beta-\alpha)\}. \quad (3')$$

The jet velocity increases as the angle α decreases, since β also decreases. With such a detonation wave the velocity approaches a maximum as α approaches zero. From Eq. (2′)

$$V=2U_d \quad \text{when} \quad \alpha=0,$$

and *the jet velocity cannot exceed twice the detonation velocity.*

In the hypothetical case of a conical wave front, moving perpendicular to the surface of a conical liner so that it strikes all surfaces at the same instant, $\beta=\alpha$ and the velocities of the jet and slug from Eqs. (2)–(3) take the simple form

$$V=(V_0/\sin\alpha)(1+\cos\alpha),$$
$$V_s=(V_0/\sin\alpha)(1-\cos\alpha).$$

With wave fronts of this sort *the velocity of the jet could be increased indefinitely by decreasing the cone angle.* However, as α tends to zero, the mass of the jet $\{m_j=m/2(1-\cos\alpha)\}$ and the momentum of the jet $\{m_jV=(mV_0/2)\sin\alpha\}$ both tend to zero.

To sum up, our mathematical theory predicts jet and slug velocities as in (2)–(3), (2′)–(3′), and masses as in (4) both for conical and wedge-shaped liners.

COMPARISON WITH EXPERIMENT; FURTHER REMARKS

The preceding theoretical predictions are in rough agreement with observation but with im-

portant exceptions. According to flash radiographs, the collapse angle 2β is greater than the original cone angle and is approximately constant throughout the collapse process, which is in complete agreement with the theory. Further, these same radiographs, as well as some rotating drum camera measurements, show that the speeds of the front of the jet and of the slug are close to those predicted by Eqs. (2) and (3), respectively, but, contrary to prediction, the speed of the back, or last formed part of the jet, is considerably slower than that of the front. Also, contrary to predictions, an "afterjet" continues to be emitted after the walls have completely collapsed.

Since the collapse angle 2β has been approximately determined by flash radiography, Eqs. (4) can be checked experimentally if either the slug or the jet can be recovered after the explosion. While both can be recovered, it is fortunate that recovery of the slug is the easiest, since it can be made to yield more detailed information.

While charges bearing wedge-shaped liners do not give slugs that survive the detonation process and subsequent battering, charges bearing cone-shaped linings with apex angles 60° or less do. These slugs have been recovered virtually undamaged by firing the charge into sawdust or water. They have been found to contain a smaller fraction of the original mass of the cone liner than Eqs. (4) predict. This is not surprising, since even qualitative inspection of the slug shows that the ideal collapse process, postulated in obtaining Eqs. (4), has not continued all the way to the base. If, before loading and firing the charge, the cone is sectioned by a series of cuts in planes parallel to the base, normal jet formation and performance is obtained. Each section of the cone forms a corresponding portion of the slug. These portions, which were recovered as separate pieces, could be fitted together to form a normal appearing slug. By weighing each section before and after firing the contribution of each part of the cone to the jet, and to the slug, was determined. It was found that for the upper part of the cone the contributions to jet and slug agree with the values calculated from Eqs. (4) within the experimental uncertainty in the radiographic determination of β. The percentage loss in weight increased, however, for the lower portions of the cone. This greater weight loss may be due in part to imperfect cone collapse near the base and the breaking off of some metal. Some of the increased loss, however, is certainly due to the formation of an additional length of jet from the slug after collapse is complete. This late formation of jet from the slug is clearly shown in the flash radiographs, and its existence is also indicated by the weight-loss relations. There has been considerable discussion as to why jet formation should continue for some time after collapse is complete.

It may be that a pressure wave in the exploded gases converges on the slug and squirts out the afterjet like toothpaste out of a tube. Metallurgical examinations on recovered slugs show that the material near the axes of these slugs has been heated almost to its melting point. The pressure wave which may converge on a newly formed slug is undoubtedly the same as the pressure wave which is primarily responsible for the penetrations produced by these same charges without liners. Immediately after an unlined hollow charge has been detonated the exploded gases stream into the cavity and converge onto the axis where they are formed into a high speed jet.[9] The effect produced by such a charge is shown in Fig. 7; it is the "Munroe effect" already mentioned in the first paragraph.

For such a mechanism to account for the observed velocity of the afterjet it would be necessary for the secondary pressure wave, converging on the slug, to produce much higher pressures than one should expect from a charge like that shown in Fig. 2. Some other explanation is needed.

Another possible explanation of the afterjet is that it may be pulled out by the primary jet which is continuous in the neighborhood of the slug throughout the process of its formation.

[9] Similar jets are formed under the extremely prosaic dropping of a sphere into water. An air-filled cavity at first trails the sphere, symmetric about a vertical axis through the center of the sphere. After an instant the outward motion of the walls is checked, then reversed, and the walls collide on the axis, meeting on all sides. This causes vertical jets, both upwards and downwards. Cf. A. M. Worthington, *A Study of Splash* (Longmans, Green and Company, London, 1908); also a forthcoming article by Dr. David Gilbarg of the Naval Ordnance Laboratory.

This process of ductile drawing may be compared with the formation of fibers from molten glass or quartz. Experiments carried out by Bridgman have shown that many metals become enormously more ductile when subjected to intense pressure, and it appears conceivable that this great ductility might persist for at least a few microseconds after the pressure is released. If this latter mechanism is correct, it also would account in part for the velocity gradient found to exist in the jet, since acceleration of material from the slug would result in deceleration of parts of the jet already formed. While this latter mechanism seems most probable at present, it is possible that both mechanisms play some part.

The afterjet forms especially easily because the interior or "core" of the slug is heated almost to the melting point, as has been mentioned before. This heating may be explained on the basis of the following crude two-dimensional theory of the heat caused by the working of the liner under deformation. (The time involved is too short for conduction to be important.)

Let us again introduce the steady-state coordinates of Fig. 13, and let us assume that the deformation is that of a perfect fluid.[8] Let u and v be the components of velocity, parallel, respectively, to the x and y axes, of the fluid at the point whose coordinates are (x, y). By classical hydrodynamics u and v satisfy the conjugate Cauchy-Riemann differential equations

$$\partial u/\partial x = -\partial v/\partial y = \sigma, \quad \partial v/\partial x = \partial u/\partial y = \tau$$

corresponding to zero divergence and curl. Hence the infinitesimal strain tensor[10] is described by the matrix

$$\begin{Vmatrix} 1+\sigma dt & \tau dt \\ \tau dt & 1-\sigma dt \end{Vmatrix},$$

whose characteristic roots may be computed as

$$\lambda = 1 \pm \sqrt{\sigma^2+\tau^2}\,dt = 1 \pm |d\zeta/dz|\,dt,$$

where $\zeta = u - iv$ is the conjugate velocity vector and $z = x + iy$ is the complex position vector. Hence, *the time rate of strain of a given infinitesimal element in the fluid is proportional to*

$$|d\zeta/dz|.$$

For simplicity let us assume that the *heat of deformation of this element depends only on its total strain* $\int |d\zeta/dz|\,dt$ and not on the rate of strain. Here the integral is evaluated for the element as it travels through the region near the stagnation point. Then

$$\int |d\zeta/dz| \cdot dt = \int |d\zeta/dz| \cdot |dt/dz| \cdot |dz|.$$

But $|dt/dz| = 1/|\zeta|$; hence the heat generated in each element is proportional to

$$\int |d\zeta/\zeta dz| \cdot |dz| = \int |d\zeta/\zeta| = \int |d(ln\zeta)|. \quad (5)$$

That is, *the total heat generated per unit volume is proportional to the variation in the natural logarithm of* ζ *or equivalently of the complex velocity vector* $\bar{\zeta} = u + iv$. Since the logarithm of zero is infinite, it is clear that the points near the axis of the jet, which pass nearest to the "stagnation point" of zero velocity, should be heated an indefinitely large amount. Possibly as the temperature of the liner material approaches its melting point this material acts more and more nearly like a perfect liquid, with negligible viscosity, so that its heating is greatly reduced and only a very small part may be melted.

It may also be noted that the "free streamlines" are lines of constant length; hence the principal axes of deformation are at 45° to these, and the plane of maximum shearing stress is parallel to these lines. Near the surface of the liner we therefore expect shearing rupture to be parallel to the boundary.

PENETRATION BY JETS

The process of penetration of a target material by a shaped-charge jet is much like that of a high speed jet of water from a fire hose nozzle penetrating a bank of soft mud. Target material is splashed out at high velocities radially from the point of impact. The diameter of the hole produced is considerably greater than, and is not directly related to, the diameter of the jet, but is more closely related to the energy delivered by the jet per unit depth of penetration.[11] As shown in Figs. 3–5, the hole diameters

[10] I. S. Sokolnikoff, *Mathematical Theory of Elasticity* (McGraw-Hill Book Company, New York, 1946), Chapter I.

[11] Felix Hélie, *Traite de balistique experimentale* (Dumaine, Paris, 1840), where an experimental law of direct proportionality between impact energy and hole (or crater) volume is asserted.

are smaller in hard materials than in soft, since more work must be done to open the hole in the harder materials. In soft materials, like lead, large diameter holes are produced because the radial momentum of the target material spreads it outward until it can be stopped by elastic or viscous forces.

On the other hand, with most charges the rate of penetration and the depth of penetration into most target materials are nearly independent of the strength of the target material. This arises from the fact that because of the high velocities of shaped-charge jets the pressures produced at the point of impact are far above the yield point of most materials. To a first approximation the strengths and viscosities of target materials can be neglected, and the problem can be treated by hydrodynamics.[12]

PENETRATION WITH CONSTANT JETS

Consider a jet as shown in Fig. 14a having a constant length, l, velocity, V, and density, ρ_j, penetrating a semi-infinite target of density, ρ, with a velocity, U, as shown in Fig. 14b. Consider the case in which U has reached a constant value.

FIG. 14a. Idealized jet of length l, velocity V density ρ_j, and cross-sectional area A.

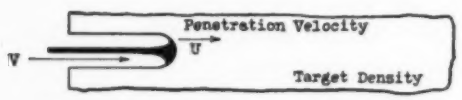

FIG. 14b. Idealized jet penetrating target material of density ρ, with a velocity U. Inasmuch as it is a continuous jet, it spreads out as it reaches the target.

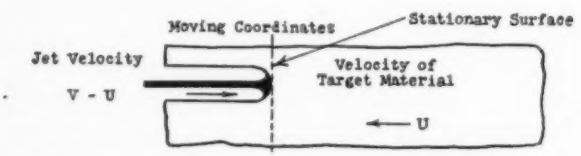

FIG. 14c. The steady state in (b) transferred to a coordinate system moving at the penetration velocity U. In this moving system the hole contour is fixed.

[12] The theory presented in the next section was discovered independently by R. Hill, N. F. Mott, and D. C. Pack in England; earlier similar semiquantitative ideas had been advanced by Kistiakowsky, Messerly, and one of us.

The phenomenon is simplest when viewed in a system of coordinates moving with a velocity U, as shown in Fig. 14c. In this system the hole profile is fixed, and the jet moves to the right at a velocity $V-U$ while the target moves to the left at a velocity U. If the pressure produced by the jet is large compared to the strengths of both the target and the jet material, they can be treated like perfect fluids. The pressure on the two sides of the surface of contact between the jet and the target must be the same. Hence, by Bernoulli's theorem which is valid since the phenomenon is stationary in the coordinates we have chosen,

$$\tfrac{1}{2}\rho_j(V-U)^2=\tfrac{1}{2}\rho U^2. \tag{6}$$

The velocity U has been measured for a number of charges and target materials. Using charges like that in Fig. 2, the velocity U in steel targets has been observed to be as high as 2.7×10^5 cm/sec. In these cases the pressure produced by the jet is $\frac{1}{2}\rho U^2=0.5\times7.8(2.7\times10^5)^2=2.8\times10^{11}$ dynes/cm^2 or 0.28-million atmospheres. Since this is far above the yield strength of any steel, the treating of steel as a perfect fluid is justifiable.

The mechanism of penetration is illustrated in Fig. 14, which shows the jet being used up by impinging on the target. If it is assumed that the steady state is reached almost instantaneously and that the penetration stops[13] as soon as the last jet particle has struck the target, then the total penetration P is equal to

$$P=Ut_f=Ul/(V-U)=l(\rho_j/\rho)^{\frac{1}{2}} \tag{7}$$

from Eq. (6), where l is the original length of the jet and t_f is the time of penetration.

This is a surprising result. It indicates that the depth of penetration into a massive target depends only on the length and density of the jet and the density of the target but not upon the jet velocity. The lack of dependence on jet velocity is at first most surprising. However, one need only notice that although from Eq. (6) the velocity of penetration U is proportional to

[13] It is probable that after the last jet particle strikes a relatively soft target material it will have sufficient residual momentum to open up the hole still deeper. This effect has been called "secondary penetration" to distinguish it from that given by Eq. (7). It helps to explain why deeper holes are produced in massive lead targets than in massive steel targets even though the lead targets have the higher densities.

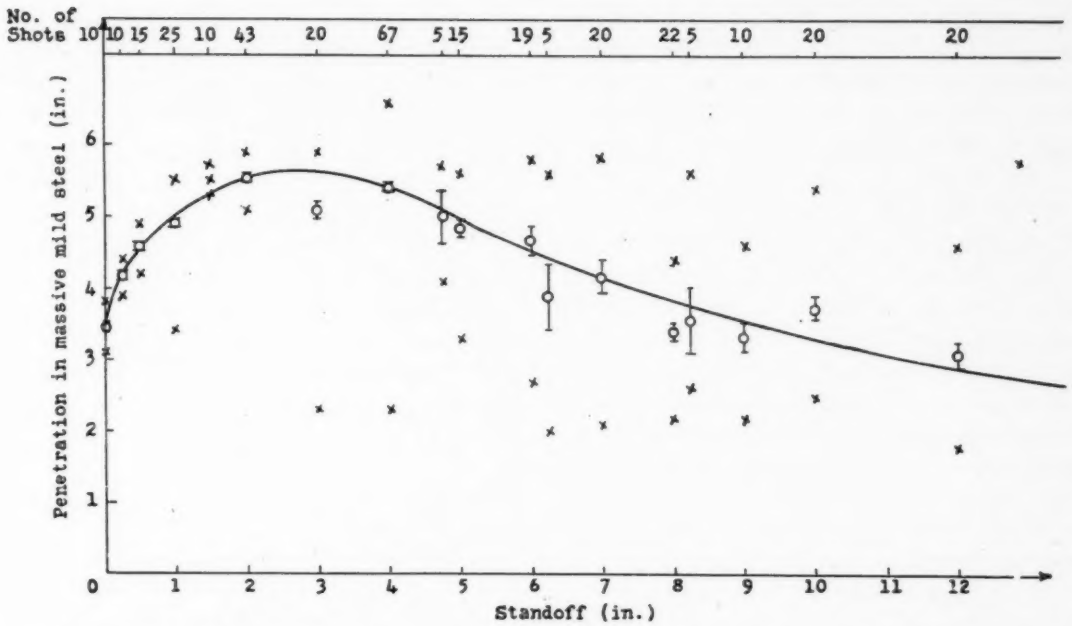

FIG. 15. Curves of average penetration into mild steel as a function of standoff for CIT standard charge. $\bar{\times}$ indicates average penetration with the average deviation of the mean. $\times$ indicates the maximum and the minimum penetrations.

the jet velocity V, the rate at which the jet is used up is also proportional to V. Thus a faster jet is used up in a shorter time, and the total penetration remains the same. Of course, this independence of the depth of penetration on the jet velocity can hold only for velocities great enough to produce pressures far above the yield strength[14] of the target materials.

Equation (7) indicates that the depth of penetration by a given charge should be inversely proportional to the square root of the density of that target. This is roughly true in many cases, though there are a number of exceptions[14] indicating that this simple model needs to be modified.

Though this theory correctly predicts a number of experimental phenomena, there are many experiments that show the inadequacy of this simple jet model. The average penetration into a given target at first increases and then decreases as the distance (standoff) between the charge and the target is increased. This phenomenon is illustrated (Fig. 15) by the shots into a massive mild-steel target with the charge shown in Fig. 2.

A number of tests have been conducted in which the massive mild-steel target was part of a ballistic pendulum so that the momentum of the jet could be measured simultaneously with the penetration it produced. These experiments showed that while the average penetration varied greatly with standoff, the average momentum was almost constant independent of standoff. This result agrees well with present theory, which indicates that the penetration should be independent of the velocity of the jet. Further confirmation of this point is found in Fig. 16, where the individual momentums of jets at a given standoff are plotted against the penetration they produced at this same standoff. The variations in momentums are smaller than those in penetrations, but the two variations show absolutely no correlation. Jets having the largest momentums did not produce the deepest penetrations.

If the material in the jet is broken up into very fine particles which are sufficiently separated so

[14] In jets from conical liners a small amount of jet material at the rear of each jet travels slow enough to produce stresses lower than the yield strength in armor though higher than the yield strength in mild steel. Thus the penetration process may continue longer in mild steel than in armor. This phenomenon, together with the phenomenon of secondary penetration[13] accounts for the fact that the total penetration into steel armor is a little less than the total penetration into mild steel and that the penetration into lead is greater than the total penetration into either of the steels.

that they do not interfere with each other, the pressure produced by the jet will be greater than that indicated by Bernoulli's theorem in Eq. (6). This follows from the fact that a particle jet does not spread out over so large an area as a continuous one. The continuous jet is capable of supporting internal pressure, whereas the particle jet is not. This ability to support internal pressure produces a gradient in pressure along the axis of the jet with the highest pressure at the point of impact with the target and reducing down to zero in the unaffected part of the jet. The gradient in the pressure causes a gradient of the opposite sign in the velocities within the jet from U at the point of impact with the target to V in the unaffected part. Since with a jet under steady-state conditions the product velocity times cross-sectional area must be the same at all points, the gradient in the velocity causes the cross-sectional area of the jet to increase as it approaches the target.

With a particle jet of the kind assumed, the particles retain their velocity and area until they make inelastic impacts with the target surface and no such spreading takes place. The pressure produced by a particle jet can be calculated approximately by dividing the total force required to effect the change in momentum of the jet by the total area A the jet strikes. The total force is given by the rate of change of momentum $\rho_j A(V-U)^2$, and so the average pressure on the surface is $\rho_j(V-U)^2$. If this pressure is set equal to the pressure in the target material at the point of impact, as given by Bernoulli's equation (1′), we get

$$\rho_j(V-U)^2=\tfrac{1}{2}\rho U^2. \tag{8}$$

This equation differs from (6) only by the factor $\frac{1}{2}$ on the left side of the equation. The two Eqs. (6) and (8) can be combined into one

$$\lambda\rho_j(V-U)^2=\rho U^2, \tag{9}$$

where λ is a constant that equals one for continuous jets and two for dispersed particle jets.

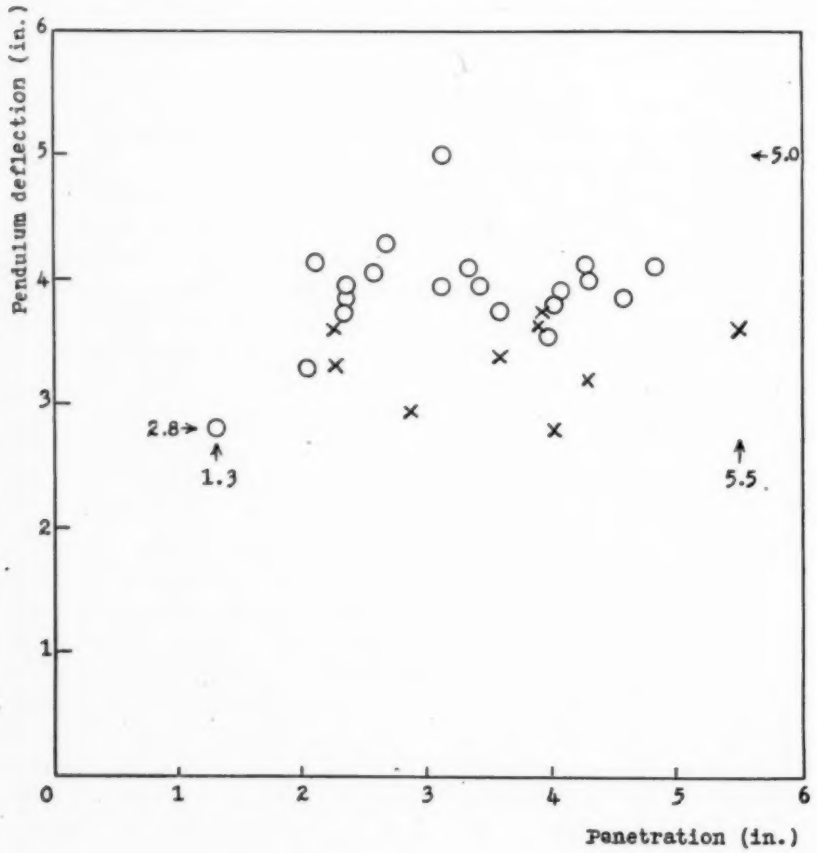

FIG. 16. Ballistic pendulum deflections *versus* penetrations into mild steel for standard charges at 12-in. standoff. The circles represent data obtained from one batch of charges, while the crosses represent data obtained from another batch. These charges were made to be identical, and no variations were observed before detonation. The second batch of charges gave nearly the same average penetrations as the first, even though their average jet momentums were lower.

If a jet is intermediate between these two types, λ may take values between one and two.

From Eq. (9) the penetration produced by either type of jet can be calculated

$$P = l(\lambda \rho_j / \rho)^{\frac{1}{2}}. \tag{10}$$

This equation should hold only for idealized jets whose properties remain constant throughout the penetration process. Real jets show a more complex behavior which will now be discussed.

PENETRATION WITH VARIABLE JETS

Jets from conical liners are not constant but change character as they travel. For these jets Eq. (10) must be modified. As mentioned earlier, the jet velocity decreases continually from the front to the rear; hence the jet becomes longer and longer. The increasing length produces other changes in jet characteristics that must be considered. Furthermore, jets do not have the same properties throughout their length at any given time, and they are usually not completely formed at the time they start penetrating a target. This last raises the question as to whether or not the target may react upon the jet to change its characteristics while it is being formed.

Such a reaction of the target upon the formation of the jet cannot take place if the velocity of sound in the jet material is low enough so that any pressure pulse produced by the target cannot travel back to the neighborhood of the stagnation point (Fig. 11) in the jet being formed. This condition is generally realized even at low standoffs, since the velocities in the front part of the jet are higher, and those at the rear are not much lower than the velocity of sound in the jet material. With charges like that in Fig. 2, the conditions are such that no effect upon the formation of the jets can be expected from steel targets that are no closer to the charge than $\frac{1}{2}$ inch. This is fortunate, for it makes it possible to divorce the process of penetration by jets from the process of formation of the jets.

To calculate the penetration of a jet into a target one needs to know its physical characteristics at all points in the jet and at every instant of time. The true conditions are undoubtedly very complex. However, in calculating the penetration attributable to a jet, we need only concern ourselves with the average density, ρ_j, and state of dispersion, characterized by λ, of that part of the jet that is about to strike the target at the given instant of time. The average density, ρ_j, is defined as the mass in a small section of the jet divided by the over-all volume of that section. It will be considered equal to the density of the liner material in continuous jets and lower than that in particle jets. The factor λ will be considered as a function of ρ_j, although it may also vary somewhat with the size of the particles into which the jet is broken: *Let us assume that the ρ_j and λ, of that part of the jet from a given charge that is striking the target at the given instant, are independent of time and depend only upon the distance from the base of the original cone to the point where the jet is striking the target.*

While this assumption is made because it greatly simplifies the calculations, it is probably close to the truth as any other simple assumption that could be made. If we neglect the relatively small compressibility of the metal in the liner, all parts of the jet from a given charge must leave the stagnation point (Fig. 11) with the same density. If the jet breaks into particles because it has a large velocity gradient, it is probable that the front breaks up first and the rear later, and thus the breaking may take place at approximately the same position in space for all parts of the jet. The subsequent reduction in density of the jet produced by spreading of the particles due to the velocity gradient and other causes is probably dependent more upon the distance that particular section of the jet has traveled from its point of formation than upon its position in the jet or upon the time since the process started.

It should be noticed that, while the theory of formation of jets from conical liners of uniform thickness indicates that the rear of each jet should have more mass per unit length than the front, there is no reason to suppose that the densities at these points will be different. The jet cross section is probably larger at the rear than at the front, but this should not affect the depth of penetration, though it should affect the diameter of the hole produced.

With this assumption, since λ depends upon ρ_j, the ρ_j and the λ of that part of the jet from a given charge that is striking the target depend

upon the distance x from the cone base but not upon the time t.

The penetration is given by

$$P=\int U dt,$$

where the integral is evaluated over the time of penetration. Now $dl=(V-U)dt$, where dl is the small element of the jet that will strike the target and thus be removed from the jet in the next instant of time dt. Hence, neglecting transient effects like that mentioned in footnote thirteen,

$$P=\int U dl/(V-U) \tag{11}$$

integrated over the total length of the jet as it strikes the target. Assuming that Eq. (9) holds approximately for variable jets, Eq. (11) may be written

$$P=\int (\lambda\rho_j/\rho)^{\frac{1}{2}} dl, \tag{12}$$

or

$$P=1/(\rho)^{\frac{1}{2}}\int (\lambda\rho_j)^{\frac{1}{2}} dl, \tag{13}$$

if the target is of constant density. The integral in Eq. (13) depends primarily on the jet characteristics, so that penetrations of similar charges into different targets should be inversely proportional to the square root of the density of the target just the same as for constant jets. However, Eq. (13) predicts that the penetration into a given target by a given variable jet will depend upon the distance between the charge and the target, whereas the penetration with constant jets would be independent of this distance.

Let the standoff s be the distance between the original cone base and the surface of the target. Since the jet lengthens as it travels, the integral in Eq. (13) for a given jet depends upon s. An exact calculation of this dependence is difficult and is hardly justified, considering the uncertainty in the original assumptions. However, an excellent idea of this dependence can be obtained by the use of some approximations.

Write Eq. (13) as

$$P=\bar{J}/(\rho)^{\frac{1}{2}}\int dl,$$

where $\bar{J}$ is a kind of average value of the quantity $(\lambda\rho_j)^{\frac{1}{2}}$ during the process of penetration. Its value lies somewhere between the values of $(\lambda\rho_j)^{\frac{1}{2}}$ at the beginning and at the end of the penetration. According to our assumption that λ and ρ_j for a given charge depend on distance but not on time, $\bar{J}$ depends primarily[15] on s. The integral $\int dl$ for a given charge also depends primarily[15] on s. If the jet were of constant length, $\int dl$ would give this length, since it represents an integration of all the elementary lengths of jet as they strike the target. With a variable length jet $\int dl$ represents an effective length, for it is the sum of all of those elementary lengths of the jet that at each instant are causing the penetration. This effective length $\int dl=\bar{l}$ depends primarily upon s. Equation (13) becomes

$$P=\bar{J}\bar{l}/(\rho)^{\frac{1}{2}}. \tag{14}$$

From Eq. (14) the approximate dependence of P on s can be calculated. There are three cases to consider, all of which may occur at different stages in the same jet.

Case 1.—The jet is "drawn out" like a ductile metal and becomes narrower. The jet density ρ_j is unchanged, and, since λ is a constant equal to one for a continuous jet, P increases in direct proportion to $\bar{l}$.[16]

Case 2.—The jet is in the process of changing from the first to the second type of jet. It has broken up into particles, but the particles are still so close together that on impact with the target the jet acts almost as though it were continuous. The value of λ is intermediate between 1 and 2, but approaches 2 in an unknown manner as the jet lengthens. Thus λ increases and ρ_j decreases with standoff. Whether $\bar{J}$ (the average of $(\lambda\rho_j)^{\frac{1}{2}}$ increases, decreases, or stays constant depends upon whether λ increases faster than, slower than, or at the same rate as ρ_j decreases. Some experiments suggest that $\bar{J}$ first increases

[15] The quantity $\bar{J}$ and the integral $\int dl$ both depend very slightly upon the density ρ of the target, since a different penetration in a different density target will change the average obtained for $(\lambda\rho_j)^{\frac{1}{2}}$ as well as the value of $\int dl$. For both, the dependence upon ρ is so slight it will be neglected.

[16] The process of ductile drawing of the jet due to the velocity gradient in it was first suggested because the increase in penetration proportional to $(\bar{l})^{\frac{1}{2}}$ for particle jets of case 3 did not appear to be rapid enough to account for the experimental observations.

slightly and then decreases with increasing standoff. Probably the penetration produced is much the same as that of case 1, where J is constant and the penetration is proportional to l.

Case 3.—The jet consists of finely divided particles with unchanging cross section. The factor λ is a constant equal to 2. Since the decrease in ρ_j is caused by the lengthening of the jet due to its velocity gradient, the average value of ρ_j should be inversely proportional to l, and J should be inversely proportional to $(l)^{\frac{1}{2}}$. Thus from Eq. (14) P should be proportional to $(l)^{\frac{1}{2}}$.[16] The penetration increases with standoff, though at a slower rate than with jets of cases 1 and 2.

The nature of jets from conical liners depends upon the physical properties of the cone materials under the conditions of temperature and pressure found in the jets. Probably all metallic jets pass through each of the three stages, starting out as continuous but sooner or later breaking up into particles. The metals that are less ductile under these conditions break up into particles sooner than those that are more ductile. Thus charges with more ductile linings, like aluminum and copper, produce larger penetrations as the standoff increases than do those with less ductile linings. In each case the penetrating ability increases with the standoff of the charge from the target, rapidly at first during the ductile drawing and more slowly after the jet has broken up into particles.

It might seem that the penetrating power of these jets should increase indefinitely, but there are a number of reasons why this does not happen.

1. In practice the jets are never perfectly aligned, so they tend to spread and their effective density is reduced, thus reducing their penetrating ability.

2. The reduction in jet density caused by both lengthening and spreading eventually reduces the pressures produced in the targets until their strengths can no longer be neglected, and the simple theory breaks down.

3. At great distances the particles spread so far apart that the air resistance on the individual[17] particles becomes an important factor.

All of these tend to reduce the penetration as the standoff increases.

To sum up, the penetrating ability of jets from conical liners rises at low standoff, because of the lengthening of the jet material which is first drawn ductilely and is later broken up into particles, and falls at larger standoff, because of the reduction in jet density resulting from its spreading. Thus, when the penetration P is plotted as a function of the standoff, s, the curve rises to a maximum at the optimum standoff and then falls off again as shown in Fig. 15. It will be noticed that, although the individual points scatter widely, the average penetrations follow a fairly smooth curve. The scatter of the points is largely due to imperfect alignment in most of the charges.

THEORY OF PENETRATION

An approximate expression for the penetration as a function of the standoff s can be obtained for variable jets from Eq. (14). It is necessary to neglect any changes in velocity[18] because of forces acting upon each jet particle from the time the jet is formed to the time when the particle strikes the target.

The effective length, l, of the jet increases linearly with standoff, s, because of the gradient of velocity which is known to be approximately constant along the jet. The ratio of the effective length at standoff s to that at $s=0$ is then roughly

$$1+\alpha s,$$

where α is a constant depending upon the velocity gradient.

For particle jets the effective density $\tilde{\rho}_j$ of the jet depends upon its effective length, l, and its effective cross-sectional area. The effective cross-sectional area increases with standoff because of spreading. If there are no appreciable forces upon the jet particles, they will travel in straight lines, and the radial spreading will be linear with s. If the radial spreading is symmetrical about the axis, the ratio of the effective jet radius at

[17] Close to the charge (within 10 or 15 times the diameter of the base of the cone) air can be treated approximately like any other target having the same density. The front of the jet creates a very intense shock wave with an evacuated space behind it which reduces the air resistance on the rest of the particles in the jet to a negligible quantity.

[18] This approximation is not serious because the forces acting upon the jet particles in this period are relatively small. The internal forces acting during the ductile drawing process change the velocities somewhat but not enough to seriously affect the rate at which the length of the jet changes, which is the quantity that now concerns us.

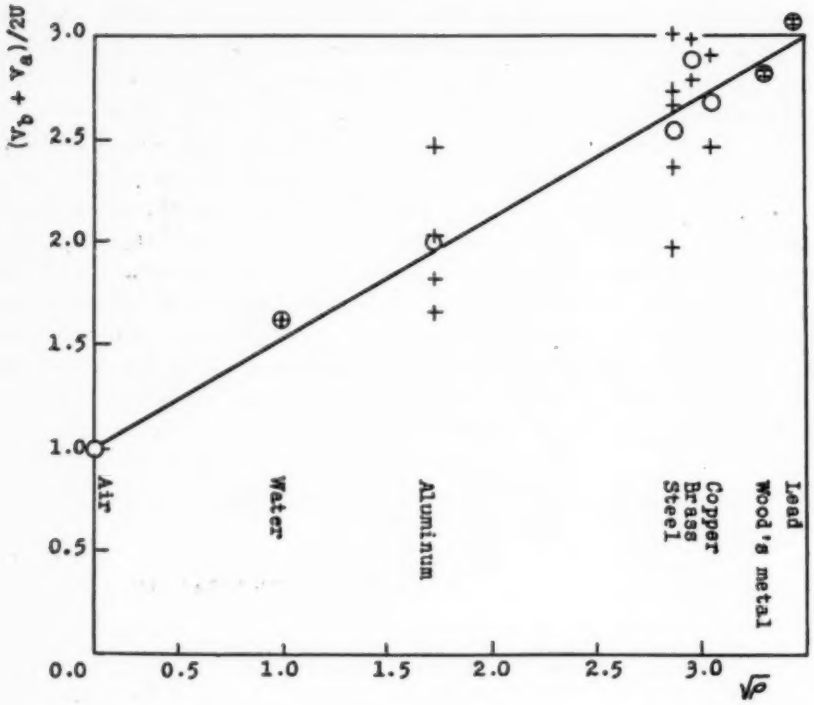

FIG. 17. The ratio for standard charges of the average jet velocity to the average penetration velocity in materials of different densities. The crosses indicate individual shots while the circles indicate the averages for each material.

standoff s to that at $s=0$ is roughly

$$1+\beta s,$$

where β is a constant that determines the rate of spreading. The ratio of the effective cross-sectional area at standoff s to that at $s=0$ is

$$(1+\beta s)^2$$

if the spreading is symmetrical. If the spreading is somewhat non-symmetrical, this relation holds less exactly.

Although the actual jet density is constant in the continuous jet of case 1, the effective jet density may decrease with standoff because of waver caused by faulty alignment. For lack of better information we may assume that the continuous jets waver through the same solid angle as the particle jets spread. The ratio of effective jet density due to spreading or wavering at standoff s to that at $s=0$ is roughly

$$1/(1+\beta s)^2.$$

The penetration of these jets can then be obtained approximately from Eq. (14). For cases 1 and 2

$$P=P_0(1+\alpha s)/(1+\beta s), \qquad (15)$$

where P_0 is the penetration at $s=0$.

For particle jets of case 3, for which $\lambda=2$, the penetration is approximately

$$P=P_0'(\sqrt{2}(1+\alpha s)^{\frac{1}{2}}/1+\beta s), \qquad (16)$$

where P_0' is the value for P from Eq. (15) at the value of $s=s_1$ where the jet breaks into particles. Generally each jet passes through the stages described by case 1, case 2, and case 3 in that succession.

Curves of penetration *versus* standoff can be fitted very well with Eqs. (15) and (16), using values of α, β, and s_1 that other experiments have shown to be reasonable. However, they generally cannot be fitted with Eq. (16) alone. At low standoff the experimental penetration rises so rapidly with standoff that some ductile drawing needs to be postulated to account for the facts.

EXERIMENTAL TESTS OF THE VELOCITY EQUATION

Equation (9) indicates that the velocity of penetration U should depend upon the density of the target material ρ but should be independent of all other properties of the target. Since Eq. (9) was derived for steady-state conditions like those shown in Fig. 12c, it cannot be

strictly true for variable jets. However, it should hold approximately for average values of V and U if the velocity measurements are made over a distance so short that the jet properties vary only slightly during the process. To compare results with different targets it will be necessary to have all of the targets at the same distance from the standard charge so that the average density of the penetrating jet is, as nearly as possible, the same in each target.

A number of different target materials, in plates of 2-in. thickness, have been tested at 6-in. standoff from standard charges with conical steel liners (base diameter 1.63 in., apex angle 45 degrees, wall thickness 0.036 in.). A high speed rotating drum camera was used to record the speed of the jet just before and just after it perforated the target plates (V_b and V_a, respectively) and the time required for that perforation. The average velocity $\bar{U}$ is obtained from the perforation time, and the average jet velocity is given by $(V_b+V_a)/2$. Now Eq. (9) can be written

$$\frac{V-U}{U}=(\rho/\rho_j\lambda)^{\frac{1}{2}}=(\rho)^{\frac{1}{2}}/J,$$

or

$$\frac{V}{U}=(\rho)^{\frac{1}{2}}/J+1, \qquad (17)$$

where $J=(\lambda\rho_j)^{\frac{1}{2}}$ depends only on the jet density for a given liner material.

From Eq. (17) a straight line should be expected if the ratio of average velocities $(V_b+V_a)/2\bar{U}$ is plotted as a function of $(\rho)^{\frac{1}{2}}$, where ρ is the target density. Figure 17 shows such a plot. The individual shots scatter rather badly, but the averages (indicated by circles) for each target material lie fairly close to a straight line which, as should be expected from the equation, passes through the intercept (0,1).

The scatter of the individual points is due to variations in jet density caused by variations in the spreads or the rates of elongation in the jets. The variations in spread are known to be the most important. From the slope of the line in Fig. 17 the average value of $\lambda\rho_j$ (reciprocal of the square of the slope) of these jets, when they are between 6 and 8 in. from the cone base, can be obtained. The average maximum and minimum values of $\lambda\rho_j$ from Fig. 17 are, respectively, 3.0, 9.0, and 1.4 g/cc. If λ is near 2 in each case, the jet densities are, respectively, 1.5, 4.5, and 0.7 g/cc, which should be compared with 7.8 g/cc, the density of steel. The value 4.5 g/cc for the best jet is so near the density of steel that this jet probably acted somewhat like a continuous jet with a λ less than 2. In which case the actual density was more than 4.5 g/cc.

In some early velocity measurements on jets from nearly identical shaped charges before and after they perforated a given target plate, a curious effect was noticed. When the target plate was close to the charge, velocities of the jets after perforation were smaller than when the target plate was farther away. With charges similar to that shown in Fig. 2, but with an aluminum liner, the velocity of the jet after perforating a 2-in. mild-steel plate at 6-in. standoff was only 4600 m/sec., whereas when this plate was at 18-in. standoff the velocity after perforation was 6300 m/sec. At 30-in. standoff the velocity after perforation had dropped back to 6000 m/sec.

This rise and fall of jet velocities after perforating a given target plate may be surprising at first, though such behavior should be expected from the principles just discussed. Measurements on jet velocities are made upon the front of the jet. A target plate shortens the jet by removing the faster particles at the front.

The jet that emerges from the rear of the target is then headed by slower particles, and the observed velocity is slower. The amount of the reduction in the observed velocity after perforating a target plate depends upon the amount of material that is removed from the front of the jet by that target plate; the more jet material that is removed, the greater is the reduction in the observed velocity. At both large and small standoffs the jet penetrates inefficiently, so that a large part of its mass is removed by a target plate, whereas at optimum standoff it penetrates more efficiently and a smaller part of its mass is removed.

Since the velocity gradient is almost constant along the length of the jet, the fraction of the jet removed is given roughly by $\Delta V/(V_1-V_2)$, where ΔV is the observed reduction in velocity and V_1-V_2 is the difference between the velocities of the front and rear of the jet. The

fraction of the jet removed by a target plate at a given standoff should be approximately equal to b/P, the ratio of the thickness b of the target plate to the total penetration P that would be produced by this jet in a massive target of this same material at this same standoff. Roughly then $\Delta V=[b(V_1-V_2)/P]$, which indicates the reduction in velocity of the jet due to the target plate, is inversely proportional to the penetration P that would be produced in a massive target of this material at this standoff. The point at which V is smallest should then be near the optimum standoff for the charge. This has been observed with charges lined with aluminum cones. For other linings the situation is not so certain, possibly because the data obtained to date is inadequate.

There are a number of groups who are now attempting to develop peacetime applications for these charges. It is hoped that the above discussion may help groups who do not have access to classified reports to avoid unnecessary duplication of experiments that have already been performed.

BIBLIOGRAPHY

B. Bomborn, "Die neue deutsche Sprengkapsel von Schulze," Zeits. f. d. ges. Schiess- und Sprengstoffwesen **16**, 177 (1921).

John B. Huttle, "The shaped charge for cheaper mine blasting," Eng. and Mining J. No. 5, 147, 58 (1946).

H. Kast, *Spreng- und Zuendstoffe* (Friedr. Vieweg and Sohn Akt. ges., Braunschweig, 1921), p. 273.

H. Kast und Haid, "Untersuchungen ueber die Brauchbarkeit der Methoden zur praktischen Pruefung von Sprengkapseln," Zeits. f. d. ges. Schiess- und Sprengstoffwesen **19**, 146, 183 (1924).

Robert S. Lewis and George B. Clark, "Application of shaped explosive charges to mining operations: tests on steel and rock," Bull. University of Utah No. 5, 37 (1946).

D. Lodati, "Eine Erklaerung fuer das explosive Verhalten von Hohlkoerpern aus gepresstem Trinitrotoluol," Giornale di chim. ind. ed. appl. **14**, 130 (1932).

M. Lupus, "Sprengkapseln und Initiatoren," Zeits. f. d. ges. Schiess- und Sprengstoffwesen **20**, 83 (1925).

A. Marshall, "The detonation of hollow charges," J. Sec. Chem. Ind. **39**, 35 (1920).

Charles E. Munroe, "Modern explosives," Scribners Mag. **3**, 563 (1888).

Charles E. Munroe, "The application of explosives II," Pop. Sci. Monthly **56**, 444 (1900).

Charles E. Munroe, "Wave-like effects produced by the detonation of Guncotton," Am. J. Sci. (Silliman) **36**, Series 3, 48 (1888).

Egon Neumann, "Neuartige Hohlkoerper aus Brisanzstoffen," Zeits. f. d. ges. Schiess- und Sprengstoffwesen **9**, 183 (1914).

M. Neumann, Zeits. f. angew. Chemie **24**, 2238 (1911).

W. Payman and D. W. Woodhead, "Explosion waves and shock waves V, the shock wave and explosion products from detonating solid explosives," Proc. Roy. Soc. London No. 915, 163, 575 (1937).

W. Payman, D. W. Woodhead, and H. Titman, "Explosion waves and shock waves II, the shock waves and explosion products sent out by blasting detonators," Proc. Roy. Soc. London Series A, 148, 604 (1935).

A. Stettbacher, "Fortschrittliche Sprengtechnik IV, Zuender und Brisanzwirkung, insbesondere bei Minenladungen," Erweiterter Sonderdruck aus der Zeitschrift "Nitrozellulose," 29, Published by Pansegrau, Berlin-Wilmersdorf, 1936/37.

Alfred Stettbacher, "Verfahren und Vorschlaege zum Detonieren von Sprengladungen," Zeits. f. d. ges. Schiess- und Sprengstoffwesen, **10**, 16 (1915).

S. Stettbacher, *Schiess- und Sprengstoffe* (J. A. Barth, Leipzig, 1933), second edition, p. 51.

M. Sucharewsky, "Ueber die Erscheinungen beim Sprengen mit Hohlkoerpern und ueber die praktische Bedeutung der Anwendung des Hohlkoerperprinzips und solcher Ladungen in der Sprengtechnik," Woina i Technica **253**, 18 (1926).

M. Sucharewsky, "Untersuchungen der Frage ueber die Moeglishkeit der Steigerung der Brisanzwirkung von Sprengstoffen durch die Methode der Kumulationswelle," (Technica i Snabschenie krasnoi Armii) **170**, 13, and **177**, 13 (1925).

V. Torrey, "Bazooka's grandfather," Pop. Sci. Monthly **146**, 65 (1945).

V. Torrey, "Shaped charge, Munroe effect," Explosives Eng. **23**, 160 (1945).

Max von Foerster, *Versuche mit comprimirter Schiessbaumwolle* (Mittler und Sohn, Berlin, 1883).

Westfaelisch Anhaltische Springstoff A. G., "Verbesserung bei Sprengladungen und Sprengkoerpern," Patent 10/10/1912.

Westfaelisch Anhaltische Sprengstoff A. G., "Verfahren zur Hertstellung von Sprengkoerpern," Zeits. f. d. ges. Schiess- und Sprengstoffwesen **6**, 358 (1911).

Westfaelisch Anhaltische Sprengstoff A. G., "Verfahren zur Herstellung von Sprengkoerpern," Patent 7/22/1912.

R. W. Wood, "Optical and physical effects of high explosives," Proc. Roy. Soc. London **157**, 249 (1936).

Zeits. f. d. ges. Schiess- und Sprengstoffwesen **9**, 183 (1914).

Spectral Emissivity and Electron Emission Constants of Thoria Cathodes

T. E. Hanley
Vacuum Tube Research Section, Naval Research Laboratory, Washington 20, D. C.
(Received January 16, 1948)

A method is described for forming cathodes by means of a cataphoresis process wherein a thin layer of thoria is deposited over an underlying metal. A temperature scale determination yields for the relation between true temperature (°K) and brightness temperature (°C) at $\lambda=0.65$ micron: $T_t=1.172T_b+177.5$. Electron emission studies yield for the constants of the Richardson equations:

$A=2.63$ amp./cm²/deg.²; $\Phi=2.67$ volts for d.c. emission,
$A=5.62$ amp./cm²/deg.²; $\Phi=2.55$ volts for pulsed emission.

Information was also obtained regarding the resistivity of thoria at high temperatures.

I. INTRODUCTION

At the present time substantial progress in the field of high frequency vacuum tubes is limited by the demands upon the cathode. This limitation has resulted in a great deal of research and development in this field. Of the various possible approaches under exploration, cathodes fabricated of thorium oxide (thoria, ThO_2) appear to offer considerable hope for early dividends.

Early work on thoria cathodes indicated that they are superior to conventional barium-strontium oxide as regards electron emission particularly under d.c. conditions. However, progress in the thoria cathode development has been handicapped by the lack of fundamental studies and, in addition, by the fact that the early cathodes would not stand up under mechanical and thermal shock.

As a consequence, the initial approach in this laboratory has been directed towards eliminating or reducing the magnitude of these handicaps. A determination of the temperature scale and of the electron emission constants yielded the fundamental data desired. To overcome the mechanical limitations a program was initiated to develop cathodes by the method of cataphoresis.

In this process finely divided particles of an insulator are deposited onto a metal in a manner resembling ordinary plating. This method has been used successfully in the case of the conventional oxide cathodes and for applying insulation coatings to vacuum tube heaters.[1] Cataphoresis was tried in the case of thoria because it appeared to offer the possibility of forming cathodes of shapes and design not possible by the then existing techniques.

Work was then directed towards obtaining data regarding the spectral emissivity and electron emission constants of thoria cathodes formed by cataphoresis.

II. FABRICATION OF THORIA CATHODES BY CATAPHORESIS

The thoria used in the cataphoretic process was procured from the National Bureau of Standards. It is a 200-mesh powder obtained by the decomposition of thorium nitrate. Spectroscopic analysis of the material at the Bureau of Standards results in the following composition determination:

Al <0.1 percent; Ca <1 percent; Cu <0.1 percent; Mg <0.01 percent; Si <0.1 percent.

The analysis does not indicate whether the impurities are present in the metallic form or as oxides or other compounds.

To make the coating bath, the powdered thoria was shaken up in ethyl alcohol to which was added a small amount of thorium nitrate. A bath that yields good coatings is obtained by adding 5 g of 200-mesh thoria and 0.075 g of thorium nitrate to 100 ml of 95 percent alcohol.

To secure good coatings it was found that the required current density depended very markedly upon the diameter of the wire or the sleeve being coated, but not upon its nature. Coatings were formed onto molybdenum, tung-

[1] E. C. Bidgood and George H. Kent, "Cataphoresis and alundum coatings," Electrochem. Soc. **87**, 321 (1945).

sten, and tantalum with no observable difference in the mechanical adherence. As will be seen later, the spectral emissivity and electron emission also appeared to be independent of the nature of the underlying core material. In most cases of electron emission studies, the coatings were formed on 0.005″ tungsten wire (Callite "200H). Sleeves were made by rolling 0.003″ molybdenum to the desired size. The wires were cleaned in ethyl alcohol or fired in H_2 before coating; whereas the sleeves were always fired in H_2. Early crude electron emission tests on coated wires showed no differences depending upon the method of cleaning the wire.

In the coating process, the wire or sleeve to be coated was made the negative electrode. In all cases the criteria of a satisfactory coating were that it be well adherent and that it appear uniform under visual, microscopic, and pyrometric (when heated) observation. It was observed that coatings which were satisfactory on the basis of the above-mentioned criteria had similar microscopic appearances independent of the diameter of the wire or sleeve being coated. This fact is utilized in later discussion. The marked dependence of the current density upon the geometry of the object to be coated (for securing satisfactory coatings) is clearly brought about by the fact that a wire 0.005″ in diameter requires a current density of 75 milliamperes per cm^2 for 2 seconds, whereas one 0.155″ in diameter requires only 600 microamperes per cm^2, but for 15 minutes. The determination of the proper current density for various surface geometries to be coated presented no great difficulties.

FIG. 1. Coating bath used in coating metal cylinders.

In general, coatings between 0.0010″ and 0.0015″ in thickness appeared to be most satisfactory from all standpoints. Figure 1 illustrates the type of coating bath used on the larger objects where the coating rate was slow.

III. PARTICLE SIZE

It might appear, in view of the fact that the thoria used was so-called "200 mesh," that a large fraction of the particles in the coating may approach 50 microns in diameter. However, particle size measurements indicated that the coatings were made up almost entirely of particles of diameters between 0.25 and 1 micron with an occasional diameter as great as 5 microns.

These particle size measurements were made with an oil immersion microscope under a magnification of 1500 and with an electron microscope using magnification of 22,000 (Fig. 2). It may be concluded from these measurements that cataphoresis is a selective process which favors the smaller particles in the bath, whereas the larger particles settle out before they can take part in the coating process. This is actually observed.

An x-ray diffraction study set a lower limit of 0.05 micron to the crystal size and, in addition, yielded the interesting result that the coating is essentially pure thoria. A spectroscopic determination of the coated material was carried through immediately after coating and before any heating had taken place. This indicated that there was a trace of Ni present (<0.01 percent) presumably as a result of the use of a nickel anode in the coating bath. Also there were faint traces (<0.001 percent) of Al, Ca, Cu, Mg, and Si.

IV. TEMPERATURE SCALE

Molybdenum sheet 0.003″ thick was rolled into a cylinder 0.152″ in diameter, fired in H_2, and then coated by the method described above.

A number of 0.045″ holes drilled in the sleeve permitted true temperature determinations to be made by sighting through the holes with an optical pyrometer. Brightness temperatures were determined by sighting on the external coating. The effective wave-length of the pyrometer employed was 0.65 micron.

The heating process was carried out by passing current through the sleeve which was mounted in an inverted bell jar through which a flow of hydrogen was maintained at the rate of 3–15 cubic feet per hour. The measured results were independent of the rate of hydrogen flow. Further evidence that the presence of the hydrogen does not affect the measured values is given by tests carried out on similar sleeves in evacuated magnetrons. The diode emission characteristics for these sleeves, when used for magnetron cathodes, checked those obtained with test diodes wherein thoria-coated wire was employed as the cathode. In both cases the temperature scale employed was that obtained from the sleeve in the hydrogen atmosphere.

The question of temperature drop through the sleeve merits attention. Unpublished measurements of temperature drop through thick thoria sleeves made at the Bartol Research Foundation indicate that the temperature drop through the coatings studied cannot, at most, exceed 2°C. This small drop has been neglected in all cases.

The sleeve was made 10 cm long to insure that end cooling effects were negligible.

It was observed that the temperature scale depended to some extent upon the coating procedure. However, it appeared that coatings similarly prepared, and which were microscopically similar, yielded results which agreed within the limits of experimental error. It was felt safe to "extrapolate" these observations to include surfaces of all diameters which had coatings microscopically similar. As a consequence, the temperature scale, as determined for the 0.155″ sleeve, was used in determining the electron emission constants from data obtained with very much smaller coated wires.

The actual data relating true and brightness temperature obtained from a number of sleeves are plotted in Fig. 3 together with an average curve. From this curve one can obtain the empirical relation:

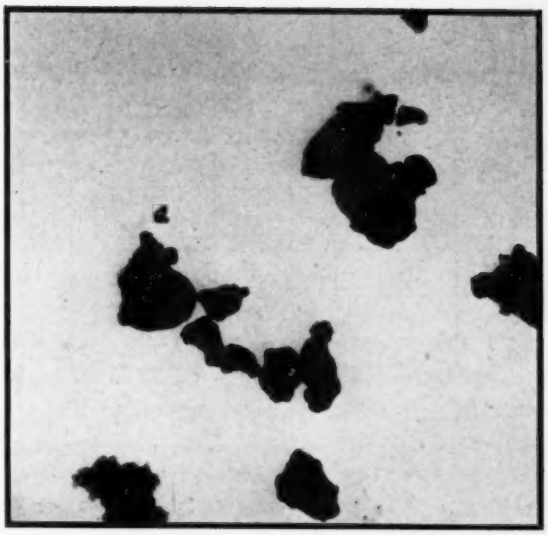

FIG. 2. Electron microscope photo giving thoria particle size.

$$T_t = 1.172T_b + 177.5, \qquad (1)$$

where T_t is the true temperature in degrees K, T_b is the brightness temperature in degrees C.

From the well-known relationship between

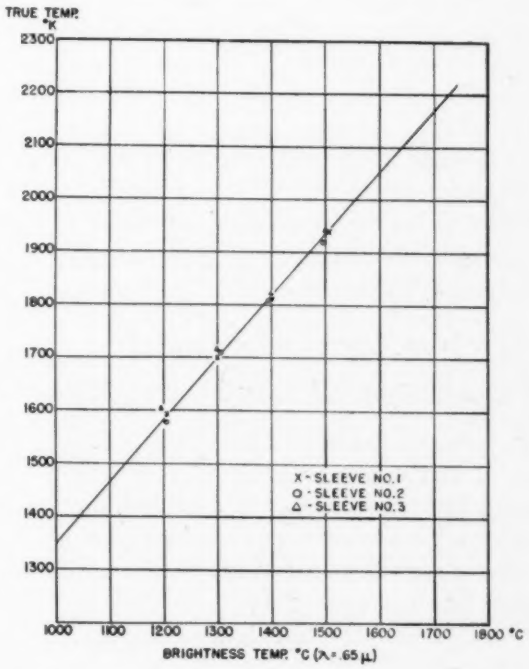

FIG. 3. True temperature in °K *vs.* observed brightness temperature in °C for thoria coatings on molybdenum sleeves.

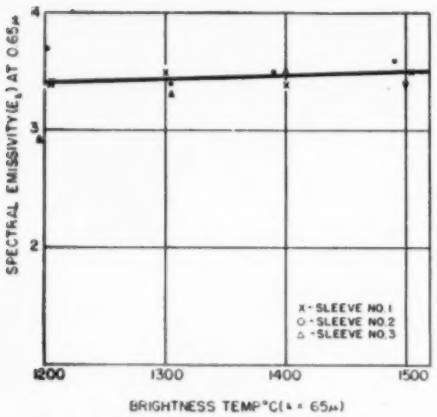

FIG. 4. Plot of spectral emissivity *vs.* brightness temperature for thoria coatings on molybdenum cylinders.

true and brightness temperatures:

$$(1/T_t)-(1/T_0)=(\log_{10}E_\lambda)/9588, \qquad (2)$$

where T_0 is the brightness temperature in degrees K and E_λ the spectral emissivity at $\lambda=0.65$ micron, one can determine the spectral emissivity of the thoria cathodes prepared in the manner described. The data are plotted in Fig. 4 together with an averaged curve. It will be seen that the spectral emissivity centers about 0.35. Previously reported values vary between 0.08 and 0.57.[2] The accuracy of some of these determinations is subject to doubt. In any case, the surface structure of the thoria specimens for some of the other work is quite different from that studied here and would be expected to yield different results. It is of interest to point out that an emissivity value of 0.35 was employed in a recent study of the electron emission from thoria sprayed onto metal.[3]

V. ELECTRON EMISSION

A. Description of Emission Study Tubes

In order to obtain the data for the determination of the emission constants, measurements were taken on six tubes of the form illustrated in Fig. 5. This is a conventional guard ring type diode, in which the current measured to the middle anode is used for the determination of the electron emission constant. Actually, these anodes were 0.5″ long with an inside diameter of 0.25″ and a separation of 0.060″.

The cathodes consisted of 0.005″ tungsten wire coated to a diameter of 0.0075″ to 0.0080″ with thoria, and then mounted in the tube without further treatment. In order to permit good outgassing during exhaust, the anodes were constructed of tantalum. The tubes were baked at 425°C for three hours and then the metal parts were outgassed by electron bombardment. During the heating up of the cathode an activation appears to take place which results in stable and reproducible emission being achieved when a temperature of 1550°C brightness is reached.

B. Emission Studies

The cathode is set initially at about 1500°C brightness and the current (to the middle anode) is measured as a function of the anode voltage. This process is repeated at a series of lower cathode temperatures.

The current and voltage data are now plotted in the form illustrated in Fig. 6. By plotting $\log_{10}I$ against V, one obtains the so-called Schottky plot[4] given in Fig. 7. I is the anode

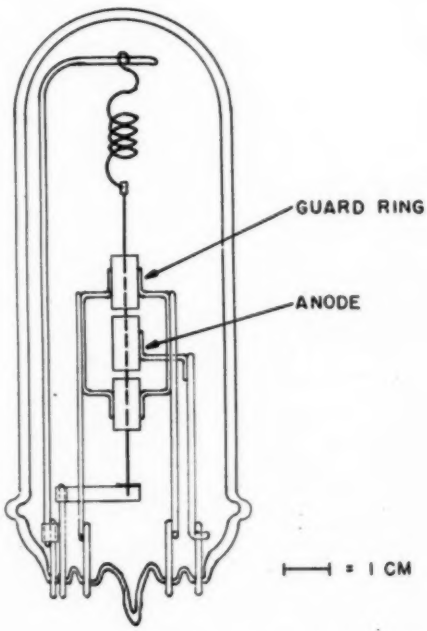

FIG. 5. A sketch of one of the experimental diodes.

[2] M. O. Weinreich, Rev. Gen. de L'Elec. **54**, 234 (1945).
[3] D. A. Wright, "Thermionic properties of thoria," Nature **160**, 129 (1947).
[4] K. T. Compton and I. Langmuir, Rev. Mod. Phys. **2**, 147 (1930).

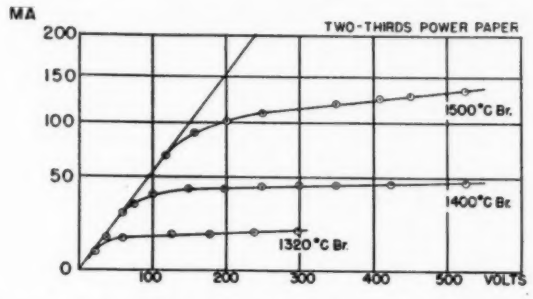

FIG. 6. A two-thirds power plot of the d.c. emission from a thoria coating on 0.005" tungsten wire.

current corresponding to the anode potential V. It can be shown that the value of the anode current to be used in determining the emission constants is that corresponding to zero anode voltage. This current is obtained from the Schottky plot by extrapolating the linear portion of the characteristic curve down to zero voltage. (Broken lines in Fig. 7.)

From the values of the plate current at zero field and the measured cathode area, one determines the value of the current per unit cathode area. This current density is denoted by I_0. From I_0 and the true temperature of the cathode, as obtained from the observed brightness temperature and the temperature scale of Fig. 3, one can plot

$$\log_{10}(I_0/T_t^2) \text{ vs. } (1/T_t),$$

where T_t is the true cathode temperature in degrees K.

This is a so-called Richardson plot, whose slope determines the work function and whose intercept with the zero axis for $1/T_t$ (corresponding to $T=\infty$) determines the constant A of Richardson's equation:

$$I_0 = AT_t^2\epsilon^{(-e\Phi/kT_t)} \qquad (4)$$

where e is electron charge and k the Boltzmann constant.

The data for the Richardson plot are given in Fig. 8. An averaged curve through these data yields the following values for the d.c. emission from thoria cathodes prepared in the manner described:

$$\Phi = 2.67 \text{ volts},$$
$$A = 2.63 \text{ amp./cm}^2\text{/deg.}^2.$$

In Fig. 8 are also given the results of the pulsed emission measurements which were made with a pulse length of 1.8 microsecond and a repetition rate of 540 cycles per second using a Raytheon Laboratory type modulator. A Schottky correction was also used on the pulsed data. An averaged curve for the pulsed data yields:

$$\Phi = 2.55 \text{ volts},$$
$$A = 5.62 \text{ amp./cm}^2\text{/deg.}^2.$$

In each case these results indicate the average of the measurements taken, and it can be seen that there is a spread of the points amounting to about 30 percent on either side of the Richardson line. This spread is no doubt in considerable part due to errors of measurement, particularly those involved in the determination of true temperature. There is some variation, however, which is very likely genuine in the sense that different cathodes may have different values of emission constants (both electronic and spectral) due to unavoidable variations in their preparation. These spreads in the data are not considered serious for complex cathodes of this type.

These results may be compared with the recently reported values of Wright[3] for the case of thoria sprayed onto tantalum. These are:

$$\Phi = 2.5(4) \text{ volts},$$
$$A = 2.5 \text{ amp./cm}^2\text{/deg.}^2 \text{ for d.c. emission},$$

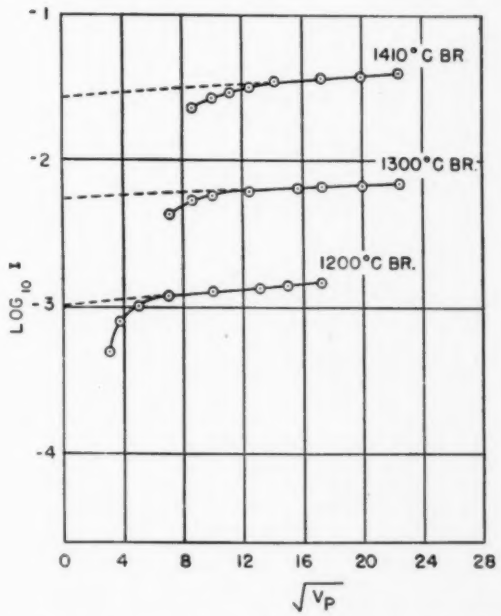

FIG. 7. An example of a Schottky plot of the d.c. emission from one of the diodes.

and

$\Phi = 2.6(2)$ volts,

$A = 7.5$ amp./cm^2/deg.^{2} for pulsed emission.

A question exists as to whether the form of Richardson's equation given by Eq. (3) is the correct one to employ for the case of a complex cathode of the type studied here. However, until further information is available on this subject, and since other workers are using the form of Eq. (3) thus making possible a direct comparison of Φ and A values as determined by different observers, it appears best to abide by this usage.

C. Discussion of the Emission Studies

An examination of the data for both the pulsed and the d.c. emission cases, as plotted in Fig. 8, shows that there is a very real difference between the two cases. The magnitude of difference between the two cases is brought home when one notes that over the temperature region where it is expected that the thoria cathodes will be of greatest value, the pulsed emission (corrected for zero field condition) is more than five times the corresponding d.c. value. In this respect, thoria cathodes of the type studied are similar in their behavior to the conventional barium-strontium oxide cathodes. However, a very real difference does exist. In these pulsed emission studies, the pulse length was increased to as much as 100 microseconds with the duty cycle going up at the same time to 0.1, without any observable decrease in emission. The lower emission for the d.c. case must occur at duty cycles in excess of 0.1, or at pulse lengths greater than 100 microseconds, or both.

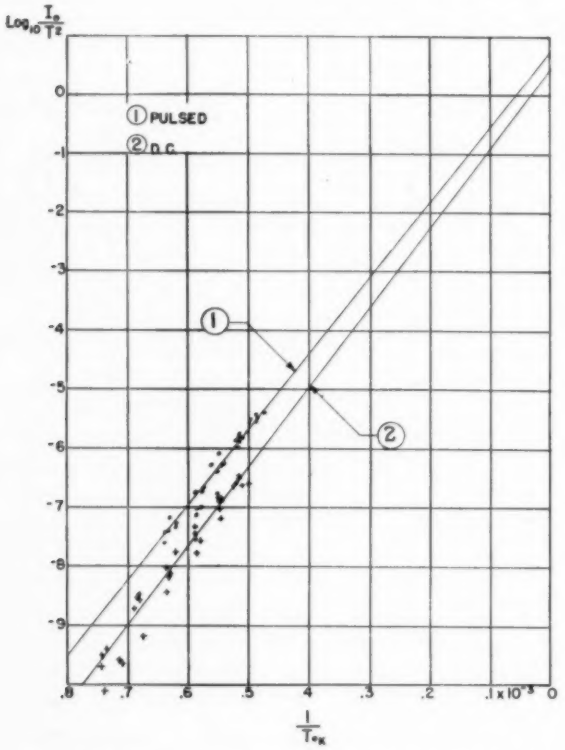

FIG. 8. A Richardson plot of both the d.c. and pulsed emission data obtained from six diodes.

VI. HIGH TEMPERATURE CONDUCTIVITY OF THORIA

When the anode current is plotted against the voltage on $\frac{2}{3}$ power paper, the region of space-charge limited emission should lie along the so-called Langmuir line. This follows from the Langmuir equation which can be put in the form:

$$V = KI^{\frac{1}{2}}, \qquad (5)$$

where K is a constant which depends upon the geometry of the electrodes of the diode. This relationship holds in the region of space-charge limited emission only.

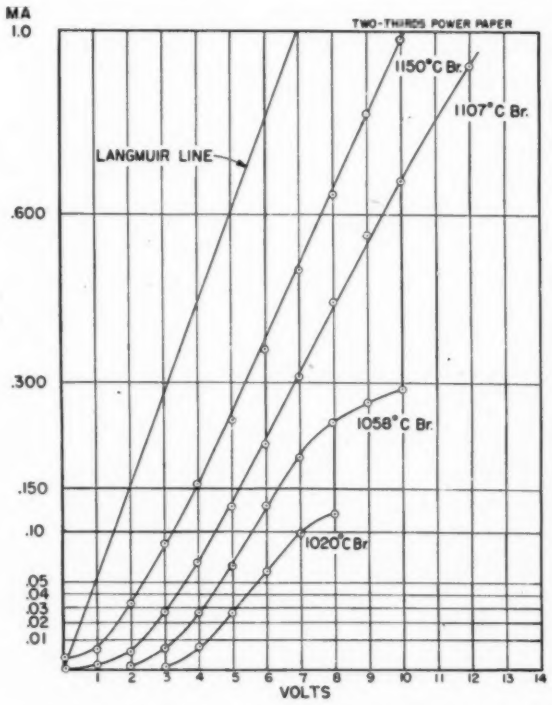

FIG. 9. Curves illustrating the effect of coating resistance on a two-thirds power plot at lower temperatures.

In Fig. 9, wherein are plotted the data for several operating temperatures, it is seen that at low temperatures the experimental curves do not fall along the Langmuir line. This is ascribed to the finite resistivity of the thoria coatings. As the temperature is raised, the resistivity decreases, thus resulting in the observed data approaching the Langmuir line.

The difference between the experimental curve and the Langmuir line is a measure of the voltage drop through the thoria coating. From this voltage drop and the anode current, one can determine the total resistance R between the underlying metal and the outside surface of the thoria, a thickness of 0.0012". This resistance may be due in part to the properties of an interface barrier which may exist between the tungsten and the thoria and in part to the thoria itself. A separation of the contributions to the measured resistance would require a more elaborate experiment. If one assumes, on the basis of a statement by Wright,[3] that such a barrier does not exist, the measured values can be used to determine thoria resistivity. In that case,

$$\rho = (R 2\pi r_{Av} l)/t, \qquad (6)$$

where ρ is the thoria resistivity (if the interface resistance is neglected), r_{Av} is the average radius of the thoria coating, l is the length of the coated section being measured, and t is the coating thickness.

$\mathrm{Log}_{10} 1/\rho$ as a function of temperature is plotted in Fig. 10. Here the R used for each temperature is an averaged value obtained from the slope of the curve (not shown) that results when ΔV is plotted against the anode current.

The data involved in this resistivity determination include a small difference between two quantities, and are, as a consequence, subject to considerable error. The results as plotted on

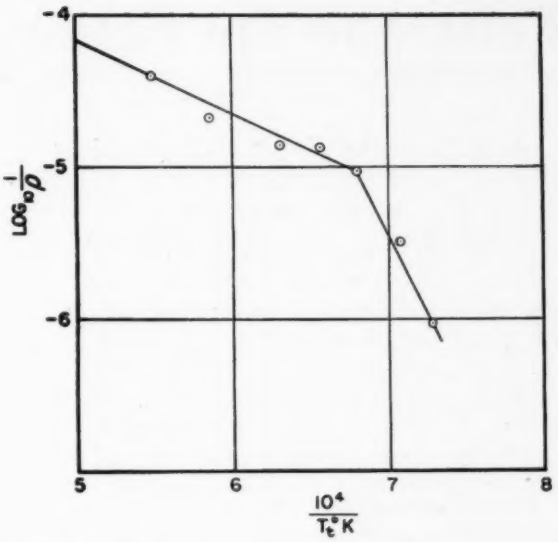

FIG. 10. Plot of conductivity *vs.* reciprocal of temperature for thoria coated on tungsten.

Fig. 10 should thus be considered as being only approximate.

VII. SUMMARY

A method is described for forming cathodes by means of a cataphoresis process wherein a thin layer of thoria is deposited over an underlying metal.

The spectral emissivity and electron emission of cathodes of the type described have been determined over a range of temperatures. The results in the case of electron emission are different for pulsed and d.c. emission and thus lead to different values for the electron emission constants.

In addition, data are presented which set an upper limit to the resistivity of thoria as a function of temperature.

VIII. ACKNOWLEDGMENT

The author wishes to express his appreciation to L. Malter for advice rendered during the course of this work.

Letters to the Editor

Analogy between Isopachic Stress Lines and Equipotential Lines

ROBERT EMMETT MUELLER
Senior House, Massachusetts Institute of Technology, Boston, Massachusetts
December 19, 1947

OF the many analogous methods used in the plotting of field patterns one that has not been previously mentioned (to my knowledge) is the photo-elastic analogy. Prior to the work done by M. M. Frocht[1] the lines available were the difference of the principal stresses, which are not useful in setting up an electrical field analog. In his article Mr. Frocht showed a way of obtaining the sum of the principal stresses using an optical set-up, which are directly analogous to equipotential field lines. This would lead to a method where a photograph could readily be obtained of the equipotential lines given the geometry and boundary conditions of the field problem.

[1] M. M. Frocht, "Isopachic stress patterns," J. App. Phys. **10**, 248 (1939).

A Note on the Phase Difference between Two Waves Reflected from the Ionosphere

J. M. KELSO
The Pennsylvania State College, State College, Pennsylvania
(Received March 9, 1948)

THIS work was undertaken with the object of verifying two relations concerning the phase difference between two waves reflected from the ionosphere, which were given without proof by Appleton and Beynon:[1]

(1) At a frequency f_1 the change in phase difference between two rays (in particular the two magneto-ionic components), when the frequency is changed by the small amount δf_1, is given by the product of the reciprocal of f_1 times the area ABEF between the two P'–f curves in Fig. 1.
(2) In the case of oblique incidence at a frequency f_1 the phase difference between the low ray and the high (Pedersen) ray is given by the product of the reciprocal of f_1 times the area ABC between the P'–f curves in Fig. 2. Here the curve AC belongs to the high ray and the curve BC belongs to the low ray.

There are two path lengths to be considered, the optical path (phase path), $P=\int \mu ds$, and the group path, $P'=c\int(ds/v)$, where μ is the index of refraction, v is the group velocity, c is the velocity of light in air, and where the integrals are taken along the actual path. It is known that P and P' are related by the differential equation[2]

$$f(dP/df)+P=P', \tag{1}$$

where f is the frequency, which when integrated becomes

$$P=(1/f_1)\int_0^{f_1}P'df. \tag{2}$$

Now, suppose there are two rays, Ray 1 and Ray 2. Then

$$\Delta P=P_2-P_1=(1/f_1)\int_0^{f_1}(P_2'-P_1')df$$

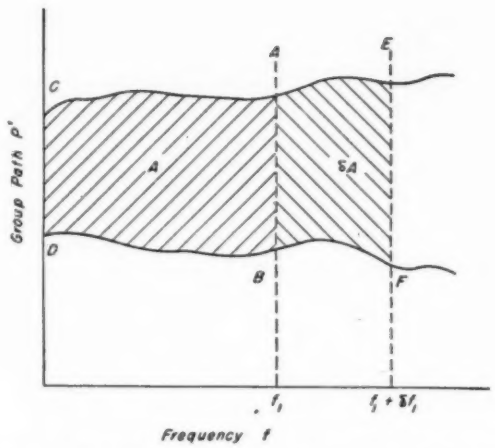

FIG. 1. Group path as a function of frequency for two waves reflected from the ionosphere. The shaded regions are the areas discussed in the text.

or

$$\Delta P=(1/f_1)\int_0^{f_1}\Delta P'df. \tag{3}$$

It is obvious that the above integral is just the shaded area $ABCD$ in Fig. 1. Hence, letting the area $ABCD=A$,

$$\Delta P=A/f_1. \tag{4}$$

If the frequency is now increased by a small amount, δf_1, the optical path difference becomes

$$\Delta P+\delta(\Delta P)=(A+\delta A)/(f_1+\delta f_1),$$

where $\delta(\Delta P)$ and δA are the increases in the phase path difference and in the area, respectively. But δf_1 is small compared with f_1 and hence

$$\delta(\Delta P)=\delta A/f_1=ABEF/f_1, \tag{5}$$

which is just the first relation given by Appleton and Beynon.

We now consider the change in phase difference between the low ray and the high ray when the frequency is changed from f_1 to f_m, where f_m is the maximum usable frequency and with $f_1>f_c$, where f_c is the critical frequency at vertical incidence. From Fig. 2 it is obvious that at f_m, $\Delta P'=0$, and hence $\Delta P=0$. From Eq. (3)

$$(\Delta P)_{f_1}-(\Delta P)_{f_m}=(1/f_1)\int_0^{f_1}\Delta P'df-(1/f_m)\int_0^{f_m}\Delta P'df,$$

where $(\Delta P)_{f_1}$ and $(\Delta P)_{f_m}$ mean the phase differences at the frequencies f_1 and f_m, respectively. We may rewrite the first integral and obtain

$$(\Delta P)_{f_1}-(\Delta P)_{f_m}=(1/f_1)\int_0^{f_m}\Delta P'df-(1/f_1)\int_{f_1}^{f_m}\Delta P'df$$
$$-(1/f_m)\int_0^{f_m}\Delta P'df=((1/f_1)-(1/f_m))\int_0^{f_m}\Delta P'df$$
$$-(1/f_1)\int_{f_1}^{f_m}\Delta P'df.$$

Now, as stated above,

$$(\Delta P)_{f_m}=(1/f_m)\int_0^{f_m}\Delta P'df=0.$$

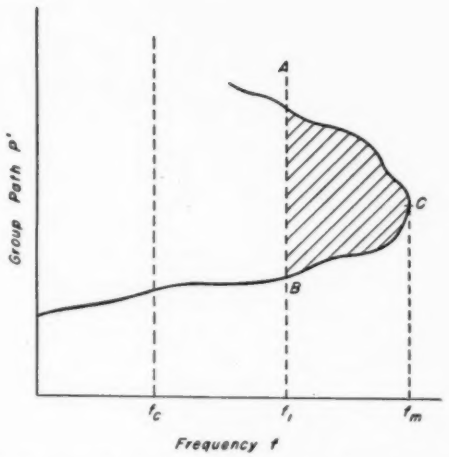

FIG. 2. Group path as a function of frequency for the two waves reflected from the ionosphere at oblique incidence.

Hence, since $f_m \neq 0$, the integral must vanish. Thus,

$$(\Delta P)_{f_1} = -(1/f_1)\int_{f_1}^{f_m} \Delta P' df, \tag{6}$$

where it can be seen that the integral is the area ABC in Fig. 2. Thus

$$(\Delta P)_{f_1} = ABC/f_1, \tag{7}$$

which is the second of the relations desired.

Although Appleton and Beynon apparently restrict their discussion to the case where there is a parabolic distribution of ions and where the earth may be assumed to be flat, the above proofs show that the results are much more general. The principal requirement is that the given curves be true P'–f curves (and hence that Eqs. (1) and (2) can be satisfied). Thus the results obtained in this way from sufficiently good experimental curves should be quite valid. In addition to this restriction it was merely assumed above that the P'–f curves were reasonably well-behaved functions and, in the second case, that the P'–f curve was concave toward the P' axis.

This work was done in the Department of Electrical Engineering of The Pennsylvania State College for the Watson Laboratories, Air Materiel Command, under Contract No. W28-099-ac-143.

The author wishes to thank Dr. A. H. Waynick of The Pennsylvania State College, whose suggestions and criticisms were of great help in this work.

[1] E. Appleton and W. J. G. Beynon, Proc. Phys. Soc. **59**, 58 (1947).
[2] S. K. Mitra, Proc. Nat. Inst. Sci. India **1**, No. 3, 131 (1935).

New Booklets

Eberbach and Son Company, Ann Arbor, Michigan, announces a new bulletin, No. 90–11, which shows the company's line of redesigned metallographic polishing machines for laboratories. 4 pages, free on request.

The Educational Service Division of General Electric, Schenectady 5, New York, has issued a brochure entitled *Electrical Developments of 1947*, an account of the company's latest progress in science, engineering, and manufacturing. 48 pages.

The New York Journal of Commerce, 63 Park Row, New York, has brought out its 1948 edition of *New Products*, an 80-page booklet to help the business community keep in step with the scores of innovations now being marketed. More than 750 different companies are listed, along with a detailed description of the new products they are about to introduce. 50 cents each.

RCA Victor Division, Harrison, New Jersey, announces its booklet 1275-D, entitled *RCA Receiving Tubes for Television, FM, and Standard Broadcast*. 24 pages. 10 cents each. Order from the RCA Tube Department.

Central Scientific Company, 1700 Irving Park Road, Chicago 13, Illinois, publishes *Cenco News Chats* each quarter. The Spring 1948 issue has 16 pages and features an article on Luther Burbank.

Rex Rheostat Company, 3 Foxhurst Road, P. O. Box 232, Baldwin, Long Island, New York, has issued its Catalog No. 4, which describes the company's new vitreous, enameled, round power rheostat. 4 pages, free on request.

Burrell Technical Supply Company, 1942 Fifth Avenue, Pittsburgh 19, Pennsylvania, announces its bulletin No. 208 on metallographic polishing supplies, featuring the new metallographic polishing compound, "C-RO." 4 pages, free on request.

The Allen B. Du Mont Laboratories, Inc., Clifton, New Jersey, publish bimonthly a leaflet called *The Oscillographer*, containing descriptions and photographs of the company's products. 4 pages, free on request.

The National Bureau of Standards, Washington 25, D. C., announces the publication of the following booklets:

No. RP1846, *Factors Affecting Operation of Apparatus for Counting Alpha Particles in an Ion Counting Chamber*, F. J. Davis, 5 pages, 10 cents.

Applied Mathematics Series 1, *Tables of the Bessel Functions* $Y_0(x)$, $Y_1(x)$, $K_0(x)$, $K_1(x) \leqq x \leqq 1$, 71 pages, 35 cents.

Either booklet may be ordered from the Superintendent of Documents, Government Printing Office, Washington 25, D. C.

Clapp and Poliak, 350 Fifth Avenue, New York 1, New York, management of the National Materials Handling Exposition of last January, announce the publication of

the proceedings at technical sessions of the Conference on Materials Handling, held concurrently with the Exposition. The book, entitled *Some Basic Techniques in Materials Handling*, is believed to be the first report of its nature ever published and one of the few texts on materials handling problems. Nineteen papers are included. The book contains 84 pages, 15 pictures, 11 diagrams, and 4 charts and tables. It may be obtained for $1 from Clapp and Poliak.

The Esterline-Angus Company, Inc., Box 596, Indianapolis 6, Indiana, has published its bulletin No. 247, *The Graphic*, featuring an article on "Operation recorders—their selection and use." The company specializes in the manufacture of graphic instruments. 16 pages.

Here and There

New Appointments

Haldon A. Leedy was named Acting Director of Armour Research Foundation of Illinois Institute of Technology, effective March 15. Dr. Leedy has been associated with the Foundation since 1938.

Harry D. Huskey, authority on large-scale automatic digital computing machinery, has been appointed Chief of the Machine Development Laboratory of the National Bureau of Standards.

John N. Adkins has been appointed head of the Geophysics Branch, Physical Sciences Division, Office of Naval Research. He has been granted a year's leave of absence from Massachusetts Institute of Technology.

International Rheological Congress

An International Rheological Congress will be held at The Hague in The Netherlands from September 21 to 24, 1948. It will be devoted to theoretical problems, fundamental experimental methods, rheological properties of various systems, rheological problems in biology, and industrial applications. Plasticity of crystallized materials, soil mechanics, and geophysical problems will be excluded, as these are being covered in other international congresses during 1948. For further information address the Organizing Committee at Julianalaan 134, Postbox 66, Delft, Holland.

Bulletin of Mathematical Biophysics

The following is the table of contents of the June 1948 issue of the *Bulletin of Mathematical Biophysics:*

"On herbicidal actions"—I. Opatowski and Alice M. Christiansen.

"On matrices of neural nets"—Telson Wei.

"A mathematical study of organism growth as an approach to the cancer problem"—Russell H. Kesselman.

"Can elastic stresses in gels cause the elongation and division of a cell?"—N. Rashevsky.

"On the effects of a constant sub-threshold conditioning stimulus upon the response to a constant current test stimulus"—H. D. Landahl and J. B. Kahn, Jr.

"A mechanism for optic nerve conduction and form perception: II"—James T. Culbertson, The University of Chicago Press, Chicago, Illinois, Volume 10, Number 2.

Examination of High Grade Physicist Positions

An examination has been announced by the Civil Service Commission for filling high grade physicist positions in Washington, D. C., and vicinity. The salaries range from $7102 to $9975 a year. A written test is not required for this examination; candidates will be rated on their experience and training relevant to the duties of the position. Applications will be accepted until further notice; however, persons who wish to be considered for positions to be filled immediately should apply at once. Information and application forms may be obtained from most first- and second-class post offices or from the U. S. Civil Service Commission, Washington 25, D. C.

Summer Course on Radioisotopes

The Oak Ridge Institute of Nuclear Studies, P. O. Box 117, Oak Ridge, Tennessee, will sponsor three one-month courses at Oak Ridge this summer in the techniques of using radioisotopes. The courses will be held from June 28 to July 23, August 2 to August 27, and August 30 to September 24. Application forms and additional information may be obtained from Dr. Ralph T. Overman, Acting Head of the Institute's Department of Special Training.

Participants in the second of the three courses will be selected by the Atomic Energy Commission. Personnel of the other courses will be chosen from qualified applicants, with preference given to persons connected with organizations which are now engaging in research utilizing radioisotopes, or planning such research. Thirty-two participants will be selected for each course.

A fee of $25 will be charged for the month's study. Participants will be expected to pay their own travel and living expenses. Dormitory or hotel accommodations will be provided in Oak Ridge at the usual rates.